



**FEDERAL UNIVERSITY OF CEARÁ**  
**TECHNOLOGY CENTER**  
**DEPARTMENT OF TELEINFORMATICS ENGINEERING**  
**GRADUATE PROGRAM IN TELEINFORMATICS ENGINEERING**  
**MASTER DEGREE IN TELEINFORMATICS ENGINEERING**

**DANIEL SANTOS DA SILVA**

**BREAST ULTRASOUND IMAGE ENHANCEMENT TECHNIQUES FOR CANCER**  
**DETECTION AND CLASSIFICATION**

**FORTALEZA**

**2023**

DANIEL SANTOS DA SILVA

BREAST ULTRASOUND IMAGE ENHANCEMENT TECHNIQUES FOR CANCER  
DETECTION AND CLASSIFICATION

Dissertation submitted to the Graduate Program in Teleinformatics Engineering of the Technology Center of the Federal University of Ceará, as a partial requirement for obtaining the title of Master in Teleinformatics Engineering. Concentration Area: Signals and Systems

Advisor: Prof. Dr. Victor Hugo Costa de Albuquerque

FORTALEZA

2023

Dados Internacionais de Catalogação na Publicação  
Universidade Federal do Ceará  
Sistema de Bibliotecas  
Gerada automaticamente pelo módulo Catalog, mediante os dados fornecidos pelo(a) autor(a)

---

S579b Silva, Daniel Santos da.  
Breast ultrasound image enhancement techniques for cancer detection and classification / Daniel Santos da Silva. – 2023.  
83 f. : il. color.

Dissertação (mestrado) – Universidade Federal do Ceará, Centro de Tecnologia, Programa de Pós-Graduação em Engenharia de Teleinformática, Fortaleza, 2023.  
Orientação: Prof. Dr. Victor Hugo Costa de Albuquerque.

1. Breast Cancer. 2. Image Enhancement . 3. Biomedical Engineering. I. Título.

CDD 621.38

---

DANIEL SANTOS DA SILVA

BREAST ULTRASOUND IMAGE ENHANCEMENT TECHNIQUES FOR CANCER  
DETECTION AND CLASSIFICATION

Dissertation submitted to the Graduate Program in Teleinformatics Engineering of the Technology Center of the Federal University of Ceará, as a partial requirement for obtaining the title of Master in Teleinformatics Engineering. Concentration Area: Signals and Systems

Approved on:

EXAMINATION BOARD

---

Prof. Dr. Victor Hugo Costa de  
Albuquerque (Advisor)  
Federal University of Ceará (UFC)

---

Prof. Dr. Renato William Rodrigues de Souza  
Federal Institute of Ceará (IFCE)

---

Prof. Dr. Leandro Aparecido Passos Junior  
São Paulo State University (UNESP)

I dedicate this work to my parents, Adenir Santos and Francisco Soares, to my brother, Júnior Soares and my girlfriend, Joyce Oliveira, for being essential in this journey.

## ACKNOWLEDGEMENTS

First to God, for allowing me to get this far, for all the strength and health to face the challenges, always with faith, effort and with the certainty that everything would work out, not letting me give up.

To my family, to my parents, Adenir Santos and Francisco Soares, for always being there, to my brother, Júnior Soares, for all the help during this journey, to my girlfriend, Joyce Oliveira, for encouraging, supporting and always being with me at all times, because without you I wouldn't get here.

To my friends, in particular, Renato William, for all the help even before starting the master's degree, as well as throughout this period.

To my friend Senthil Kumar for his help in translating the published articles and the dissertation.

To my advisor, Victor Hugo, for all the teachings during this journey, mainly for believing in my potential, not measuring efforts to get me this far.

To the Coordination for the Improvement of Higher Education Personnel – Brazil (CAPES / PROEX) for granting the scholarship in the first year of the master's course.

And my thanks to everyone who cheered and believed that I could make it this far.

“Uma gota no oceano ou um simples grão de areia podem mudar tudo.”

(Di Ferreira)

## ABSTRACT

Breast cancer is the type of cancer with the highest incidence and global mortality of female cancers. Thus, the adaptation of modern technologies that assist in medical diagnosis in order to accelerate, automate and reduce the subjectivity of this process is of paramount importance for an efficient treatment. Therefore, this work aims to propose a platform to compare and evaluate the proposed strategies for improving breast ultrasound images and compare them with state-of-the-art techniques by classifying them as benign, malignant, and normal. Investigations were performed on a dataset containing a total of 780 images of tumor-affected people, divided into benign, malignant, and normal. A data augmentation technique was used to scale up the corpus of images available in the chosen dataset. For this, novel image enhancement techniques were used and the Multilayer Perceptrons, k-Nearest Neighbor, and Support Vector Machines algorithms were used for classification. From the promising outcomes of the conducted experiments, it was observed that the image enhancement algorithm called bilateral together with the SVM classifier achieved the best result for the classification of breast cancer, with an overall accuracy of 96.69% and an accuracy for the detection of malignant nodules of 95.11%. Therefore, it was found that the application of image enhancement methods can help in the detection of breast cancer at a much earlier stage with better accuracy in detection.

**Keywords:** breast cancer; image enhancement; biomedical engineering.



## RESUMO

O câncer de mama é o de maior incidência e mortalidade entre os cânceres femininos. Assim, a adaptação de tecnologias modernas, que auxiliem no diagnóstico médico, são de fundamental importância para tornar o diagnóstico mais rápido e preciso. Dessa forma, este trabalho tem como objetivo propor uma plataforma para aplicar e analisar técnicas de realce de imagens, obtidas por ultrassom da mama, para avaliar a influência sobre a detecção do câncer baseada em técnicas de *machine learning*. Uma base de dados contendo 780 imagens, divididas em benignas, malignas e normais foi considerada. Devido a quantidade de imagens, utilizou-se a técnica *Data Augmentation* para ampliar a quantidade de imagens. Durante a análise dos resultados, foi observado que o algoritmo de realce denominado bilateral, combinado com o classificador SVM, obtiveram o melhor resultado para a detecção do câncer de mama, com uma precisão global de 96,69% e uma precisão para a detecção de nódulos malignos de 95,11%. Portanto, pode-se concluir que a aplicação de métodos de realce de imagem de ultrassom da mama é uma ferramenta complementar e promissora para detectar o câncer de forma rápida e precisa.

**Palavras-chave:** câncer de mama; aprimoramento de imagens; engenharia biomédica.

## LIST OF FIGURES

Figure 1 – Breast anatomy. . . . .	20
Figure 2 – Example of cancer. . . . .	21
Figure 3 – Example of screening and early diagnosis. . . . .	23
Figure 4 – Image Processing and Analysis. . . . .	24
Figure 5 – Example of the digital image acquisition process (a) Energy source. (b) An element of a scene. (c) Image acquisition system. (d) Projection of the scene onto the image plane. (e) Scanned image. . . . .	25
Figure 6 – Example of noise reduction. <b>a)</b> Image with noise <b>b)</b> application of noise reduction algorithm. . . . .	26
Figure 7 – Example deblurring. <b>a)</b> Shaky image <b>b)</b> application of deblurring algorithm. . . . .	27
Figure 8 – Dehazing example. <b>a)</b> Image with fog <b>b)</b> Application of dehazing algorithm. . . . .	28
Figure 9 – Segmentation example. <b>a)</b> Original image <b>b)</b> Application of segmentation algorithm <b>c)</b> Segmented image. . . . .	29
Figure 10 – Example of the feature extraction process. . . . .	30
Figure 11 – Example of the recognition and interpretation step. . . . .	31
Figure 12 – Sequence of stages involved in the proposed clinical decision-making system. . . . .	38
Figure 13 – Examples of images of each class. <b>a)</b> Normal <b>b)</b> Benign <b>c)</b> Malignant . . . . .	39
Figure 14 – Steps Exposure Fusion. . . . .	44
Figure 15 – Gamma Correction Flowchart. . . . .	46
Figure 16 – LD-NET architecture. . . . .	47
Figure 17 – Zero-DCE architecture. . . . .	48
Figure 18 – LLFLOW architecture. . . . .	49
Figure 19 – The confusion matrix highlighting the performance accuracy of the classification of mammogram images, with the diagonal elements in bold representing the true prediction labels. . . . .	54
Figure 20 – Normal highlighted mammogram images <b>a)</b> Original <b>b)</b> Bilateral <b>c)</b> Gamma correction <b>d)</b> HE <b>e)</b> LDNET <b>f)</b> LIME <b>g)</b> LLFLOW <b>h)</b> TV <b>i)</b> Ying <b>j)</b> Zero-DCE. . . . .	59
Figure 21 – Benign highlighted mammogram images <b>a)</b> Original <b>b)</b> Bilateral <b>c)</b> Gamma correction <b>d)</b> HE <b>e)</b> LDNET <b>f)</b> LIME <b>g)</b> LLFLOW <b>h)</b> TV <b>i)</b> Ying <b>j)</b> Zero-DCE. . . . .	60
Figure 22 – Malignant highlighted mammogram images <b>a)</b> Original <b>b)</b> Bilateral <b>c)</b> Gamma correction <b>d)</b> HE <b>e)</b> LDNET <b>f)</b> LIME <b>g)</b> LLFLOW <b>h)</b> TV <b>i)</b> Ying <b>j)</b> Zero-DCE. . . . .	61

Figure 23 – Global Accuracy: SVM Classifier Performance as Seen in Boxplot. . . . .	64
Figure 24 – Global Accuracy: k-NN Classifier Performance as Seen in Boxplot. . . . .	65
Figure 25 – Global Accuracy: MLP Classifier Performance as Seen in Boxplot. . . . .	65
Figure 26 – Confusion matrix for the combination of the Bilateral algorithm with the SVM classifier. . . . .	67
Figure 27 – Database images. (a) Normal image with region marked in red that resembles a benign nodule. (b) Image with a benign nodule. (c) Image with malignant nodule. . . . .	68
Figure 28 – Online web platform interfaces modules. (a) Main interface module (b) Module with images enhancement (c) Classification module with nodules (d) Nodule-free sorting module. . . . .	70

## LIST OF TABLES

Table 1 – Comparison of articles. . . . .	37
Table 2 – Base data of the images considered for analysis. . . . .	39
Table 3 – Comparison of processing time taken by image enhancement algorithms (in minutes). . . . .	57
Table 4 – Quality metrics for image enhancement algorithms. . . . .	58
Table 5 – Training and testing times of image enhancement algorithms and the classifiers.	62
Table 6 – Metrics for image enhancement algorithms. . . . .	66

## LIST OF ABBREVIATIONS AND ACRONYMS

AG	Average Gradient
AMBE	Absolute Mean Brightness Error
CAD	Computer-Aided Diagnosis
CNN	Convolutional Neural Network
CNR	Contrast-to-Noise Ratio
CT	Computed Tomography
CV	Computer Vision
DBT	Digital Tomosynthesis of the Breast
FN	False Negative
FP	False Positive
HE	Histogram Equalization
k-NN	k-Nearest Neighbor
LD-Net	Light-DehazeNet
LIME	Low-Light Image Enhancement via Illumination Map Estimation
LLFLOW	Low-Light Image Enhancement with Normalizing Flow
MLP	Multi-Layer Perceptron
MRI	Magnetic Resonance Imaging
PSNR	Peak Signal-to-Noise Ratio
RMSE	Root Mean Square Error
SSIM	Structural Similarity Index Measure
SVM	Support Vector Machine
TB	True Positive class Benign
TM	True Positive Malignant class
TN	True Positive Normal class
TV	Total Variance
VDSR	Very Deep Super Resolution
WHO	World Health Organization
Zero-DCE	Zero-Reference Deep Curve Estimation

## CONTENTS

<b>1</b>	<b>INTRODUCTION</b> . . . . .	<b>15</b>
<b>1.1</b>	<b>Objectives</b> . . . . .	<b>16</b>
<i>1.1.1</i>	<i>General objective</i> . . . . .	<i>16</i>
<i>1.1.2</i>	<i>Specific objectives</i> . . . . .	<i>16</i>
<b>1.2</b>	<b>Contributions</b> . . . . .	<b>17</b>
<b>1.3</b>	<b>Work organization</b> . . . . .	<b>17</b>
<b>1.4</b>	<b>Publications</b> . . . . .	<b>17</b>
<b>2</b>	<b>THEORETICAL FOUNDATION</b> . . . . .	<b>19</b>
<b>2.1</b>	<b>The Breast Cancer</b> . . . . .	<b>19</b>
<i>2.1.1</i>	<i>Breast anatomy</i> . . . . .	<i>19</i>
<i>2.1.2</i>	<i>Pathology and pathophysiology of breast cancer</i> . . . . .	<i>20</i>
<i>2.1.3</i>	<i>Breast cancer diagnosis</i> . . . . .	<i>22</i>
<b>2.2</b>	<b>Computer Vision</b> . . . . .	<b>23</b>
<i>2.2.1</i>	<i>Acquisition step</i> . . . . .	<i>24</i>
<i>2.2.2</i>	<i>Preprocessing step</i> . . . . .	<i>25</i>
<i>2.2.2.1</i>	<i>Denoise</i> . . . . .	<i>26</i>
<i>2.2.2.2</i>	<i>Deblurring</i> . . . . .	<i>27</i>
<i>2.2.2.3</i>	<i>Dehazing</i> . . . . .	<i>28</i>
<i>2.2.3</i>	<i>Segmentation step</i> . . . . .	<i>29</i>
<i>2.2.4</i>	<i>Feature extraction step</i> . . . . .	<i>30</i>
<i>2.2.5</i>	<i>Recognition and interpretation step</i> . . . . .	<i>31</i>
<b>2.3</b>	<b>Computer-aided diagnostic systems</b> . . . . .	<b>31</b>
<b>2.4</b>	<b>Related works</b> . . . . .	<b>32</b>
<i>2.4.1</i>	<i>Improvement</i> . . . . .	<i>32</i>
<i>2.4.2</i>	<i>Classification</i> . . . . .	<i>34</i>
<i>2.4.3</i>	<i>Classification using improvement methods</i> . . . . .	<i>35</i>
<i>2.4.4</i>	<i>Comparative analysis</i> . . . . .	<i>35</i>
<b>3</b>	<b>METHODOLOGY</b> . . . . .	<b>38</b>
<b>3.1</b>	<b>Database Description</b> . . . . .	<b>39</b>
<i>3.1.1</i>	<i>Data Augmentation</i> . . . . .	<i>40</i>
<b>3.2</b>	<b>Image Enhancement Techniques</b> . . . . .	<b>40</b>

3.2.1	<i>Bilateral</i> . . . . .	40
3.2.2	<i>Histogram Equalization</i> . . . . .	41
3.2.3	<i>Total Variance</i> . . . . .	42
3.2.4	<i>Low-Light Image Enhancement via Illumination Map Estimation</i> . . . . .	42
3.2.5	<i>Exposure Fusion</i> . . . . .	43
3.2.6	<i>Gamma Correction</i> . . . . .	46
3.2.7	<i>Light-DehazeNet</i> . . . . .	47
3.2.8	<i>Zero-Reference Deep Curve Estimation</i> . . . . .	48
3.2.9	<i>Low-Light Image Enhancement with Normalizing Flow</i> . . . . .	49
3.3	<b>Data Extraction</b> . . . . .	50
3.4	<b>Classification Methods</b> . . . . .	50
3.4.1	<i>Multi-Layer Perceptron (MLP)</i> . . . . .	50
3.4.2	<i>Support Vector Machine (SVM)</i> . . . . .	51
3.4.3	<i>k-Nearest Neighbor (k-NN)</i> . . . . .	51
3.5	<b>Statistical Metrics</b> . . . . .	51
3.5.1	<i>Quality Metrics</i> . . . . .	51
3.5.2	<i>Rank Metrics</i> . . . . .	53
3.6	<b>Experimental Configuration</b> . . . . .	56
4	<b>RESULTS AND DISCUSSION</b> . . . . .	57
4.1	<b>Image Enhancement</b> . . . . .	57
4.2	<b>Classification</b> . . . . .	62
4.3	<b>Online System/Web Interfaces</b> . . . . .	68
5	<b>CONCLUSIONS AND FUTURE WORK</b> . . . . .	72
	<b>REFERENCES</b> . . . . .	73

## 1 INTRODUCTION

It is reported that almost 24.2% of women with cancer in the world are affected by breast cancer each year, and 15% of deaths of female cancer-affected people are from patients with this type of cancer (LI, 2021). According to the World Health Organization (WHO), 2.3 million women were diagnosed with breast cancer in 2020, and a mortality of 685,000 was reported (MATIC; KADRY, 2022). In addition, as per the a study, it is anticipated that breast cancer cases will be increasing over the years and reach around 27 million in 2030 (AHMED; ISLAM, 2021).

Some patients have breast cancer cells but are asymptomatic, so frequent screening plays a vital role in detecting breast cancer before it becomes worse and progresses to subsequent stages (KHUMDEE *et al.*, 2021). To detect breast cancer, imaging tests can be used as well as biopsy, however, the biopsy is considered an invasive method, while imaging tests are more conservative (AFAQ; JAIN, 2022).

Among the imaging tests, the most commonly used breast cancer detection techniques are Mammogram, Ultrasound and Magnetic Resonance Imaging (MRI) (WANG *et al.*, 2020; WU *et al.*, 2022). Although imaging tests are fundamental in the identification and diagnosis of breast cancer, on several occasions, the tests are affected by noise, low contrast and other factors that impair the images and make it difficult to diagnose efficiently (HUANG *et al.*, 2019; MOSHREFI; NABKI, 2021).

Due to the challenges encountered in the early stage of accurate diagnosis of breast cancer, industry and academia have been involved in active research with the aim of proposing computational tools capable of performing a diagnosis automatically (SOUZA *et al.*, 2021).

The concept of Computer-Aided Diagnosis (CAD) is being increasingly used to assist in the medical analysis of various diseases, such as, vertebrae segmentation (QADRI *et al.*, 2022), diagnosis of Parkinson's disease (SOUZA *et al.*, 2021; AFONSO *et al.*, 2019), perception of the dynamics of blood flow to from static Computed Tomography (CT) angiography images (GAO *et al.*, 2020), detection and classification of multiclass skin lesions via teledermatology (KHAN *et al.*, 2021), EEG-based BCI rehabilitation (CAO *et al.*, 2022), recognition and detection of atrial fibrillation (CHEN *et al.*, 2022), detection of pulmonary nodules on CT scans (MESQUITA *et al.*, 2022), classification of oral cancer (HUANG *et al.*, 2022), as well as addressing security and efficient authentication for IoT applications in the medical field. In addition, research has been conducted on ways to improve the images (MOHAMED *et al.*, 2019; SINGH *et al.*, 2019; LATIF



*et al.*, 2020), segment the parts of interest (ZHAO *et al.*, 2022; JAHWAR; ABDULAZEEZ, 2022; DABASS *et al.*, 2019), and classify the nodes (CHEN *et al.*, 2021; BADAWY *et al.*, 2021; WANG *et al.*, 2020).

In this way, CADs systems seek to help physicians in decision-making, pointing out doubtful aspects in the images and bringing them to the attention of the radiologist, thus helping in the process of detecting diseases and reducing the reading of false negatives, providing less subjectivity in the diagnosis (PANDE; BHOYAR, 2022).

In view of this, ultrasound imaging plays a significant role in diagnosis, however, the judgment of the diagnosis of the disease based on ultrasound depends on the skill of the physician. Uninformative open ultrasound images lead to wrong conclusions on the part of the doctor (HOSSAIN *et al.*, 2022). Thus, the use of ultrasound in conjunction with improvement methods can provide lower cost and greater accessibility by people.

Thus, this research seeks to answer the following problem question: Can image enhancement methods improve the quality of breast ultrasound images and influence the classification?

## **1.1 Objectives**

In this topic, the general objective and specific objectives will be addressed.

### ***1.1.1 General objective***

This research has the general objective compare and evaluate image improvement methods in breast imaging ultrasounds, classifying them into benign, malignant, and normal images.

### ***1.1.2 Specific objectives***

As specific objectives, we have:

- Apply methods of image enhancement;
- Compare the methods applied;
- Evaluate their performance through quality metrics;
- Classify the images into three groups: normal, benign and malignant;
- Evaluate and validate the models used.

- Develop a platform to aid breast cancer doctors containing image enhancement and classification methods.

## 1.2 Contributions

Following are the principal contributions involved in this research:

- Development of a comparative analysis on the evaluation of breast cancer image enhancement methods to improve the accuracy in the detection of malignant tumors;
- Comparing different image enhancement techniques and classification techniques focused on breast tumor;
- Validating the results through statistical evaluations and estimating a better strategy for pre-screening of tumors;
- Developing Computer Assisted Diagnosis platform.

## 1.3 Work organization

This work is structured in five Chapter. The first one deals with the introduction, addressing the contextualization, problematic, justification, objectives, and contributions. The second chapter addresses the theoretical foundation, dealing with breast cancer, computer vision, Computer Aided diagnosis (CAD) and related works. Then, the third chapter presents the methods incorporated for the development of the research. the fourth Chapter addresses the results obtained in relation to image improvement and classification. Finally, the last Chapter summarizes the work with conclusions and notes on future work.

## 1.4 Publications

Some articles were published during the master's period. Among them, the first topic, which gave rise to this dissertation.

- DA SILVA, Daniel S. et al. Mammogram Image Enhancement Techniques for Online Breast Cancer Detection and Diagnosis. *Sensors*, v. 22, n. 22, p. 8818, 2022.
- ASTOLFI, Rodrigo S. et al. Computer-Aided Ankle Ligament Injury Diagnosis from Magnetic Resonance Images Using Machine Learning Techniques. *Sensors*, v. 23, n. 3, p. 1565, 2023.
- CHEN, Jiarong et al. Implementing ultra-lightweight co-inference model in ubiquitous

edge device for atrial fibrillation detection. *Expert Systems with Applications*, v. 216, p. 119407, 2023.

- XU, Gaowei et al. A compressed unsupervised deep domain adaptation model for efficient cross-domain fault diagnosis. *IEEE Transactions on Industrial Informatics*, 2022.
- CHEN, Jiarong et al. Edge2Analysis: a novel AIoT platform for atrial fibrillation recognition and detection. *IEEE Journal of Biomedical and Health Informatics*, v. 26, n. 12, p. 5772-5782, 2022.
- SOUSA, Fábio de O. et al. A Novel Virtual Nasal Endoscopy System based on Computed Tomography Scans. *Virtual Reality & Intelligent Hardware*, v. 4, n. 4, p. 359-379, 2022.

## 2 THEORETICAL FOUNDATION

This chapter is divided into four sections. The first section deals with breast cancer and its characteristics. In the second section, it discusses computer vision and its stages. In the third section, it deals with Computer-aided diagnostic (CAD) systems. Finally, in the third section, it deals with the related works.

### 2.1 The Breast Cancer

Among women, breast cancer accounts for 1 in 4 cancer cases and 1 in 6 cancer deaths, ranking first in incidence in the vast majority of countries (159 out of 185 countries) and in mortality in 110 countries (SUNG *et al.*, 2021). For Brazil, it is estimated that there are 66,280 new cases of breast cancer for each year of the 2020-2022 triennium. This value corresponds to an estimated risk of 61.61 new cases per 100,000 women (INCA, 2019b).

According to INCA (2019b) female breast cancer occupies the first position of most frequent in all regions of Brazil, without considering non-melanoma skin tumors, with an estimated risk of 21.34 per 100,000 in the North Region; 44.29 per 100,000 in the Northeast Region; 45.24 per 100,000 in the Midwest Region; 71.16 per 100,000 in the South Region; and 81.06 per 100 thousand in the Southeast Region.

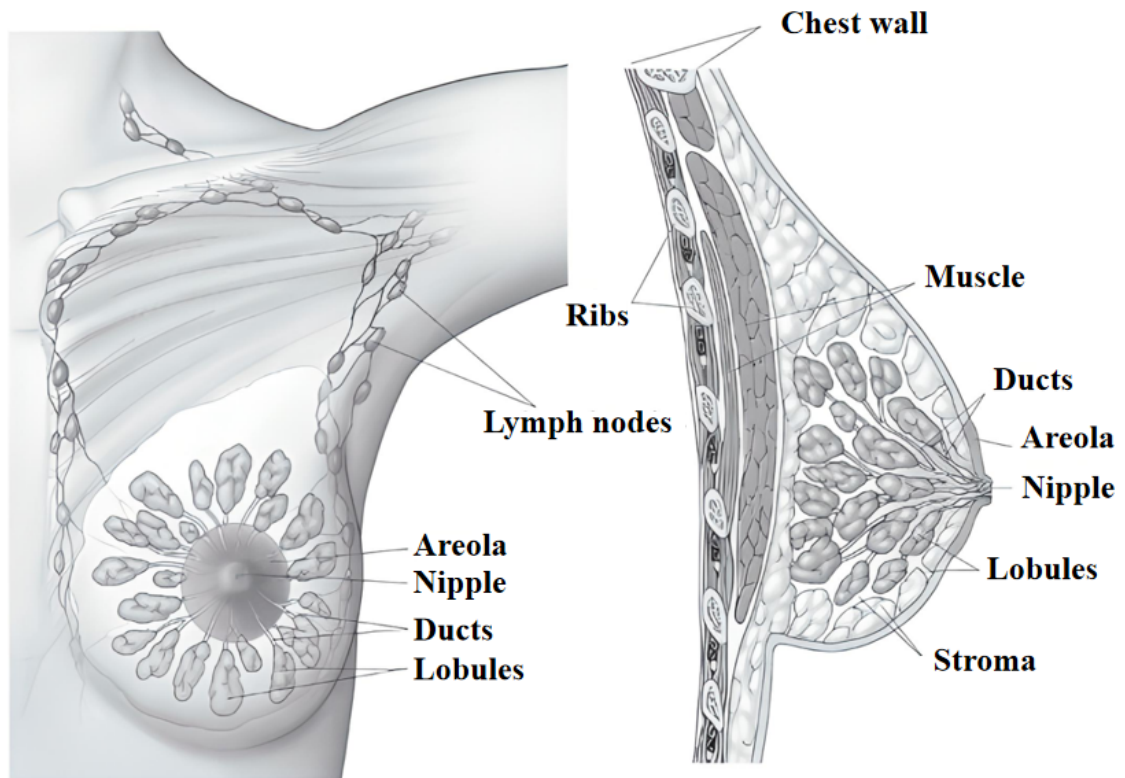
#### 2.1.1 Breast anatomy

The breasts are made up of glandular tissue and supporting fibrous tissue integrated into an adipose matrix, together with lymphatic vessels, blood vessels and nerves. They are superficial structures that, on the anterior chest wall, are more prominent, especially in women (MOORE *et al.*, 2014).

As shown in Figure 1, the breast has different parts, namely (ACS, 2021):

- Lobules: The lobules are the glands that produce breast milk.
- Ducts: The ducts are small channels that come out of the lobules and carry the milk to the nipple.
- Nipple: The nipple is the opening in the skin of the breast where the ducts join and become larger ducts so that the milk can leave the breast.
- Fat and connective tissue (stroma): These surround the ducts and lobules and help hold them in place.

Figure 1 – Breast anatomy.



## Normal breast tissue

Source: ACS (2021).

In addition, the breasts have several other structures, such as blood vessels, lymphatic vessels and nerve fibers.

### 2.1.2 Pathology and pathophysiology of breast cancer

Breast cancer has several possible causes. In view of this, several factors have been and still continue to be studied with the aim of analyzing and understanding the relationship with the risk of developing the disease (INCA, 2021; WEIDERPASS; STEWART, 2020). Thus, the factors well established in the literature are:

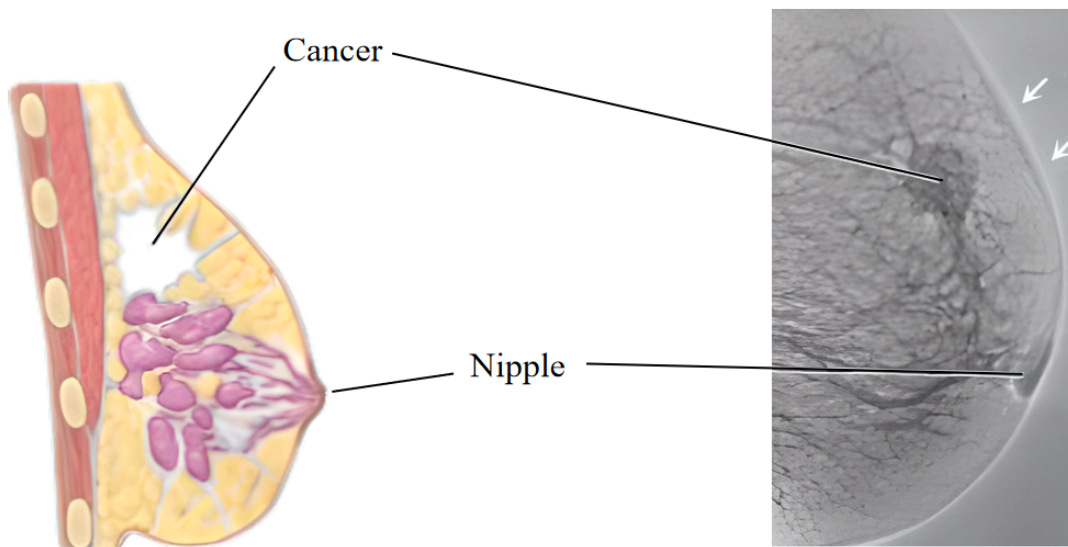
- Age: Women aged 50 and over have a higher risk of developing breast cancer. Thus, as the years go by, the probability of contracting cancer increases.
- Behavioral and environmental factors: Factors such as alcohol intake and overweight and obesity after menopause are factors that can cause breast cancer.
- Heredity: Factors such as the presence of mutations in certain genes.

- Endocrine factors and reproductive history: Some factors such as recent use of oral contraceptives (estrogen-progesterone), exposure to the hormone estrogen as well as late menopause (after age 55).

Generally, breast cancers are epithelial and non-epithelial supporting stromal tumors. Most are epithelial tumors that develop from cells lining lobules or ducts, while non-epithelial cancers of the supporting stroma are less common and originate from the connective tissues that support the epithelial cells of the breast, such as muscles, blood vessels, lymphatics, and adipose tissue. (CHOI, 2022).

Cancers are divided into two types, carcinoma in situ and invasive cancer. Carcinoma in situ, which can be ductal or lobular, is characterized by the proliferation of cancer cells within ducts or lobules and without invasion of stromal tissue, whereas invasive cancer is an adenocarcinoma (MENKE *et al.*, 2007; CHOI, 2022). In Figure 2, a demonstration of cancer can be seen.

Figure 2 – Example of cancer.



Source: Adapted from MOORE *et al.* (2014).

The cancer usually spreads through the lymph vessels (lymphatic metastasis), which carry cancer cells from the breast to the lymph nodes, especially those in the armpit. The cells settle in the lymph nodes, creating foci of cancerous cells (metastases). The most common site of breast cancer metastasis is in the axillary lymph nodes, as this is where most of the lymphatic drainage from the breast is destined, but it can affect almost all organs in the body, the most common being the lungs, liver, bones, brain and skin. (MOORE *et al.*, 2014).

When there is enlargement of these palpable lymph nodes, it suggests that there is a possibility of breast cancer and can help detect cancer early. However, when these enlarged axillary lymph nodes are not present, there is no guarantee that the breast cancer has not spread. Malignant cells can migrate to other lymph nodes, such as supraclavicular and subclavian lymph nodes (MOORE *et al.*, 2014).

Thus, the main radiological signs of malignancy are calcifications, nodules, asymmetries, neodensities, distortions, architectural and isolated ductal dilations (INCA, 2019a). The most common sign of breast cancer is the fixed nodule, usually hard, painless, and irregular, which is an expansive lesion that can be evaluated according to size, shape, margin and density (INCA, 2021; INCA, 2019a).

### **2.1.3 Breast cancer diagnosis**

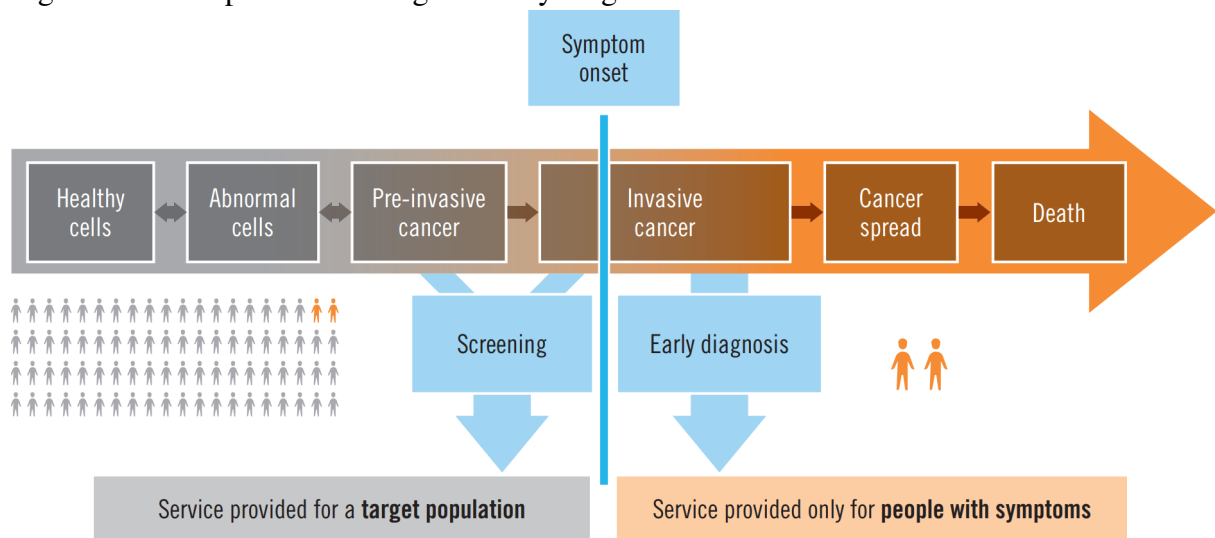
The World Health Organization recommends actions for prevention, early detection and access to treatment for cancer control (WHO, 2017). Among these actions, early detection is treated with greater importance and attention by the population and the media, considering that the earlier the cancer is identified, the greater the patient's chance of cure (INCA, 2021).

Early cancer detection encompasses two types of strategies, screening and early diagnosis. Screening seeks to find precancerous lesions or preclinical cancer by carrying out routine examinations in a target population without signs and symptoms suggestive of the screened cancer, while early diagnosis aims to identify early-stage cancer in people who already have suspicious symptoms and signs of cancer, such as a hardened and fixed breast lump, presence of axillary lymphadenopathy, breast skin retraction, among others (INCA, 2021; WHO, 2017). It can be observed, in Figure 3, the example of tracking and early diagnosis.

There are some tests that can be used to screen for breast cancer, such as mammography, ultrasound and magnetic resonance imaging. Mammography is still the most effective form of imaging for early detection of changes in the breasts, even those that are so small that they go unnoticed in awareness and clinical examination (INCA, 2019a).

Although mammography is the most important method, both for screening and for diagnosing breast cancer, and is the only imaging method that has already been shown to contribute to reducing mortality from breast cancer, it has some limitations and does not allow detection of all types of cancer, notably in women with dense breasts and in high-risk women with a mutation in the breast cancer suppressor gene (INCA, 2021; INCA, 2019a).

Figure 3 – Example of screening and early diagnosis.



Source: WHO (2017).

Thus, other exams can be used, such as ultrasonography, which are also performed because they have a relatively lower cost, their performance is not affected by dense tissues, as in mammography, they do not require the use of ionizing radiation, they have the ability to examine images in real time, in addition, not having the need to compress the breast to perform the exam (WEIDERPASS; STEWART, 2020; VOCATURO; ZUMPANO, 2021). However, one of the problems with this type of ultrasound examination is the low quality of the image and the presence of noise (MISRA *et al.*, 2022).

Thus, to alleviate these limitations, alternatives can be used, such as performing other tests together, as well as using other technological and computational ways that can contribute to a more accurate diagnosis (WHO, 2017; WEIDERPASS; STEWART, 2020; VOCATURO; ZUMPANO, 2021; MISRA *et al.*, 2022).

## 2.2 Computer Vision

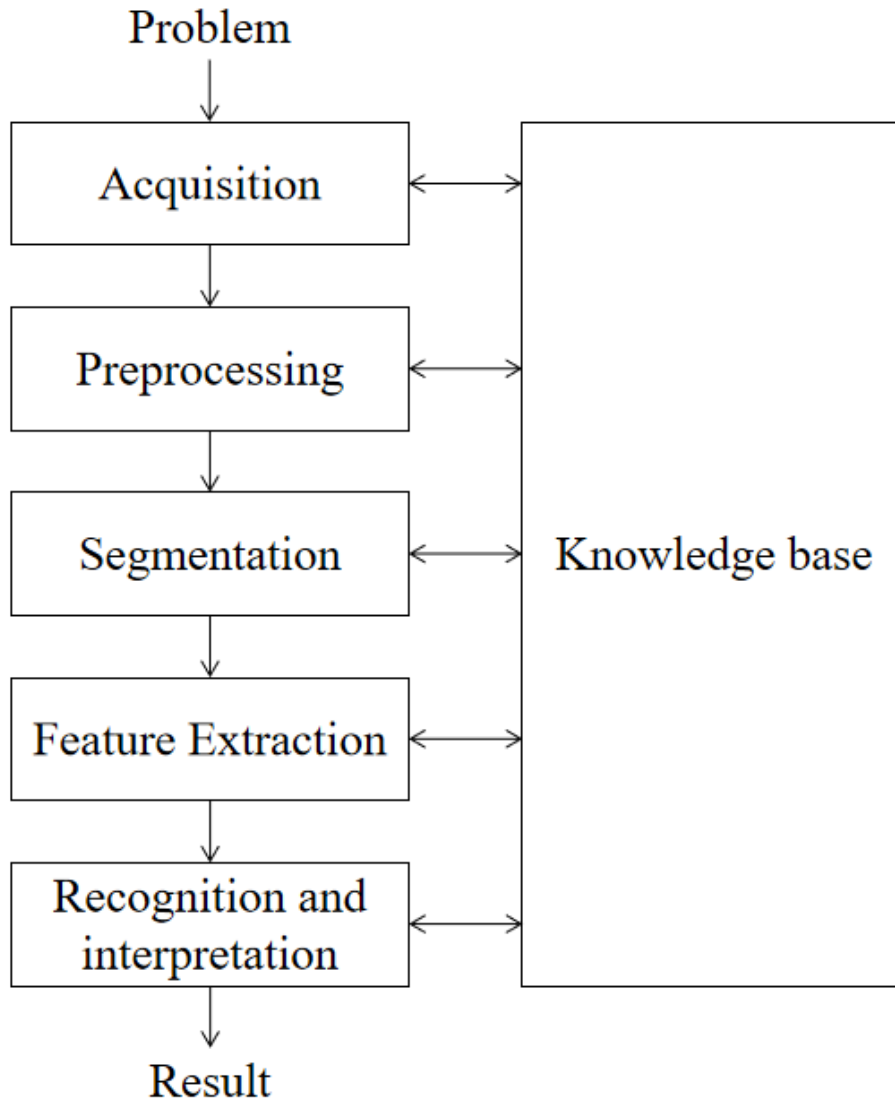
Computer Vision (CV), also known as Artificial Vision, is a subarea of artificial intelligence that seeks to acquire, process, extract and interpret images corresponding to real scenes (TRINKS; FELDEN, 2020). Its main steps are acquisition, pre-processing, segmentation, feature extraction and recognition and interpretation (MARQUES FILHO; VIEIRA NETO, 1999).

The execution of all activities in the mentioned stages requires prior knowledge about the problem to be solved. This knowledge is stored in a knowledge base, which can vary



significantly in size and complexity. It is desirable for this knowledge base to not only guide the functioning of each stage but also allow for feedback between them. In Figura 4 the flow of steps is presented.

Figure 4 – Image Processing and Analysis.



Source: MARQUES FILHO; VIEIRA NETO (1999).

In this way, each step has activities and processes that, when completed and the final results obtained, will be passed on to the following steps. Such steps can be observed in the following subsections.

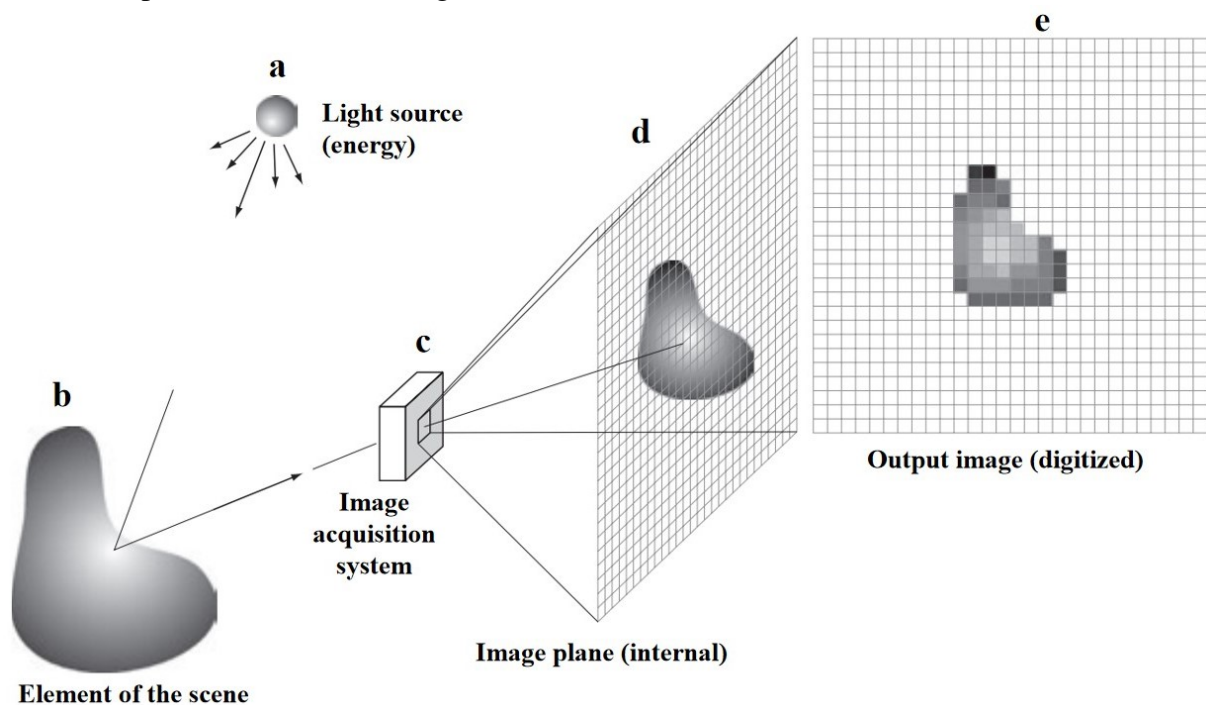
### **2.2.1 Acquisition step**

The acquisition stage deals with the capture of images by means of a sensor or device such as medical tomographs, digital cameras, among others (OLIVEIRA, 2014). Among

the design aspects involved in this step, one can consider the type of sensor, the lighting conditions, the lenses used, as well as the resolution and number of gray levels of the scanned image (MARQUES FILHO; VIEIRA NETO, 1999).

To perform image acquisition, single sensors, line scan sensors and matrix sensors can be used. Image acquisition using matrix sensors is the type of sensors predominantly found in digital cameras (GONZALEZ; WOODS, 2010). In Figure 5 an example of acquisition from matrix sensors (digital image) is presented.

Figure 5 – Example of the digital image acquisition process (a) Energy source. (b) An element of a scene. (c) Image acquisition system. (d) Projection of the scene onto the image plane. (e) Scanned image.



Source: GONZALEZ; WOODS (2010).

Figure 5 shows the energy of a light source (a) being reflected from an element of a scene (b). The image acquisition system (c) collects the input energy and projects it onto an image plane (d), producing a digital image output (e) (GONZALEZ; WOODS, 2010).

### 2.2.2 Preprocessing step

After the image is obtained, pre-processing is the next step. The main function of pre-processing is to improve the quality of the image in order to facilitate the processes of later stages (MARQUES FILHO; VIEIRA NETO, 1999). In this stage, the images are improved by

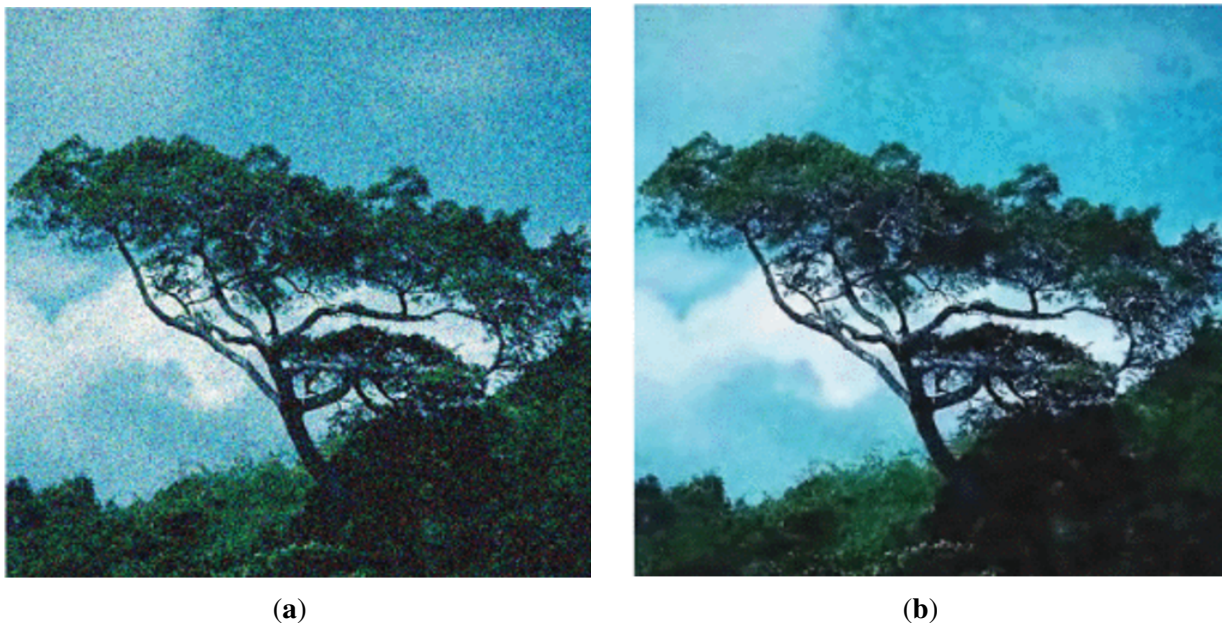
enhancing contrasts and brightness, removing noise, among others (GONZALEZ; WOODS, 2000).

The restoration of these acquired images is extremely important in the pre-processing stage, some tasks such as denoising, deblurring and dehazing are used to try to soften the noise and interference, seeking to restore a degraded image to a clean image (CHU *et al.*, 2022).

### 2.2.2.1 Denoise

Noise corrupts virtually any image captured by a camera (KATTAKINDA; RAJAGOPALAN, 2020). The elimination of image noise is one of the problems widely studied in the area of computer vision and image processing, aiming to reduce the noise intensity, in order to preserve the content of the original image (KUMWILAISAK *et al.*, 2020). In Figure 6 an example of applying a denoise algorithm to an image with noise is presented.

Figure 6 – Example of noise reduction. **a)** Image with noise **b)** application of noise reduction algorithm.



Source: Adapted from KATTAKINDA; RAJAGOPALAN (2020).

There are several noise reduction methods for different noises (Gaussian, salt and pepper, speckle) and different types of images such as, for example, filter algorithms (mean, median, Gaussian) as well as the most recent algorithms based on Convolutional Neural Network (CNN) (YU *et al.*, 2019).

The denoise algorithms, however, can cause blurring in the image, as well as loss of

detail at the edges, depending on the algorithm used, amount of noise and the image used, as can be seen in Figure 6b (YANG *et al.*, 2018; YU *et al.*, 2019; LIU; MA, 2020).

#### 2.2.2.2 Deblurring

Blur is generated due to the accumulation of optical signals captured by the sensor during the exposure time and is one of the most common artifacts of digital images. It usually occurs when objects in captured scenes are moving, or the camera does not find focus, or the camera is held unsteadily, or objects in the scene are moving rapidly during the exposure time period (LIANG *et al.*, 2022; BAI *et al.*, 2020).

Image deblurring is a fundamental process in many computer vision applications and can be used in many situations (GONG; ZHANG, 2019). In Figure 7 you can see the example of the use of deblurring algorithms.

Figure 7 – Example deblurring. a) Shaky image b) application of deblurring algorithm.



Source: Adapted from ZHANG *et al.* (2020).

Deblurring algorithms can be categorized into two types, those based on single images and those based on multiple images. Single-image deblurring algorithms have made considerable advances in handling the misplaced deblurring problem by utilizing various previous statistics while multi-image-based algorithms aim to deal with the highly misplaced problem by fusing complementary information from multiple blurred images (ZHANG *et al.*, 2019).

However, both approaches have points to be considered, since single-image deblurring algorithms are difficult to obtain optimal results, since part of the information is lost in the deblurring process, in addition to their computational load being, generally, quite high. Multi-image algorithms usually take into account that all images are well aligned, which does not happen in practice, in addition, few deblurring algorithms consider the influence of exposure time on the deblurring process. (ZHANG *et al.*, 2019; AGRAWAL *et al.*, 2009)

### 2.2.2.3 Dehazing

The quality of images may be affected due to fog, smoke, impurities in the air, as well as other factors that influence images indoors or outdoors (XIE *et al.*, 2020). In this way, Dehazing algorithms can improve the problems of several applications based on image processing and computer vision, as it helps in improving the visibility of the scene. Removing fog from an image can eliminate unwanted visual effects in many types of images (ABIN *et al.*, 2021).

You can see in Figure 8 an example of using dehazing. In Figure 8a, it is the image with fog or haze, while in Figure 8b the image after applying the dehazing algorithm.

Figure 8 – Dehazing example. **a)** Image with fog **b)** Application of dehazing algorithm.



Source: Adapted from MIN *et al.* (2019).

Existing dehazing methods formulate haze removal as an image composition problem,

dividing into prior-based and data-driven. Prior-based algorithms seek to estimate factors such as depth and atmospheric light based on various assumptions or premises. However, since these methods assume that the haze follows certain assumptions or premises, they can easily be violated by the complexity of the scene (ZHU *et al.*, 2021; RAIKWAR; TAPASWI, 2020).

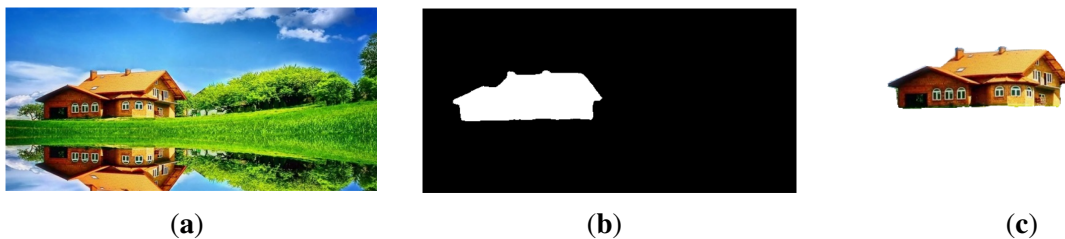
Data-drive methods were developed to deal with the disadvantages of prior-based, using deep neural networks instead of a shallow model, such as convolutional neural networks (CNNs), to learn discriminative features of raw data and regress the physical parameters. However, like the prior-based methods, it has some disadvantages, as these methods show suboptimal results, given that image retrieval and parameter estimation are treated as two separate steps, and errors can accumulate (ZHENG *et al.*, 2020; ZHU *et al.*, 2021).

### 2.2.3 Segmentation step

After the image is acquired and passed through the pre-processing step, applying all the improvements, the segmentation step will be performed. The segmentation step deals with the division of an image into its significant units, that is, into the objects of interest that compose it (GONZALEZ; WOODS, 2000).

In Figure 9 an example of the use of segmentation in an image is presented, in which only the object of interest is removed, disregarding the rest of the image (image background).

Figure 9 – Segmentation example. **a)** Original image **b)** Application of segmentation algorithm **c)** Segmented image.



Source: Adapted from FACCIO (2020).

Segmentation is used for various purposes and areas of knowledge such as document processing, object recognition, remote sensing image, biomedicine, among others (CORONEL *et al.*, 2018).

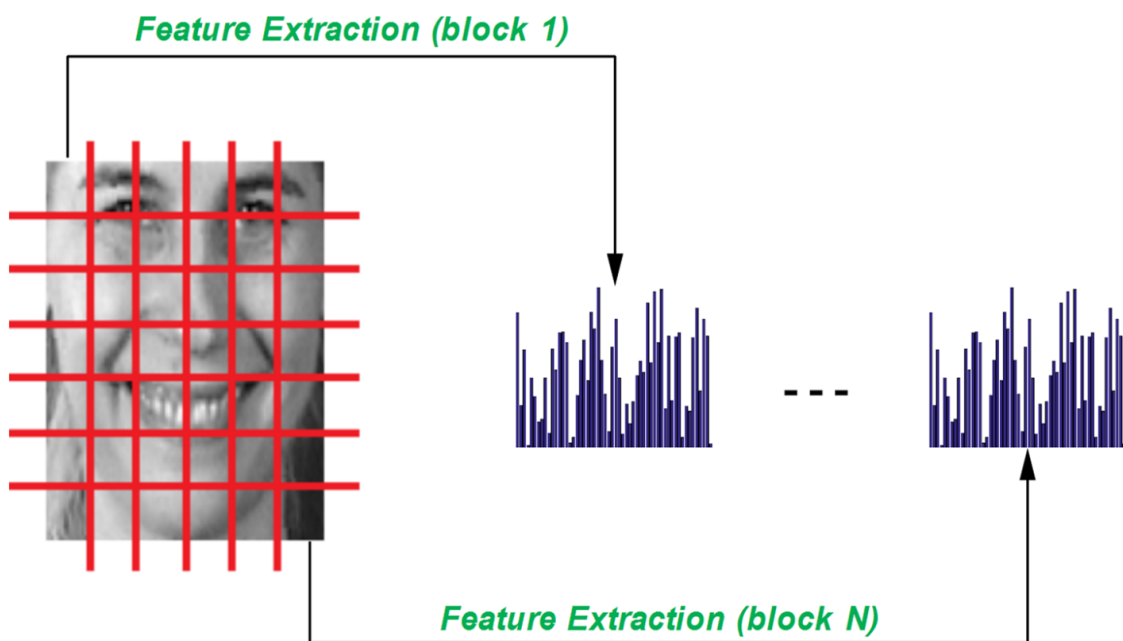
It should be considered, however, that the segmentation algorithms may present some limitations to separate only the area of interest (PANG *et al.*, 2021; LIN *et al.*, 2019). Depending

on the image, degree of noise, similarity between the object of interest and the background, information can be lost at the time of segmentation, as well as separating objects that are not part of the object of interest (CHENG; LI, 2021; YIN *et al.*, 2020).

#### 2.2.4 Feature extraction step

The image feature is actually the key information in the image content, and the image feature extraction is the key information extraction process (CHENG *et al.*, 2020). Thus, the feature extraction step seeks to extract information from the images that can characterize, through descriptors, the analyzed object (MARQUES FILHO; VIEIRA NETO, 1999). Figure 10 shows an example of extracting features from an image.

Figure 10 – Example of the feature extraction process.



Source: SADEGHI; RAIE (2019).

In this step, the input is still an image from the previous steps, however, the output is a set of characters, whether text, numbers, or other representations (GONZALEZ; WOODS, 2018).

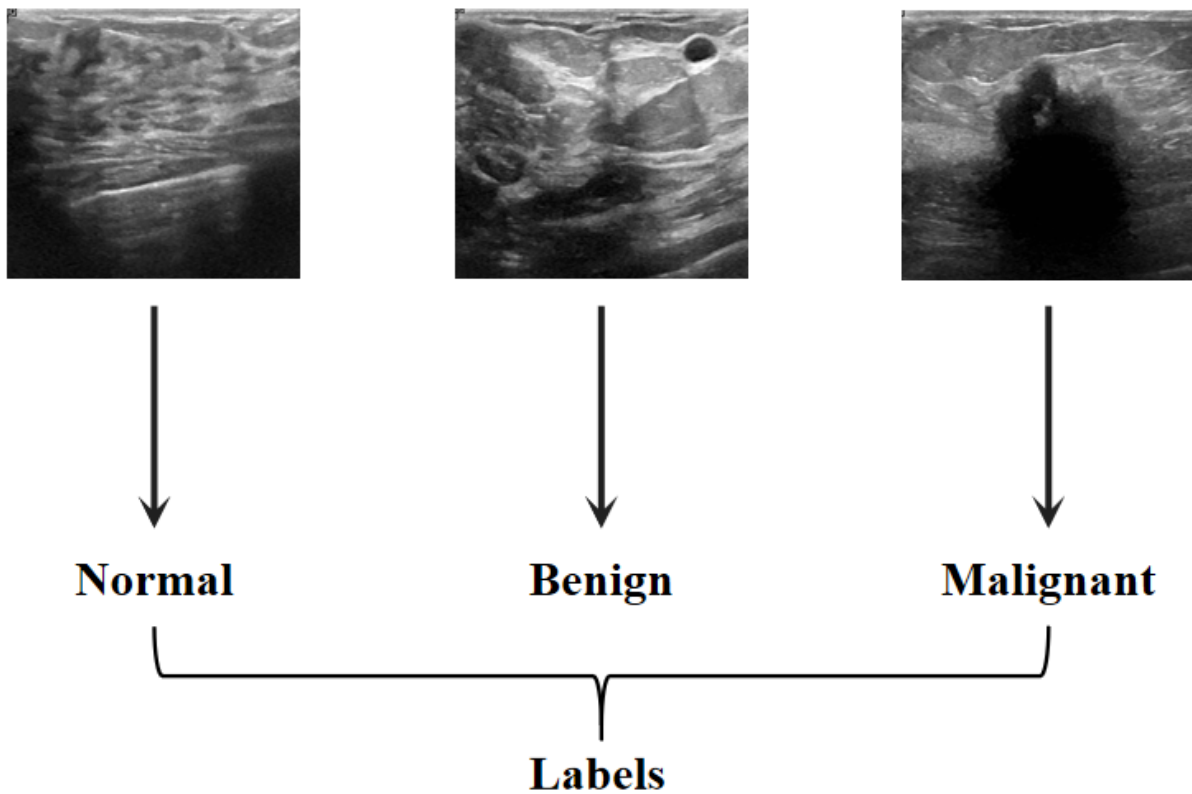
In this way, several resources can be extracted from the images, such as textures, colors and shapes (KARTIKA *et al.*, 2020). The algorithms used to extract these features can be both traditional algorithms and algorithms based on CNN, in addition, a combination of both can also be performed (QUAN *et al.*, 2020).

### 2.2.5 Recognition and interpretation step

The last step to be used is recognition and interpretation. At this stage, recognition seeks to assign a label to an object, while interpretation deals with assigning meaning to a set of recognized objects (GONZALEZ; WOODS, 2000).

In this way, the classification and selection is carried out through pattern recognition, based on the characteristics presented by the descriptors provided by the previous step (GONÇALVES, 2016).

Figure 11 – Example of the recognition and interpretation step.



Source: Elaborated by the author (2023).

Figure 11 shows the labeling of the images according to the total number of classes in the problem. In this way, there are several algorithms that can perform the classification of information, in order to learn the patterns and be able to identify automatically (LI *et al.*, 2020).

## 2.3 Computer-aided diagnostic systems

Computer-aided diagnostic systems are introduced in the field of medicine in order to allow doctors and specialists to perform clinical diagnoses more accurately with the help of



modern science and technology, saving time and improving the accuracy of diagnostic results, as well as supporting experienced clinicians in their daily work, minimizing human error and subjectivity. (ZHANG; LI, 2021; NAPIER *et al.*, 2019).

The main components of these CAD systems usually include pre-processing, segmentation, feature extraction and classification (detection/diagnosis) steps. Among the components, classification is often considered the core of the CAD system (WANG *et al.*, 2020).

Various types of medical images can be used as input to CAD systems, such as X-rays, CT scans, ultrasound images, MRIs, mammography, among others (KUMAR *et al.*, 2020). In addition, different platforms can be used for CAD systems such as web, desktop and mobile platforms (MEMARI; MOGHBEL, 2020; DULF *et al.*, 2021).

## 2.4 Related works

Several studies have been proposed in recent years with the aim of proposing methods for improving, extracting and classifying breast cancer images. In view of this, we searched in 2022 and 2023 for articles published in IEEE Xplore, Springer and Science Direct, related to new methods and algorithms for improvement, extraction and classification applied to breast cancer.

### 2.4.1 Improvement

Authors KIM *et al.* (2023) have proposed a generative adversarial network to synthesize contrast-enhanced T1-weighted MRI (ceT1) from pre-contrast (pre-T1) T1-weighted breast MR images. who adopted a local discriminator and a network of segmentation tasks to specifically focus on the tumor region in addition to the entire breast. Thus, the objective is to generate ceT1 images from pre-T1 images. For this purpose, images from Samsung Medical Center (SMC) and Gil Hospital (GH) were used. Four normalized mean squared error (NRMSE) evaluation metrics, Pearson's cross-correlation coefficients (CC), peak signal-to-noise ratio (PSNR) and structural similarity index (SSIM) map were used for the entire breast and region. tumor. With that, the proposed method reaches NRMSE of 25.65, PSNR of 54.80 dB, SSIM of 0.91 and CC of 0.88, on average.

The authors SULAIMAN *et al.* (2022) sought to develop an approach based on deep learning to enhance Digital Tomosynthesis of the Breast (DBT) images. The Very Deep Super

Resolution (VDSR) approach was used with three different types of optimizers which are Adam, RMSPROP and SGDM. The database used was the VICTRE trial: Open-source. To validate the method, the peak signal noise ratio (PSNR), the Structural Similarity Index Method (SSIM) and the Naturalness Image Quality Evaluator (NIQE) were used. Thus, the authors reached as a result the PSNR of 40.3274, SSIM of 0.9562 and NIQE of 9.5511.

The authors BABU; JEROME (2022) sought to investigate and identify the most appropriate noise removal filter and the improvement technique between mean, median, adaptive median, Gaussian, wiener, contrast stretching, equalization of histogram and contrast-limited adaptive histogram equalization (CLAHE) for the mammography images. For that, it used the MIAS database to perform the tests. Thus, for validation, the Mean Square Error (MSE), Peak Signal-to-Noise Ratio (PSNR) and Structural Similarity Index (SSIM) metrics were used. Thus, the methods that obtained the best results were the adaptive median filter with 0.5828 of MSE, 48.8351 of PSNR and 0.9912 of SSIM, on average, and the histogram equalization with 46.1515 of MSE, 20.08 of PSNR and 0.76145 of SSIM.

HARRON *et al.* (2022) presented a denoise technique for use in digital breast tomosynthesis (DBT) images using a deep learning model. The new technique will use a multiscale context aggregation network (MS-CAN) to learn how to reduce image noise. To test the proposed technique, he used the base proposed by BUDA *et al.* (2020). To validate the method used the peak signal noise ratio (PSNR), Structural Similarity Index Method (SSIM) and Naturalness Image Quality Evaluator (NIQE) metrics. The best result used the sgdm optimizer reaching 26.5439 of PSNR, 0.16126 of SSIM and 9.70889 of NIQE.

The authors SAIFUDIN *et al.* (2022) proposed an enhancement method based on Non-Linear Unsharp Masking (NLUM) filters. NLUM needs a filter to complete the non-linear element in the algorithm like Median Filter in conventional NLUM, however, you can use and adapt other filters like Hybrid Maximum Filter (H3F) and Hybrid Sigma Filter (H4F) to replace the conventional filter. To test the method, the database tal was used. Mean Square Error (MSE), Peak Signal to Noise Ratio (PSNR) and Structural Similarity Index Measure (SSIM) are used for validation. The results show that the H4F is the best filter between the conventional and the H3F to adapt to the NLUM with 0.01976, 66.399 and 0.9417, on average, of MSE, PSNR and SSIM.

### 2.4.2 Classification

PATEL *et al.* (2023) proposed an adaptive regularized learning based on deep network graphs, called GARL-Net, for breast cancer classification. Transfer learning was used to train the DenseNet121 backbone network. For the tests, three datasets (BreakHis, BACH-2018 and mixed) with benign and malignant classes were used. With this methodology employed, it reached a percentage of 99.00% precision, 99.40% recall, 99.20% F-1score and 99.49% accuracy, with the BreakHis base.

Already XU *et al.* (2023) have developed a Regional-attentive Multi-Risk Learning framework (RMTL-Net) to simultaneously segment tumor regions and classify tumors in breast ultrasound images into benign and malignant. In addition, they designed a regional attention (RA) module that employs the predicted probability maps to automatically guide the classifier to learn important category-sensitive information in the tumor, peritumoral, and background regions and thus merge them seamlessly to obtain a better representation of resources. For the experiments, two sets of breast ultrasound data, UDIAT and BSU, were used. The authors achieved a hit rate of 96.32% for sensitivity, 81.64% for specificity, 91.94% for precision, 91.44% for accuracy and 93.85% for F1-score.

The authors WANG *et al.* (2023) proposed a new structure called multicenter transformation between unified capsules (MLT-UniCaps). The MLT-UniCaps is composed of Attention Pose Embedding, Dynamic Source Capsule Traversal, and Adaptive Target Capsule Fusion in order to perform intelligent remote assistant diagnosis. Embedding attention poses extract feature vectors through variations in position, orientation, scale, and lighting as poses through an adversarial convolutional neural network with an attention-based layer. For that, three sets of data were used, the DDSM, CBIS-DDSM and MIAS. Thus, they achieved 88.1% precision, 94.3% recall, 91.1% F1-score and 90.1% accuracy.

LOIZIDOU *et al.* (2022) presented a method based on the subtraction of temporally sequential digital mammograms and on machine learning for the automatic segmentation and classification of masses. To this end, they created a database including sequential digital mammograms and notes of each mass and implemented a Synthetic Minority Oversampling (SMOTE) technique for data augmentation. With that, he applied different types of extractors and classifiers to test the best combination. Thus, the best results achieved were with Neural Network, reaching an accuracy of 97.97%, sensitivity of 98.96% and specificity of 96.15%.

The authors LIU *et al.* (2022) proposed a new framework for classifying breast

pathology, called the AlexNet-BC model, in order to alleviate the problem of overfitting for better classification accuracy. Furthermore, they devised an improved cross-entropy loss function to penalize overconfident low-entropy output distributions and make predictions suitable for uniform distributions. For the tests, the BreKHis, IDC and UCSB databases were used. Thus, the new method reached a percentage of 98.48% of accuracy.

### **2.4.3 Classification using improvement methods**

KHAN *et al.* (2022) introduced a domain adaptive model based on multiscale feature fusion for breast cancer classification using histopathology images. Thus, the objective is to extract features from images based on multiscale inputs, using heterogeneous models to extract different features for better classification of complex images. In addition, the local window-based CLAHE contrast enhancement technique is used to increase foreground and background contrast as well as remove noise. To carry out the experiments, the BreKHis dataset was used. Thus, the model proposed by the authors achieved a rate of 98.00% precision, 98.15% recall, 98.08% F1-score and 98.23% accuracy.

ISKANDAR *et al.* (2022) proposed an image processing method to pre-process mammography images for detection and classification of breast cancer using CNN. Otsu thresholding, median filtering, CLAHE and truncation normalization were used. The INbreast dataset was used for testing together with private images from the Husada Hospital located in Jakarta, in addition to applying the data argumentation technique. With this, a CNN is used to provide a positive and negative diagnosis from the mammography images. Thus, the best result achieved obtained 94.1% accuracy, 100.0% precision and 85% sensitivity in classifying mammography images as benign or malignant.

### **2.4.4 Comparative analysis**

It is noticed that the works approached seek to analyze an aspect such as just the improvement or just the classification. The works of KIM *et al.* (2023), SULAIMAN *et al.* (2022), BABU; JEROME (2022), HARRON *et al.* (2022), SAIFUDIN *et al.* (2022) proposes new methods or compares existing methods to perform image enhancement, using quality metrics to validate them. However, they did not analyze the effect of ranking enhancement.

The works of PATEL *et al.* (2023), XU *et al.* (2023), WANG *et al.* (2023), LOIZIDOU *et al.* (2022), LIU *et al.* (2022) developed new methods to perform classification,

using classification metrics to validate them. What you can notice is that the authors did not use improvement methods, unlike the authors KHAN *et al.* (2022) and ISKANDAR *et al.* (2022) who both did the classification and applied an improvement method. Although the authors KHAN *et al.* (2022), and ISKANDAR *et al.* (2022) applied an improvement method, they did not analyze with quality metrics, only ranking metrics.

Among the works approached and analyzed, only that of XU *et al.* (2023) developed an IoT platform to use his method online. Thus, the Table 1 presents a summary of information on related works.

Table 1 – Comparison of articles.

Authors	Dataset used	Improvement method	Classification method	IoT platform	Results Quality	Results Classification
Kim et al. (2023)	Private base: SMC and GH	YES, new method	NO	NO	NRMSE: 25.65, PSNR: 54.80, SSIM: 0.91, CC: 0.88.	NO
Sulaiman et al. (2022)	VICTRE trial: Open-source	YES, new method	NO	NO	PSNR: 40.32, SSIM: 0.95, NIQE: 9.55.	NO
Babu and Jerome (2022)	MIAS	YES, method comparison	NO	NO	MSE: 0.58, PSNR: 48.83, SSIM: 0.99.	NO
Harron et al. (2022)	Basis proposed by Buda et al. (2020)	YES, new method	NO	NO	PSNR: 6.54, SSIM: 0.16, NIQE: 9.70	NO
Saifudin et al. (2022)	private base	YES, method comparison (Median filter, H3F and H4F)	NO	NO	MSE: 0.019 PSNR: 66.39 SSIM: 0.94	NO
Patel et al. (2023)	BreakHis, BACH-2018 e mixed	NO	YES, CNN com GARL-Net	NO	NO	Acc: 99.49%, Prec: 99%, Rec: 99.40%, F1s: 99.49%.
XU et al. (2023)	UDIAT e BSU	NO	YES, RMTL-Net	YES	NO	Acc: 91.44%, Prec: 91.94%, Sen: 96.32%, Esp: 81.64%, F1s: de 93.85%.
Wang et al. (2023)	DDSM, CBIS-DDSM e MIAS	NO	YES, NLT-UniCaps	NO	NO	Acc: 90.1%, Prec: 88.1%, Rec: 94.3%, F1s: 91.1%.
Loizidou et al. (2022)	Private base	NO	YES, NN	NO	NO	Acc: 97.97%, Sen: 98.96%, Esp: 96.15%.
Liu et al. (2022)	BreakHis, IDC e UCSB	NO	Yes, AlexNet-BC	NO	NO	Acc: 98.48%.
Khan et al. (2022)	BreakHis	YES, CLAHE	Yes, new model	NO	NO	Acc: 98.23% Prec: 98%, Rec: 98.15%, F1s: 98.23%.
Iskandar et al. (2022)	INbreast	YES, CLAHE	Yes, CNN	NO	NO	Acc: 94.1%, Prec: 100%, Sen: 85%.

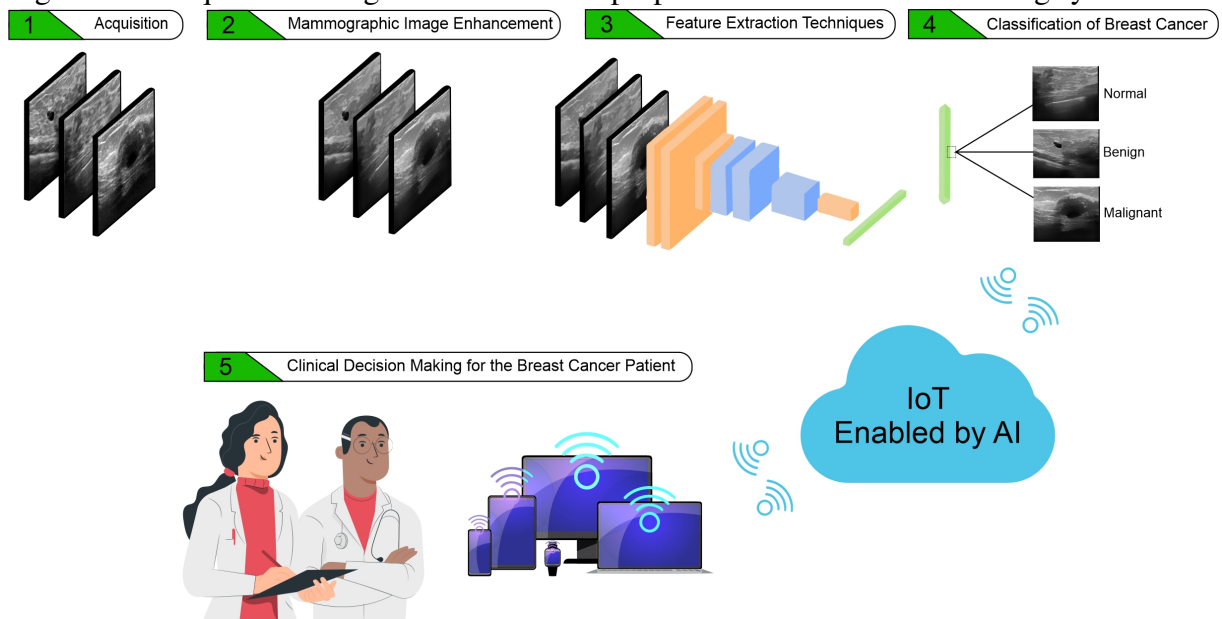
Source: Elaborated by the author(2022).

### 3 METHODOLOGY

In this chapter, the application steps of the proposed system will be presented, covering the web platform, the image enhancement algorithms, the feature extraction method, the classifiers, as well as the validation metrics, and the experimental settings used in this study. Figure 12 shows the sequence of stages involved in the automated pre-screening of breast tumors using the proposed clinical decision-making system.

From the perspective of providing an interactive environment for screening tumor-affected patients, the proposed Web platform was built using HTML 5 and CSS 3 for the front-end interactive part with users, and the Flask micro-framework as a fast and lightweight development tool for the back-end design (YAGANTEESWARUDU, 2020; MUFID *et al.*, 2019). It is responsible for performing all the image enhancement processes, feature extraction (AHMED *et al.*, 2021), classification and metrics calculation, which will be discussed in the sections below.

Figure 12 – Sequence of stages involved in the proposed clinical decision-making system.



Source: Elaborated by the author (2022).

Considering the functioning of the platform, the acquisition will be performed from the user uploads that include the breast ultrasound images with either png, jpg, jpeg or gif extensions and channelize them for cloud processing. The images generated after the enhancement process through the enhancement algorithms, as well as their associated metrics, will be stored in a folder for further analysis and possible improvement in the training phases of the presented classification algorithms (MUNADI *et al.*, 2020).

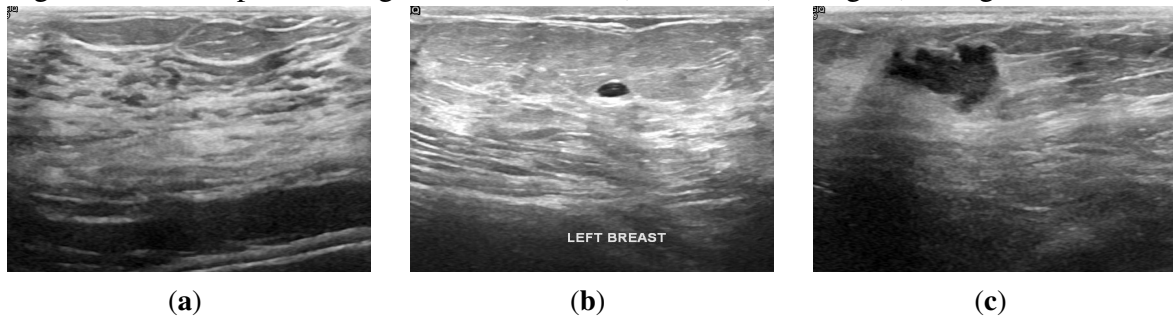
Subsequently followed by the enhancement, the generated images will be processed by the feature extractors and classified as normal, benign or malignant, and the metrics related to these processes will also be recorded in variables in the back end. Once all the results are calculated, the image storage path and the metric values are stored in a JSON file, which will be tracked by the front-end Flask framework, where the user can choose their visualization of interest.

### 3.1 Database Description

The chosen dataset of breast ultrasound images used in this study was proposed in (AL-DHABYANI *et al.*, 2020), which includes data from 600 female patients aged between 25 and 75 years. The dataset comprises a total of 780 gray scale images separated into three classes: normal, containing a total of 133 images; benign, containing 437 images; and, malignant, containing 210 images. The images present in the dataset have an average dimension of  $500 \times 500$  pixels, in PNG format.

Figure 13 shows examples of ultrasound images for each class, normal image, image with benign nodule, and image with nodule and malignant. Table 2 lists the statistics on the count of the number of images in each category considered for the analysis.

Figure 13 – Examples of images of each class. **a)** Normal **b)** Benign **c)** Malignant



Source: Elaborated by the author (2022).

Table 2 – Base data of the images considered for analysis.

Information	Amount	Percent
Normal Images	133	17.05
Benign Images	437	56.03
Malignant Images	210	26.92

Source: Elaborated by the author (2022).



### 3.1.1 Data Augmentation

In order to increase the number of base images, the Data Augmentation technique was used. The transformations used for this analysis were shear, rotation, horizontal translation (x-axis) and vertical translation (y-axis), with their corresponding values in degrees considered for transformation as  $15^\circ$ ,  $15^\circ$ ,  $10^\circ$  and  $10^\circ$ , respectively. For every individual image, the type of transformation used is randomly chosen and they were performed thrice. Thus, the base dataset is augmented with triple the number of images of various transformations, and the corpus of images in the dataset will contain both the original images and the augmented images with applied transformations.

## 3.2 Image Enhancement Techniques

The methods used for image enhancements are categorized into traditional methods and methods based on Deep Learning, as shown below.

### 3.2.1 Bilateral

The two-sided method proposed by (TOMASI; MANDUCHI, 1998), provides a traditional, iterative, local and simple strategy that smoothes images in order to preserve edges, through a non-linear combination of values from nearby images. The bilateral method combines shades of gray or colors based on their geometric proximity and photometric similarity, preferring close values to distant values, both in range and subject, to be within the domain.

The bilateral filter combines domain and range filtering, reinforcing geometric and photometric locality. The combination of domain and range filtering can be seen in the equation 3.1.

$$\mathbf{h}(x) = k^{-1}(x) \int_{-\infty}^{\infty} \int_{-\infty}^{\infty} \mathbf{f}(\xi) c(\xi, x) s(\mathbf{f}(\xi), \mathbf{f}(x)) d\xi \quad (3.1)$$

where,

- $c(\xi, x)$  measures the geometric proximity between the center of the neighborhood  $x$  and a nearby point  $\xi$
- $s(f(\xi), f(x))$  measures the photometric similarity between the pixel at the center of the neighborhood  $x$  and that of a nearby point  $\xi$ .

- The bold font for  $f$  and  $h$  emphasizes the fact that both input and output images can be multiband.

It can be presented with normalization, as in the equation 3.2.

$$k(x) = \int_{-\infty}^{\infty} \int_{-\infty}^{\infty} c(\xi, x) s(f(\xi), f(x)) d\xi \quad (3.2)$$

Thus, the two-sided filter replaces the pixel value in  $x$  with an average of closely similar pixel values. In smooth regions, pixel values in a small neighborhood are similar to each other, and the normalized similarity function  $k^{-1}s$  is close to one. In this way, the two-sided filter acts primarily as a standard domain filter and averages the small, weakly correlated differences between pixel values caused by noise.

### 3.2.2 Histogram Equalization

Histogram Equalization (HE) is another traditional method of image enhancement. Generally, histogram equalization increases the overall contrast of the images, especially when the used image data are represented by close contrast values, thus, it is a non-linear extension of the image, where it redistributes the pixel values and, within of a certain range of grayscale, the number of pixels is almost the same (ZHIHONG; XIAOHONG, 2011).

Considering continuous intensity values, with the variable  $r$  expressing the intensities of an image to be processed, in an interval  $[0, L - 1]$ , with  $r = 0$  being black, and  $r = L - 1$  being the white one. The value of  $L$  is given by  $L = 2^b$ , where  $b$  is the number of bits in the image (GONZALEZ; WOODS, 2018). Thus, one can observe the transformation from the equation 3.3.

$$s_k = T(r_k) = (L - 1) \sum_{j=0}^k p_r(r_j) = \frac{(L - 1)}{MN} \sum_{j=0}^k n_j \quad (3.3)$$

where,  $k = 0, 1, 2, \dots, L - 1$ .

Therefore, the processed image is obtained by mapping each pixel of the input image with intensity  $r_k$  into a corresponding pixel with level  $s_k$  in the output image. The transformation (mapping)  $T(r_k)$  in this equation is called histogram equalization or histogram linearization (GONZALEZ; WOODS, 2018).

### 3.2.3 Total Variance

The Total Variance (TV) method proposed by (CHAMBOLLE, 2004) is treated as another traditional image enhancement method. Here, the authors propose an algorithm for minimization and total variance applications. It is treated as a very fast method and can be used to solve the challenges in noise reduction and zooming, in addition to ensuring better proof of convergence.

For the noise reduction case, we considered recovering the original image  $u$  trying to solve the problem of Equation 3.4, assuming that the observed image  $g = (g_{i,j})_{1 \leq i,j \leq N}$  is the addition of a piecewise smooth (or with little wobble) a priori image  $u = (u_{i,j})_{1 \leq i,j \leq N}$  and a random Gaussian noise, of estimated variance  $\sigma^2$ , where  $N^2$  is the total number of pixels.

$$\min \left\{ J(u) : \|u - g\|^2 = N^2 \sigma^2 \right\} \quad (3.4)$$

Thus, as the purpose of the method is to solve the problem of Equation 3.4, it was assumed that  $N\sigma$  is between 0 and  $\|g - \langle g \rangle\|$ . Thus, we need to find a value  $\bar{\lambda}$  for which  $f(\bar{\lambda}) = N\sigma$ . First, choose an arbitrary initial value  $\lambda_0 > 0$  and calculate  $v_0 = \pi_{\lambda_0 K}(g)$ , that it is a nonlinear projection, as well as  $f(\lambda_0) = \|v_0\|$ . This way, given  $\lambda_n, f_n$   $\lambda_{n+1} = (N\sigma / f_n)\lambda_n$ , calculating  $v_{n+1} = \pi_{\lambda_{n+1} K}(g)$  and  $f_{n+1} = \|v_{n+1}\|$ .

### 3.2.4 Low-Light Image Enhancement via Illumination Map Estimation

The Low-Light Image Enhancement via Illumination Map Estimation (LIME) method is a simple low-light image enhancement method proposed by (GUO *et al.*, 2017). In this method, the illumination of each pixel is initially estimated individually, in order to find the maximum value for each component of the image, the R, G and B. The initial illumination map was refined by imposing a previous structure on it, such as the final lighting map, and thus, with a well-built lighting map, enhancement can be achieved (GUO *et al.*, 2017).

The LIME method is built on the Retinex model, which explains the formation of an image in low light. The model can be observed in the equation 3.5.

$$\mathbf{L} = \mathbf{R} \circ \mathbf{T}, \quad (3.5)$$

where  $L$  and  $R$  are, respectively, the captured image and the desired recovery. The  $\circ$  represents the element-by-element multiplication, while the  $T$  means the lighting map. Thus, they considered that, for color images, the three channels share the same lighting map, using the notation  $\hat{T}$  to represent one-channel and three-channel lighting maps interchangeably.

From this perspective, as a way of estimating the Illumination Map and dealing with non-uniform illumination, they used the equation 3.6:

$$\hat{T}(x) \leftarrow \max_{c \in \{R, G, B\}} L^c \quad (3.6)$$

Thus, it is calculated for each individual pixel  $x$ . The principle underlying the equation 3.6 is that the illumination is at least the maximum value of three channels in a given location. The  $\hat{T}(x)$  obtained guarantees that the recovery will not be saturated, due to the equation

$$R(x) = L(x) / (\max_c L^c(x) + \varepsilon), \quad (3.7)$$

where,  $\varepsilon$  is a constant too small to avoid zero denominator. In view of this, the authors sought with this method to non-uniformly increase the illumination of low-light images, instead of eliminating the color change caused by light sources.

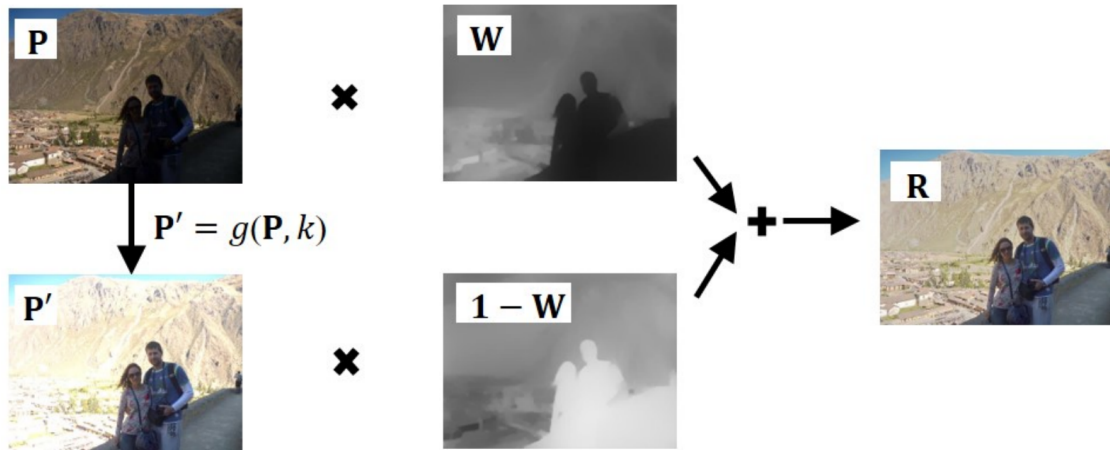
### 3.2.5 Exposure Fusion

In the work by Ying et al., in (YING *et al.*, 2017), the authors developed a new image contrast enhancement algorithm using an exposure fusion framework. This method is used for low-light images, where a weight matrix is designed for image fusion using lighting estimation techniques.

With the model proposed by the authors, the camera response is used to synthesize multiple exposure images and, subsequently, it is used to estimate the best exposure ratio, such that the synthetic image is more exposed in the regions where the input image was underexposed. Thus, the input image and synthetic image are merged according to the weight matrix to achieve the expected enhancement result (YING *et al.*, 2017). Figure 14 shows the steps of the Exposure Fusion method.

To get an image with all pixels well exposed, you can merge the images using Equation 3.8.

Figure 14 – Steps Exposure Fusion.



Source: (YING *et al.*, 2017).

$$R^c = \sum_{i=1}^N W_i \circ P_i^c \quad (3.8)$$

where,  $W_i$  is the weight map of the  $i$ th image,  $P_i$  is the  $i$ th image in the exposure set,  $c$  is the index of three color channels,  $N$  is the number of images and  $R$  is the enhanced result. Thus, poorly exposed pixels receive a small weight, while well exposed pixels receive a large weight.

Thus, in the presented method, the input image itself was merged with another exposure to reduce the complexity, as shown in Figure 14. The fused image is defined as shown in Equation 3.9.

$$R^c = W \circ P^c + (1 - W) \circ g(P^c, k) \quad (3.9)$$

Thus, the enhancement problem can be divided into three parts: the estimate of  $W$ ,  $g$  and  $k$ .

Wherein, the  $W$  is key to achieving an enhancement algorithm that can enhance the low contrast of underexposed regions, while the contrast in well exposed regions is preserved. Thus, the weight matrix is calculated by the equation 3.10:

$$W = T^\mu \quad (3.10)$$

Being the  $T$  the lighting map of the scene and the  $\mu$  is a parameter that controls the degree of enhancement.

The  $g$  deals with the Camera Response Model, in which they proposed a model called Beta-Gamma Correction Model. The brightness transform function (BTF) of the proposed model can be analyzed in the equation 3.11.

$$g(P, k) = \beta P^\gamma = e^{b(1-k^a)} P^{(k^a)} \quad (3.11)$$

Since  $\beta$  and  $\gamma$  are two model parameters that can be calculated from camera parameters  $a$ ,  $b$  and exposure rate  $k$ , where  $a = 0.3293$ ,  $b = 1.1258$ .

The optimal  $k$  is calculated by maximizing the entropy of the highlight brightness image as shown in the equation 3.12.

$$\hat{k} = \underset{k}{\operatorname{argmax}} H(g(B, k)) \quad (3.12)$$

To arrive at this equation, it is necessary to extract the dimly lit pixels as shown in Equation 3.13, measure the brightness component which is defined as the geometric mean of three channels as shown by Equation 3.14, and measure the amount of information, using the image entropy which is defined by Equation 3.15

$$Q = \{P(x) \mid T(x) < 0.5\} \quad (3.13)$$

Where  $Q$  contains only the under-exposed pixels.

$$B := \sqrt[3]{Q_r \circ Q_g \circ Q_b} \quad (3.14)$$

Where,  $Q_r$ ,  $Q_g$  and  $Q_b$  are, respectively, the red, green and blue channels of the input image  $Q$ .

$$H(B) = - \sum_{i=1}^N p_i \cdot \log_2 p_i \quad (3.15)$$

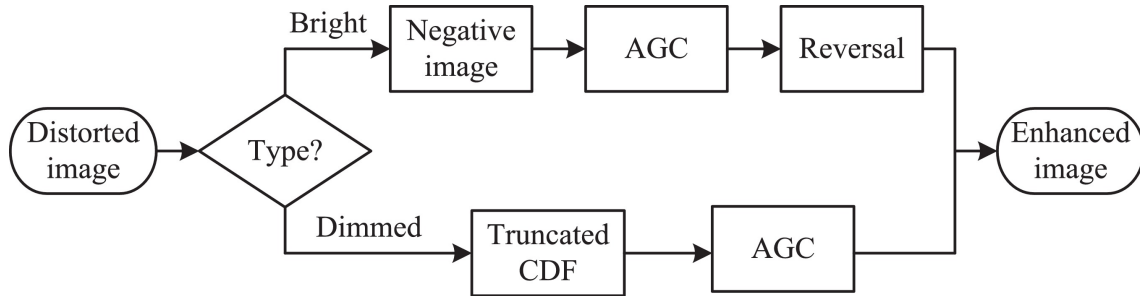
Where,  $p_i$  is the  $i$ th bin of the histogram of  $B$  that counts the number of data evaluated and  $N$  is the number of bins.

### 3.2.6 Gamma Correction

The method proposed by CAO *et al.* (2018) addresses contrast enhancement of glow-distorted images by enhanced adaptive gamma correction. The authors developed an improved adaptive gamma correction technique that utilizes a negative image strategy to perform image contrast of bright images, employing truncated cumulative distribution function modulated gamma correction to enhance the faint ones, thus, distortion in the structure and challenges in local enhancement can be alleviated effectively.

The flowchart of the proposed contrast enhancement method can be seen in Figure 15. The contrast enhancement method is used for two types of images, dim and bright.

Figure 15 – Gamma Correction Flowchart.



Source: Adapted from (CAO *et al.*, 2018).

Thus, first an input image is identified by the threshold of the statistical quantity  $I(x,y), x = 1, 2, \dots, M, y = 1, 2, \dots, N$  as shown in Equation 3.16.

$$t = \frac{m_I - T_t}{T_t} \quad (3.16)$$

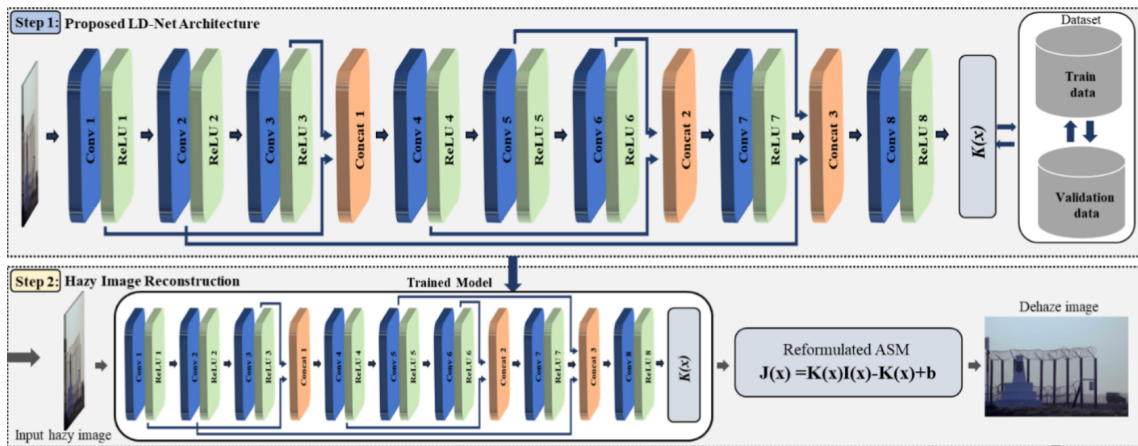
Where,  $m_I = \sum_x \sum_y I(x,y)/MN$  and  $T_t$  is a constant defined as the global average brightness expected for normal natural images. For 8-bit images it is appropriate to use  $T_t$  with approximately half of the maximum pixel intensity, that is, 128. The two cases of input images are those considered dimmed when  $t \leq T_t$  and bright when  $t > T_t$ .

Thus, when the image type is bright, adaptive gamma correction based on the negative image is used, whereas when the image type is dimmed, adaptive gamma correction is used via truncation of the cumulative distribution function, with the aim of to improve contrast as well as restoration.

### 3.2.7 Light-DehazeNet

In the work of ULLAH *et al.* (2021), a new lightweight CNN architecture for image defogging is proposed. The Light-DehazeNet (LD-Net) jointly estimates both the transmission map and atmospheric light using a transformed atmospheric scattering model. In breast ultrasound images with high-density impulse noise, the LD-Net ensures to realize quick and effective means of image denoizing.

Figure 16 – LD-NET architecture.



Source: Adapted from (ULLAH *et al.*, 2021).

LD-Net has eight convolution layers and three concatenation layers, where a rectified linear unit layer follows each convolution layer. The network takes an RGB image of size  $(640 \times 480 \times 3)$  as input, processing in multiple convolution layers with various kernel sizes to extract multiscale features. Different formations of convolutional layers followed by concatenated layers are investigated to retain the useful learned representation.

For image reconstruction, the classic ASM model was transformed into a new representation for the joint estimation of the parameters  $t(x)$ , which is the transmission map, and  $A$ , which is the atmospheric light. Furthermore, to obtain a joint estimate of both model parameters,  $t(x)$  and  $A$  were encapsulated in a new variable called  $k(x)$ , as shown in Equation 3.18.

In this way, the reformulated model with the proposed LD-Net defogging model are encapsulated, in order to directly minimize the reconstruction error. After integrating the two parameters into a single variable  $k(x)$ , the transformed fuzzy image reconstruction formula can be rewritten as Equation 3.17:

$$J(x) = K(x) \times I(x) - K(x) + b_{ias} \quad (3.17)$$



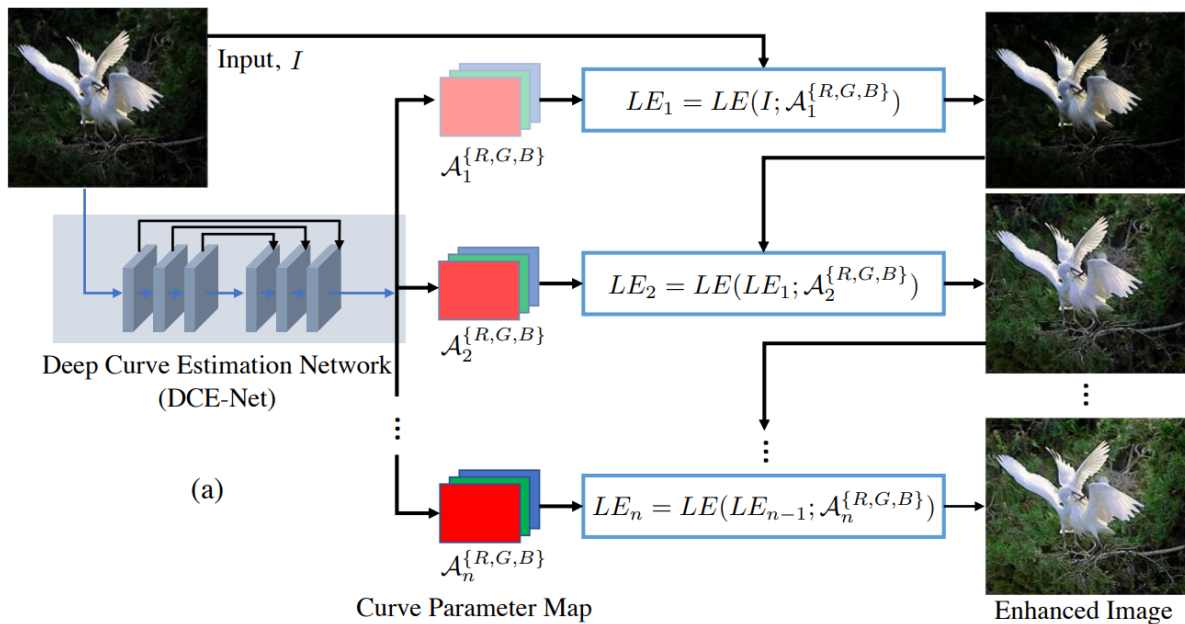
$$K(x) = \frac{\frac{1}{t(x)} \times (I(x) - A) + (A - b_{ias})}{I(x) - 1} \quad (3.18)$$

Thus,  $I(x)$  refers to the observed fuzzy image and  $b_{ias}$  refers to the bias term with a default value of 1, while  $K(x)$  is the new variable containing  $t(x)$  and  $A$ .

### 3.2.8 Zero-Reference Deep Curve Estimation

The paper proposed by (GUO *et al.*, 2020) presents a Zero-Reference Deep Curve Estimation (Zero-DCE) as method that formulates light enhancement strategy as one of the image-specific curve estimation tasks using a deep neural network. It is highly instrumental in pixel-wise and high-order curve estimation and assists in adjusting the dynamic range of the input image. Further, the non-reference loss functions used for implementing the Zero-DCE help to realize an intuitive and simple nonlinear curve mapping.

Figure 17 – Zero-DCE architecture.



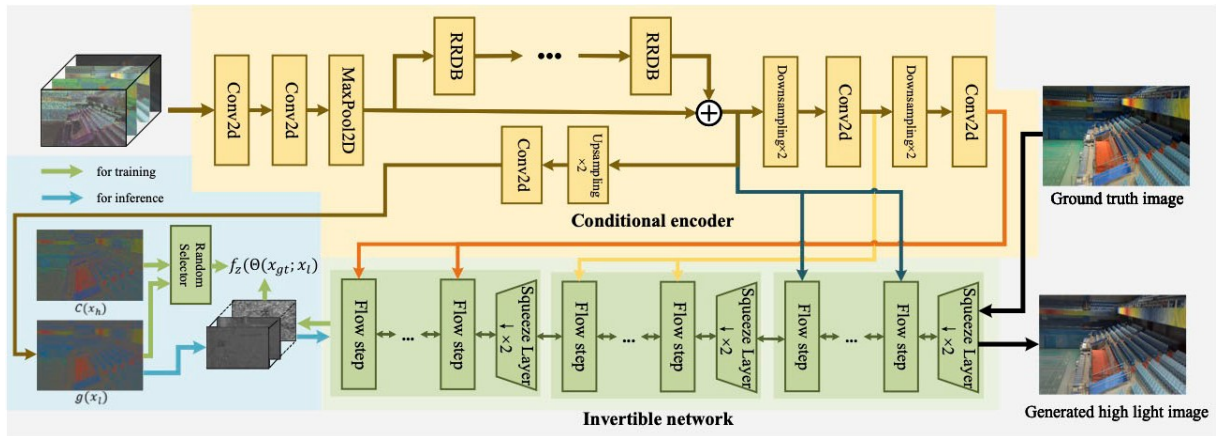
Source: (GUO *et al.*, 2020).

Figure 17 presents the architecture and operation of Zero-DCE. Shows the structure of Zero-DCE. Thus, a DCE-Net is organized to estimate a set of best-fit light enhancement curves, known as Light-Enhancement curves (LE curves), which iteratively enhance a given input image. Each layer of DCE-Net consists of 32 convolutional kernels of size  $3 \times 3$  and step 1 followed by the ReLU activation function.

### 3.2.9 Low-Light Image Enhancement with Normalizing Flow

The research proposed by (WANG *et al.*, 2021) addresses a flow-based low-light image enhancement with a normalizing flow method to accurately learn global image properties as well as local pixel correlations by modeling distributions over images normally exposed. It establishes the mapping relationship of low-light images from one to many by considering the conditional distribution. This Low-Light Image Enhancement with Normalizing Flow (LLFLOW) technique helps to achieve enhanced images with better illumination, rich colors, and less noise, as well as artifacts.

Figure 18 – LLFLOW architecture.



Source: (WANG *et al.*, 2021).

Figure 18 shows the architecture of LLFLOW. The proposed method is an invertible network that learns image distributions, normally exposed in low light conditions, as well as a conditional encoder to extract the color map invariant to illumination. To carry out the training, the variable change theorem was used in order to maximize the exact probability of high light images  $x_h$ . A random selector was also used to obtain the average value of the latent variable  $z$  that obeys the Gaussian distribution of the color map of the reference image or the extracted color map  $g(x_l)$  of the low light image through the conditional encoder.

Passing the training step, to perform the inference, one can randomly select  $z$  among  $N(g(x_l), 1)$  to generate different images of normally exposed images with different levels of brightness from the distribution learned conditional  $f_{flow}(x | x_l)$ .

### 3.3 Data Extraction

CNNs have been widely used for various purposes and applications (MUHAMMAD *et al.*, 2020; KHAN *et al.*, 2019; HUSSAIN *et al.*, 2020; MUHAMMAD *et al.*, 2021). To extract features from the images, we used the Resnet CNN proposed by (HE *et al.*, 2016), which possesses a residual learning structure that facilitates the training of substantially deeper networks. This type of network has greater ease of optimization and can gain accuracy even with considerably greater depth. Several methods have been developed based on Resnet, such as (LIU *et al.*, 2021; YANG *et al.*, 2021; WAN; GU, 2021; WANG *et al.*, 2021), which were observed to eliminate noise inference in the images, and assist in identifying even complex features with better accuracy.

In terms of the Resnet architecture, the vast majority of convolutional layers have  $3 \times 3$  filters and follow two basic rules. Firstly, the layers have the same number of filters for the same output feature map size. Secondly, the number of filters is doubled if the feature map size is reduced by half, to preserve per-layer time complexity. Subsequently, the downsampling is performed directly by convolutional layers. It possesses a global averaging pool layer and a 1000-way fully connected layer with softmax, with a total of 34 weighted layers (HE *et al.*, 2016).

### 3.4 Classification Methods

For this study, the fully connected layer of the network was eliminated and only the core Resnet50 was used for performing the feature extraction. Subsequently, to classify the data extracted by Resnet50, the Multi-Layer Perceptron (MLP), Support Vector Machine (SVM) and k-Nearest Neighbor (k-NN) classifiers were used.

#### 3.4.1 Multi-Layer Perceptron (MLP)

MLP is a supervised learning technique that consists of an artificial neural network based on forward-feeding biological neurons that has three types of layers, the input layer to collect the input data, the output layer that gives the decision over the input data, and the hidden layer, which lies between the input layer and the output layer (DUTTA; CHANDA, 2021; AHIL *et al.*, 2021).

At least one hidden layer is added to the MLP, and there can be numerous hidden

layers. With the exception of the input layer, each node is a neuron with a nonlinear activation function (WANG; WANG, 2021).

### 3.4.2 Support Vector Machine (SVM)

The SVM is based on the statistical learning theory (LIU *et al.*, 2019). SVM is a supervised machine learning technique that builds a set of hyperplanes in a high-dimensional space, and good separation of the hyperplanes is achieved when it is obtained based on the greatest distance to the closest training data point of any class (KR *et al.*, 2019).

### 3.4.3 k-Nearest Neighbor (k-NN)

The k-NN is a supervised machine learning regression and classification technique (TURESSON *et al.*, 2016). The idea of kNN is that the point  $k$  closest to the sample to be tested is usually found through the Euclidean distance (SALIM *et al.*, 2020). If most of the  $k$  points belong to the same category as the sampled, this sample will be classified in the same class (MA *et al.*, 2022).

## 3.5 Statistical Metrics

The metrics used for analysis were both to evaluate the quality of the images, as well as to evaluate the classification accuracy.

### 3.5.1 Quality Metrics

The quality of the assessment process was ensured through several aspects that can be observed through the following metrics:

- RMSE: The Root Mean Square Error (RMSE) is a metric that considers the root mean squared error between two sets of data. In this metric, the closer to zero, the more accurate the observed forecast results (SABILLA *et al.*, 2021). Thus, a comparison will be made with the two breast ultrasound images, the original and the image after applying the improvement algorithms.

$$RMSE = \sqrt{\frac{\sum_{i=1}^n (P_i - O_i)^2}{n}}, \quad (3.19)$$

where,  $P_i$  is the actual value of the data,  $O_i$  is the predicted value,  $n$  is the number of data and  $\sum$  is the total number of values.

- CNR: The Contrast-to-Noise Ratio (CNR) is a metric to measure the contrast of images. It enables us to analyze the difference in contrast between the nodules and the other regions in the breast ultrasound images (RODRIGUEZ-MOLARES *et al.*, 2018).

$$\text{CNR} = \frac{|\mu_i - \mu_o|}{\sqrt{\sigma_i^2 + \sigma_o^2}}, \quad (3.20)$$

where,

$$\sigma_i = E\{(\|s_i\|^2 - \mu_i)^2\}, \quad (3.21)$$

$$\sigma_o = E\{(\|s_o\|^2 - \mu_o)^2\}, \quad (3.22)$$

which are the variation of signal strength inside and outside the target area, respectively, and  $E$  is the expected value operator.

- AMBE: The Absolute Mean Brightness Error (AMBE) is a metric that evaluates the difference between the average intensity level of the enhanced ultrasound image and the average intensity level of the original image (HARUN *et al.*, 2020).

$$\text{AMBE} = |I(y) - I(x)| \quad (3.23)$$

where  $I(y)$  is the average intensity level of the enhanced image and  $I(x)$  is the average intensity level of the original image.

- AG: The Average Gradient (AG) is a metric that represents the clarity of the breast ultrasound image, reflecting the image's ability to express contrast details between the nodule and the other regions (ABDALRAHMAN *et al.*, 2021).

$$\text{AG} = \frac{1}{M \times N} \sum_{i=1}^M \sum_{j=1}^N \sqrt{\frac{(\frac{\partial f}{\partial x})^2 + (\frac{\partial f}{\partial y})^2}{2}} \quad (3.24)$$

where  $M$  and  $N$  are the width and height of the image,  $(\frac{\partial f}{\partial x})$  and  $(\frac{\partial f}{\partial y})$  refers to the horizontal and vertical gradients.

- PSNR: The Peak Signal-to-Noise Ratio (PSNR) is a metric that evaluates the relationship between the maximum value of the measured signal and the amount of noise that affects the signal of breast ultrasound images (SABILLA *et al.*, 2021).

$$PSNR = 20 \log_{10} \left( \frac{MAX_f}{\sqrt{MSE}} \right) \quad (3.25)$$

where  $MAX_f$  is the maximum value and  $\sqrt{MSE}$  is the result of the RMSE.

- SSIM: The Structural Similarity Index Measure (SSIM) is one of the quality assessment metric used to measure the visual changes and similarity between two images, by performing quality assessment and comparing the structural characteristics, which is described through the structural similarities (SABILLA *et al.*, 2021). In this way, it helps to analyze the similarity between the original breast ultrasound image and the image after applying the image improvement algorithm.

$$SSIM(x, y) = \frac{(2\mu_x\mu_y + c_1)(2\sigma_{xy} + c_2)}{(\mu_x^2 + \mu_y^2 + c_1)(\sigma_x^2 + \sigma_y^2 + c_2)} \quad (3.26)$$

where, with an image  $I(x, y)$  and  $\mu_x$  being the average value for  $x$  or luminance  $x$ ,  $\mu_y$  being the average value for  $y$  or luminance  $y$ ,  $\sigma_y$  the contrast value for  $y$ ,  $\sigma_x$  the contrast value for  $x$ ,  $c_1$  and  $c_2$  being two variables used to stabilize the division if the divisor is 0.

### 3.5.2 Rank Metrics

The classification of clinical data presents a few challenges, among them, two of which are primary ones to be addressed. The first is the unbalanced dataset, where a greater number of cases have negative diagnoses than positive diagnoses. In the second one, the main interest is to accurately classify the positive case of the disease, since false positives do not cause great damage while false negatives can result in a delay in treatment, consequently increasing the difficulty of an early diagnosis.

The classification of clinical data presents a few challenges, among them, two of which are primary ones to be addressed. The first is the unbalanced dataset, where there is a greater number of cases with one diagnosis than the other. In the second one, the main interest is to accurately classify the positive case of the disease, since false positives do not cause great harm, while false negatives can result in a delay in treatment, consequently increasing the difficulty of an early diagnosis.

To measure the accuracy of the method, the confusion matrix is used as a basis, using the evaluation metrics of True Positive (TP), False Positive (FP), True Negative (TN) and False Negative (FN).

As this search has three classes, benign, malignant and normal, the confusion matrix can be described as shown in Figure 19.

Figure 19 – The confusion matrix highlighting the performance accuracy of the classification of mammogram images, with the diagonal elements in bold representing the true prediction labels.

		Predicted Class		
		Benign	Malignant	Normal
True Class	Benign	<b>TB</b>	$FN_{BM}$	$FN_{BN}$
	Malignant	$FP_{MB}$	<b>TM</b>	$FN_{MN}$
	Normal	$FP_{NB}$	$FP_{NM}$	<b>TN</b>

Source: Elaborated by the author (2022).

In this way, we have:

- True Positive class Benign (TB): TB occurs when in the actual dataset, class Benign was correctly predicted as class Benign.
- True Positive Malignant class (TM): The TM occurs when in the actual dataset, the Malignant class was correctly predicted as the Malignant class.
- True Positive Normal class (TN): The TN occurs when in the actual dataset, the Normal class was correctly predicted as the Normal class.
- False Negative (FN): The FN occurs when in the actual data set, the class we are trying to predict was predicted incorrectly. That is, when it was supposed to be cancer and was diagnosed as non-cancer. Within false negatives cases, it is possible to distinguish three types:  $FN_{BM}$ , when the case was benign and was misclassified as malignant;  $FN_{BN}$ , when the case was benign and was misclassified as normal; and  $FN_{MN}$ , when the case was

malignant and was misclassified as normal.

- False Positive (FP): The FP occurs when in the actual dataset, the class we are trying to predict was predicted incorrectly. That is, when it was supposed to be non-cancer and was diagnosed as cancer. Within false positive cases, it is possible to distinguish three types:  $FP_{MB}$ , when the case was malignant and was incorrectly classified as benign;  $FP_{NB}$ , when the case was normal and was incorrectly classified as benign; and  $FP_{NM}$ , when the case was normal and was incorrectly classified as malignant.

For this, five metrics were used to evaluate the results considering these questions, namely: Accuracy (AccGlobal), F1-score (F1score), benign class hit rate (Benign), malignant class hit rate (Malignant), and normal class hit rate (Normal).

- Accuracy: This is the general probability of success, which shows the global success rate considering the analyzed classes. Thus, it takes into account the hits of the three classes under all hits and misses.

$$AccGlobal = \frac{TB + TM + TN}{TB + TM + TN + FN + FP} \quad (3.27)$$

- F1-score: It is the harmonic average between precision and recall. It is a commonly used metric to assess unbalanced data.

$$F1score = 2 \times \frac{Precision \times Recall}{Precision + Recall} \quad (3.28)$$

- Hit rate of benign class (Benign): This is the probability that a patient who has a positive diagnosis for benign actually has a benign nodule.

$$Benign = \frac{TB}{TB + FN_{BM} + FN_{BN}} \quad (3.29)$$

- Hit rate of Malignant class: This is the probability that a patient who has a positive diagnosis for malignant actually has a malignant nodule.

$$Malignant = \frac{TM}{TM + FP_{MB} + FN_{MN}} \quad (3.30)$$

- Hit rate of the Normal class (Normal): This is the probability that a patient who has a negative diagnosis for nodules actually does not have nodules.

$$Normal = \frac{TN}{TN + FP_{NB} + FP_{NM}} \quad (3.31)$$



### 3.6 Experimental Configuration

Initially, a Resnet50 (a CNN with 50 layers deep neural network) was implemented as a feature extractor, learning intrinsic patterns from images to identify breast cancer. For classification, the algorithms MLP, SVM and kNN were used. The dataset extracted by Resnet50 was divided into training data using k-fold Cross Validation with 20 fields. Hyperparameters were optimized through grid search. Relative to kNN, the number of neighbors  $\in [3, 10]$  and leaf size  $\in [10, 50]$ . The SVM parameters, the  $\gamma \in [2^{-15}, 2^{-1}]$  and  $C \in [2^{-5}, 2^5]$ . As for MLP, the parameters were the number of hidden layers  $\in [1, 5]$ , the number of neurons per hidden layer  $\in [50, 500]$ ,  $\alpha \in [0.000001, 1]$ , and learning rate  $\in [0.000001, 0.9999]$ .

The experiments were performed on a computing terminal with Windows 11 Operating System (a new version from Microsoft Corporation), i7 11800H processor, 8-core, 24Mb Cache, 4.6GHz, 11th generation, 16Gb of DDR4 RAM, 3200 MHz, and NVIDIA Geforce RTX 3060 video card (a Graphical Processing Unit from NVIDIA Corporation), 6GB GDDR6.

## 4 RESULTS AND DISCUSSION

In this section, the results obtained for the improvement of the images, as well as for classification, will be discussed.

### 4.1 Image Enhancement

With the application of the enhancement algorithms on the ultrasound images, the processing duration of each approach was summarized as shown in Table 3. It is evident from the statistics that the Bilateral and LIME algorithms consume much longer processing time compared to the other algorithms, particularly the Bilateral with 1344 min. The Gamma correction method was the one that consumes the shortest processing time of 2.8 min.

Table 3 – Comparison of processing time taken by image enhancement algorithms (in minutes).

Algorithms	Processing Time (Minutes)
Bilateral	1344.5736
Gamma correction	2.8820
HE	7.1598
LDNet	6.7305
LIME	651.8196
LLFLOW	9.2683
TV	17.3219
Ying	8.8536
ZDCE	9.5254

Source: Elaborated by the author (2022).

From the perspective of the processing times of the algorithms, the metrics presented in Table 4 is used to assess the quality of the obtained images. It can be seen that in relation to the RMSE metric and the AMBE metric, the algorithm that obtained the best results was the TV with 0.0227 and 0.0017, respectively. The bilateral algorithm achieved a result close to the TV, with RMSE of 0.0329 and AMBE of 0.0063. The HEP and LIME algorithms achieved inferior results both in the RMSE metric and in the AMBE metric among the other algorithms.

Regarding the CNR metric, the algorithms that had the highest contrast–noise ratio were the HE and LIME methods, while the lowest contrast–noise ratio were the TV and Bilateral methods.

Analyzing the AG metric, which evaluates the change in the intensity of pixel values, it can be seen that the smallest change was for the Bilateral and LIME methods, both with 0.0,

Table 4 – Quality metrics for image enhancement algorithms.

Algorithms	RMSE	CNR	AMBE	AG	PSNR	SSIM
Bilateral	0.0329	0.0317	0.0063	0.0	77.8054	0.8726
Gamma correction	0.0936	0.4060	0.0763	0.0363	36.7292	0.8924
HE	0.2391	0.9998	0.2161	0.0364	61.2157	0.6347
LDNet	0.2360	0.9508	0.1941	0.0361	60.7778	0.3705
LIME	0.2801	0.9982	0.2272	0.0	59.4688	0.3778
LLFLOW	0.1342	0.5578	0.1069	0.0184	66.3159	0.8116
TV	0.0227	0.0088	0.0017	3.86e-05	81.0792	0.8569
Ying	0.0691	0.3125	0.0621	0.1676	71.6003	0.9394
ZDCE	0.1334	0.6059	0.1189	0.0362	65.6991	0.7858

Source: Elaborated by the author (2022).

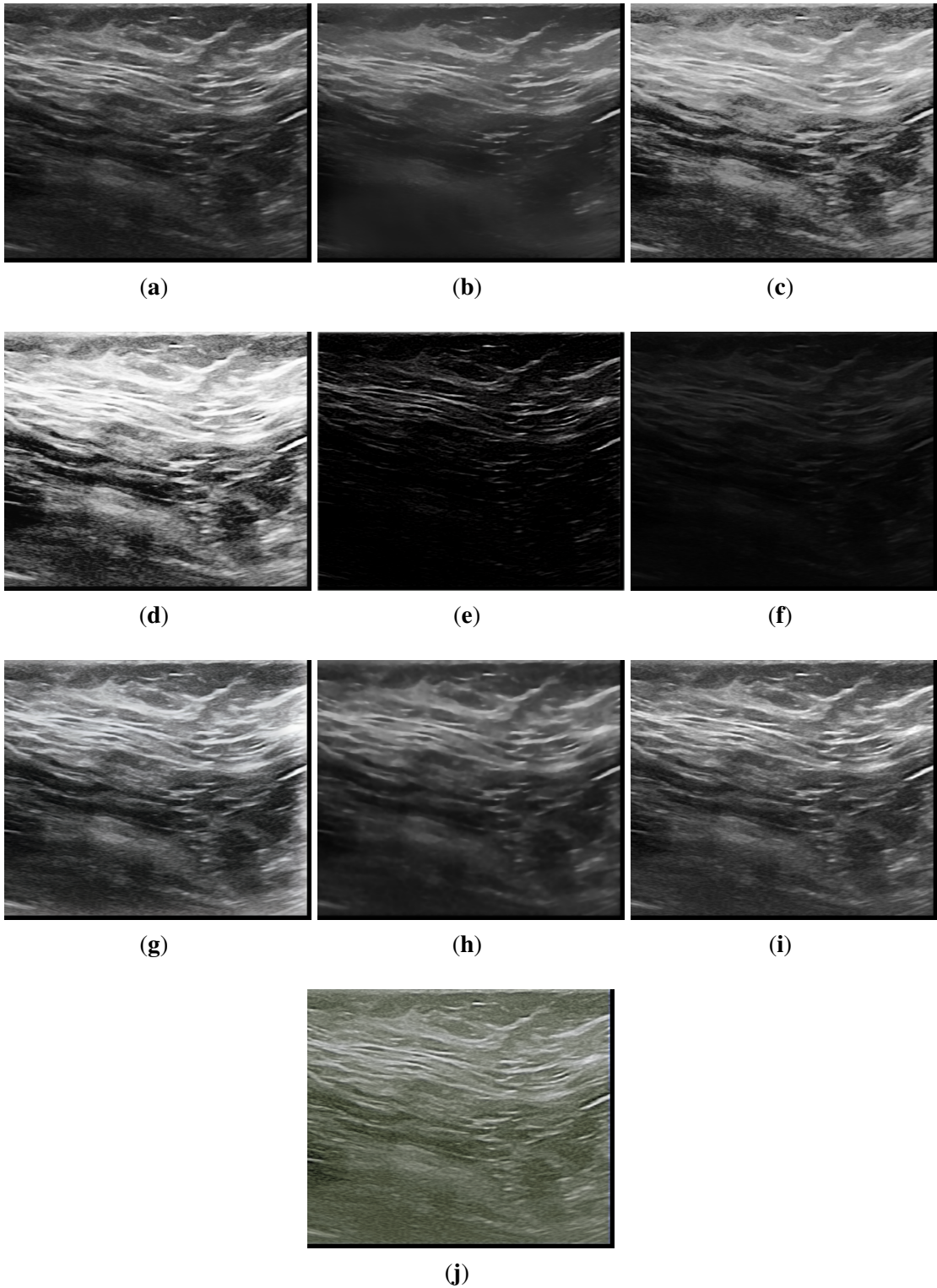
while the Ying method was the one that caused the greatest change in intensity. When analyzed from the perspective of the PSNR metric, the TV method achieved the best result with 81.0792, followed by the Bilateral method with 77.8054. The Gamma algorithm achieved the worst result compared to the others, with 36.7292.

With the conception of the SSIM metric, the Ying algorithm achieves the closest result to the original image with 0.9394, while LDNet being the most distant method with 0.3705, followed by LIME with 0.3778. The Gamma, Bilateral, TV and LLFLOW methods achieved the SSIM value above 0.80.

Considering all the metrics, the TV method achieved a good performance in three of the seven analyzed metrics. The Bilateral method achieved the best result in the AG metric and also achieved good results in the RMSE, AMBE and PSNR metrics.

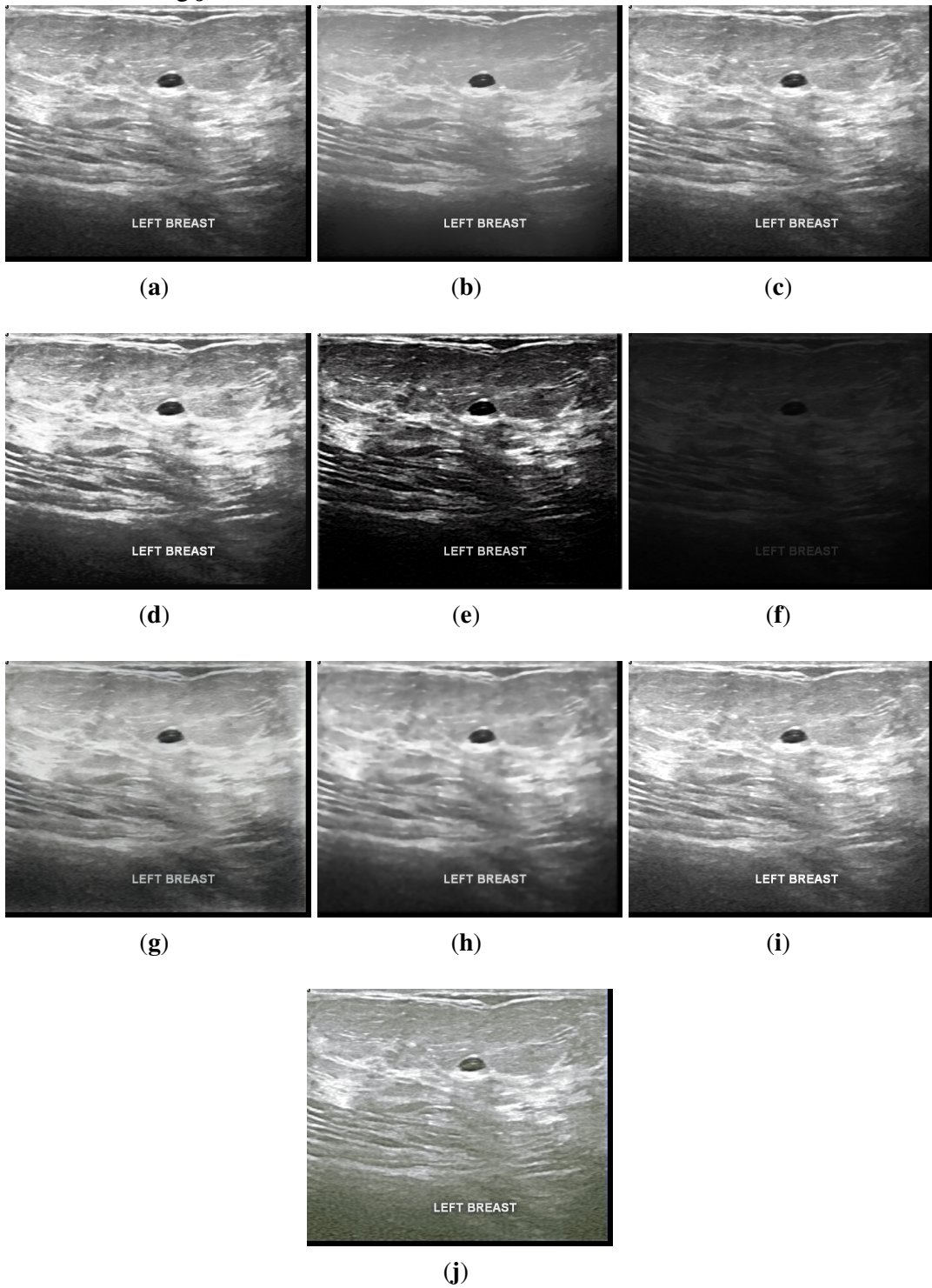
With the application of image enhancement algorithms, it can be seen in Figures 20–22 the elimination of some noise that presents the same characteristics of the region of interest. It is noted that the TV and Bilateral algorithms, which presented better results in quality metrics, have images with less noise compared to the other algorithms, which can facilitate better classification accuracy.

Figure 20 – Normal highlighted mammogram images **a)** Original **b)** Bilateral **c)** Gamma correction **d)** HE **e)** LDNET **f)** LIME **g)** LLFLOW **h)** TV **i)** Ying **j)** Zero-DCE.



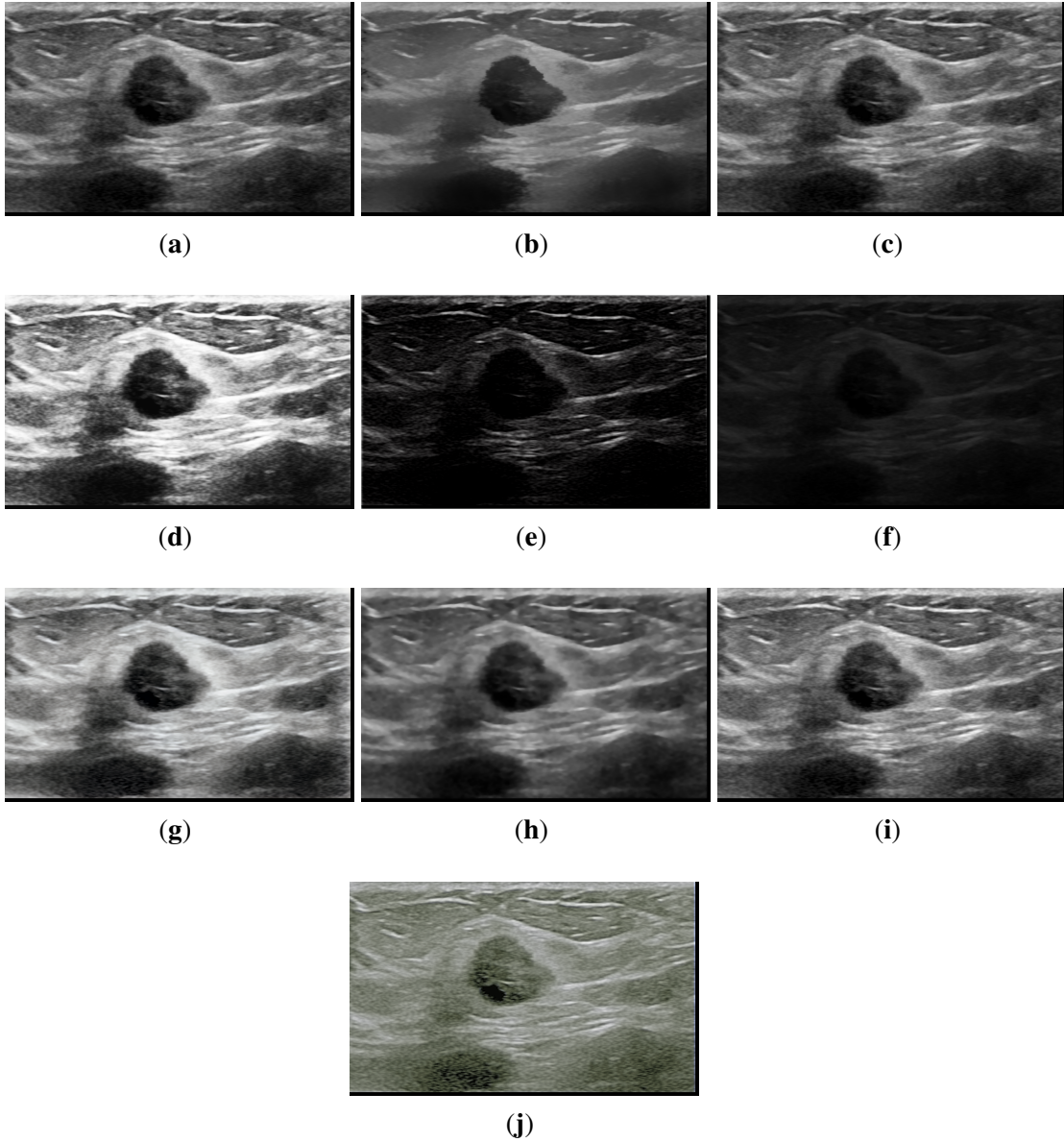
Source: Elaborated by the author (2022).

Figure 21 – Benign highlighted mammogram images **a)** Original **b)** Bilateral **c)** Gamma correction **d)** HE **e)** LDNET **f)** LIME **g)** LLFLOW **h)** TV **i)** Ying **j)** Zero-DCE.



Source: Elaborated by the author (2022).

Figure 22 – Malignant highlighted mammogram images **a)** Original **b)** Bilateral **c)** Gamma correction **d)** HE **e)** LDNET **f)** LIME **g)** LLFLOW **h)** TV **i)** Ying **j)** Zero-DCE.



Source: Elaborated by the author (2022).

## 4.2 Classification

From the data extracted with Resnet50, the results were obtained using the MLP, kNN and SVM algorithms for the metrics of global accuracy (ACC Global), benign success rate (Benign), malignant success rate (Malignant), hit rate of normals (Normal) and F1-score. Furthermore, presented in Table 5 are the training and testing times for each algorithms for image enhancement, considering the MLP, kNN and SVM classifiers.

It is worth noting that the kNN classifier provides the shortest training time in relation to the other algorithms. Further, the combination of the HE enhancement approach with the kNN achieved the shortest training time. The MLP classifier, despite being the one that takes more training time, in relation achieves the shortest test times. Moreover, it is observed that the TV method in association with the MLP achieved the shortest test time.

Table 5 – Training and testing times of image enhancement algorithms and the classifiers.

Algorithms	Times (Seconds)	MLP	kNN	SVM
Original	Training	161.605	0.105	109.754
	Test	0.036	1.119	5.582
Bilateral	Training	165.828	0.107	114.538
	Test	0.034	1.105	5.741
Gamma correction	Training	142.177	0.106	113.221
	Test	0.039	1.231	5.801
HE	Training	164.593	0.104	117.841
	Test	0.033	1.176	5.906
LDNET	Training	197.522	0.106	119.007
	Test	0.040	1.143	6.101
LIME	Training	158.675	0.105	110.196
	Test	0.032	1.193	5.622
LLFLOW	Training	120.524	0.106	114.953
	Test	0.032	1.205	5.803
TV	Training	141.409	0.106	115.173
	Test	0.031	1.214	5.900
Ying	Training	156.628	0.105	115.086
	Test	0.033	1.194	5.874
Z-DCE	Training	169.422	0.105	123.348
	Test	0.037	1.122	6.170

Source: Elaborated by the author (2022).

In Table 6 are presented the metrics for each image enhancement algorithm, as well as for the original base. Analyzing the enhancement algorithms for each classifier individually,

we observe that for the MLP classifier, the algorithm that obtained the best accuracy result was the TV algorithm with 95.64%, being considered statistically similar to the Bilateral method that reached an accuracy rate of 95.54%.

For the kNN classifier, the algorithm that obtained the best results in terms of both accuracies and hit rate of images with malignant nodules (malignant) was LDNET with 83.23% and 76.90%, respectively. For the SVM classifier, the algorithm that obtained the best global accuracy was the Bilateral one with 96.69%. The TV algorithm delivers an accuracy rate of 96.66%, by considering the Wilcoxon method, which is statistically equal to the Bilateral method.

Analyzing in general, considering the best combination between the image improvement algorithm and classifier, the one that delivers the better results with balanced trade-offs was the Bilateral algorithm in association with the SVM classifier, both quantitatively and qualitatively assessed through visual analysis of the presented images.

Although global accuracy is a valid metric, the accuracy rate in the classification of images with malignant nodules (malignant) is fundamental for this analysis, as it is more clinically relevant. Thus, it can be seen that the Bilateral algorithm with the SVM classifier for the malignant metric achieved the best result among all combinations, with 95.11%.

Taking into account the training and testing times along with their the hit metrics, it is clear that despite the kNN training time being the shortest, it was the algorithm that delivers the inferior results for all image enhancement methods. The SVM that achieved neither the shortest, nor the longest training and test times assists in providing better classification accuracy.

Figures 23, 24 and 25 show the Boxplot graphs for the SVM, kNN and MLP classifiers for the Global ACC metric of each image enhancement algorithm. The variability of the improvement methods among the classifiers can be seen, showing statistical information such as, for example, median, minimum and maximum.

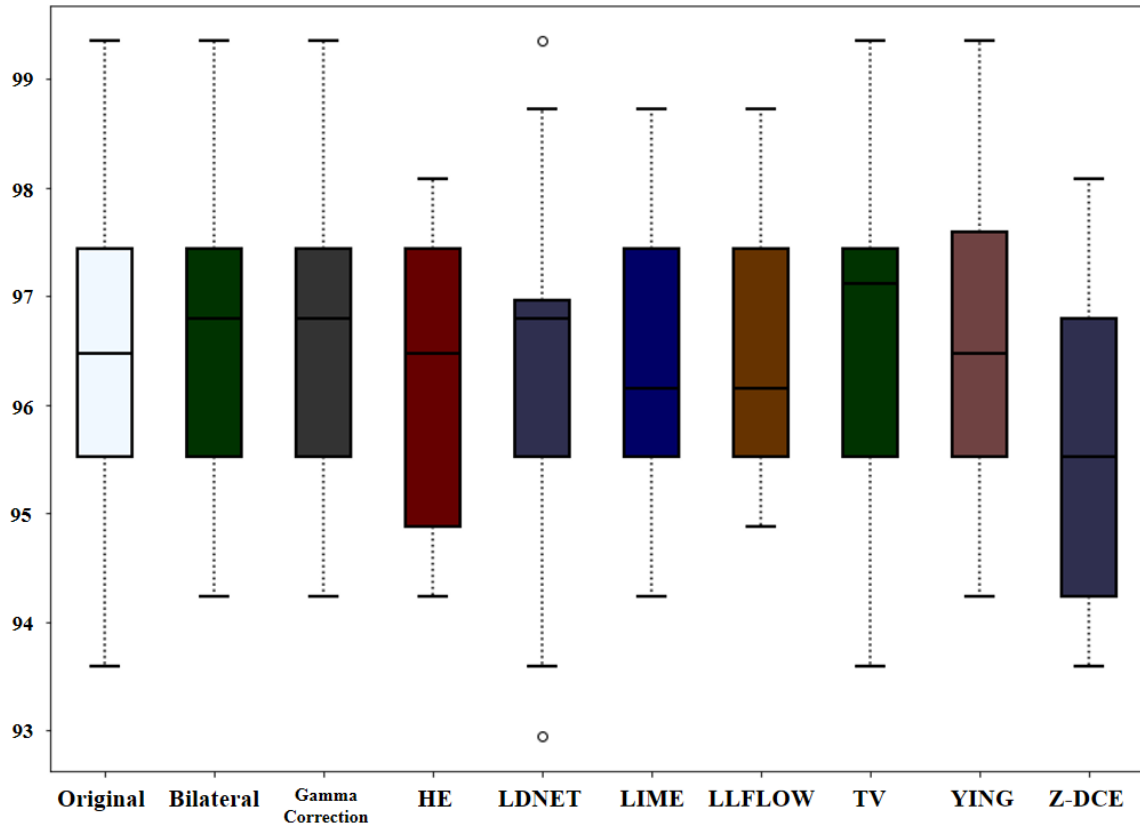
It can be seen that the results for the SVM classifier have the best statistical data compared to the other classifiers. The maximum and median values are higher, as well as the minimum values are lower when compared to kNN and MLP.

Considering only the best combination that was targeted for achieving the best result of global and malignant accuracy, Figure 26 shows the confusion matrix for the combination of the bilateral method with the SVM classifier.

It is evident from the analysis that the benign class had 1701 correctly classified, while the malignant and normal had 799 and 517, respectively. The benign class possesses more



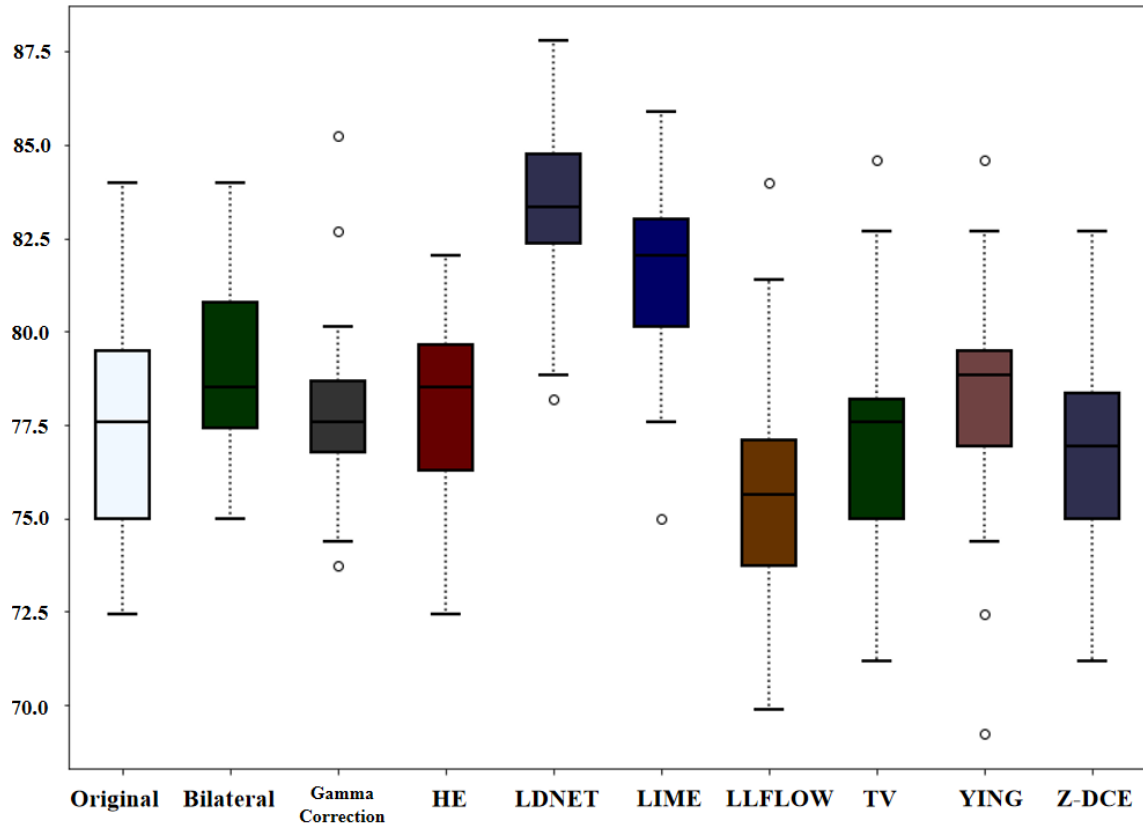
Figure 23 – Global Accuracy: SVM Classifier Performance as Seen in Boxplot.



Source: Elaborated by the author (2023).

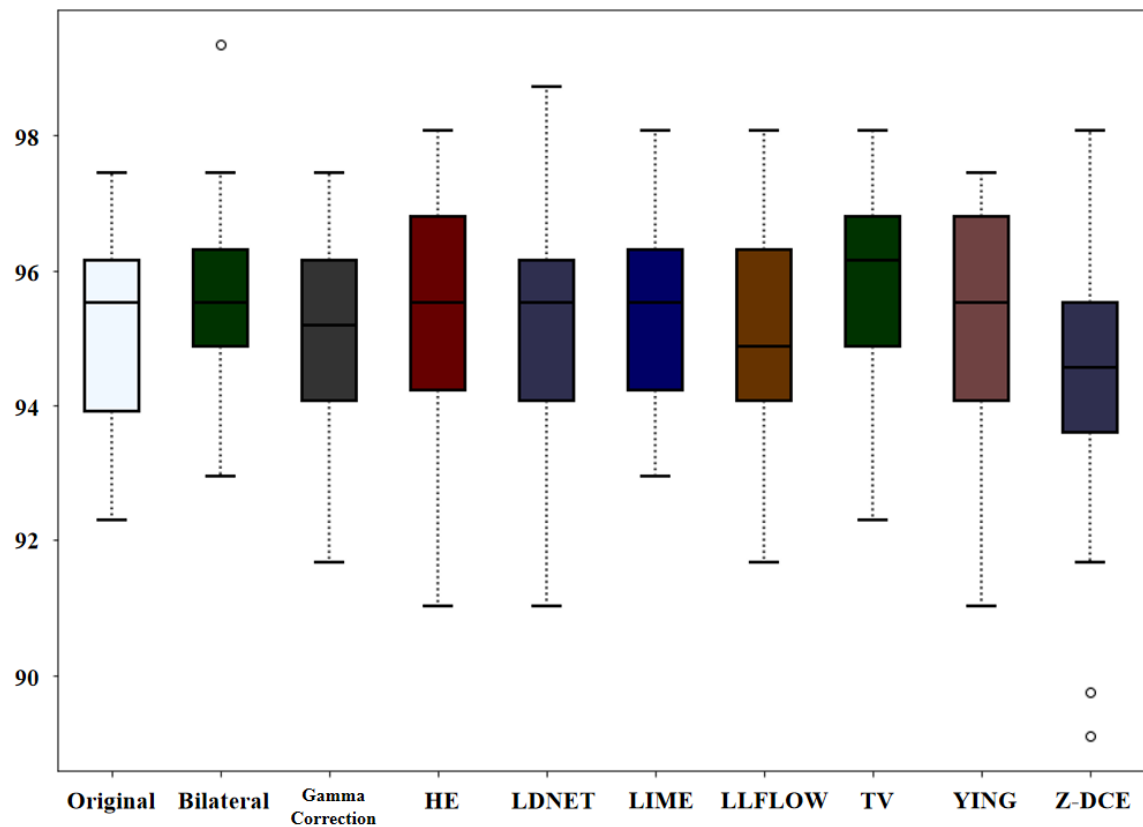
errors than the malignant class, as these two classes contain nodules in their images. A similar situation occurred with the malignant class as well, as there were more errors in the benign class. In the normal class, there are more errors than in the benign class, which could also be observed in comparison with the normal class, which comes very close to the error of the malignant class that has the nodule.

Figure 24 – Global Accuracy: k-NN Classifier Performance as Seen in Boxplot.



Source: Elaborated by the author (2023).

Figure 25 – Global Accuracy: MLP Classifier Performance as Seen in Boxplot.



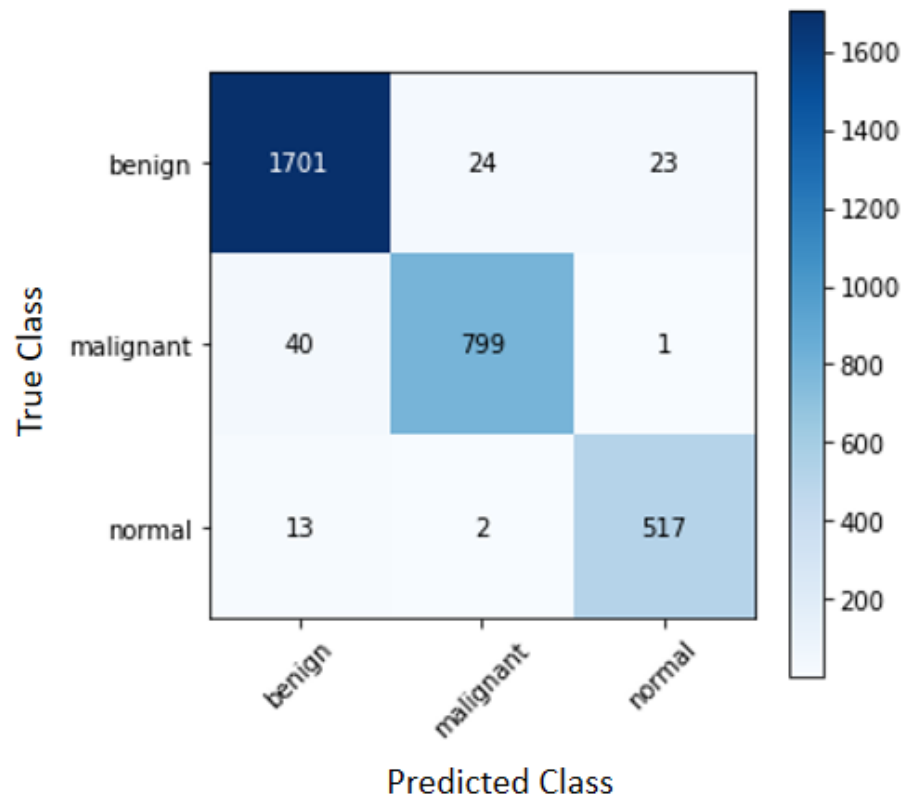
Source: Elaborated by the author (2023).

Table 6 – Metrics for image enhancement algorithms.

Algorithms	Metrics	MLP	kNN	SVM
Original	ACC Global	94.99 ± 1.65	77.85 ± 3.30	96.50 ± 1.82
	Benign	97.08 ± 1.50	76.44 ± 4.98	97.42 ± 1.44
	Malignant	92.50 ± 3.21	71.90 ± 5.90	94.40 ± 2.94
	Normal	92.15 ± 7.50	91.91 ± 5.87	96.80 ± 3.99
	F1-score	94.96 ± 1.69	78.57 ± 3.20	96.49 ± 1.56
Bilateral	ACC Global	95.54 ± 1.36	79.07 ± 2.45	<b>96.69 ± 1.56</b>
	Benign	96.68 ± 1.91	78.78 ± 3.06	97.31 ± 1.94
	Malignant	92.61 ± 3.44	73.21 ± 5.92	95.11 ± 2.86
	Normal	96.41 ± 4.41	89.31 ± 5.65	97.18 ± 3.54
	F1-score	95.53 ± 1.37	79.70 ± 2.41	96.69 ± 1.56
Gamma correction	ACC Global	94.93 ± 1.59	77.91 ± 2.66	96.47 ± 1.33
	Benign	96.74 ± 1.57	77.17 ± 4.08	97.54 ± 1.31
	Malignant	91.90 ± 3.86	70.83 ± 5.52	93.92 ± 3.32
	Normal	93.83 ± 5.90	91.54 ± 6.45	97.00 ± 3.66
	F1-score	94.91 ± 1.61	78.72 ± 2.65	96.46 ± 1.35
HE	ACC Global	95.28 ± 1.71	78.07 ± 2.62	96.31 ± 1.38
	Benign	96.45 ± 2.01	78.20 ± 4.21	97.25 ± 1.50
	Malignant	92.97 ± 3.87	75.23 ± 5.80	94.40 ± 2.84
	Normal	95.15 ± 4.55	82.15 ± 7.88	96.26 ± 3.51
	F1-score	95.27 ± 1.71	78.45 ± 2.54	96.30 ± 1.39
LDNET	ACC Global	94.96 ± 1.96	83.23 ± 2.54	96.31 ± 1.52
	Benign	96.90 ± 1.81	84.61 ± 3.07	97.19 ± 1.59
	Malignant	93.09 ± 4.63	76.90 ± 5.48	94.40 ± 3.55
	Normal	91.50 ± 7.48	88.73 ± 6.95	96.45 ± 4.60
	F1-score	94.93 ± 1.99	83.44 ± 2.46	96.30 ± 1.53
LIME	ACC Global	95.51 ± 1.46	81.57 ± 2.57	96.47 ± 1.24
	Benign	96.91 ± 1.72	82.21 ± 3.45	97.25 ± 1.36
	Malignant	92.38 ± 3.49	75.00 ± 5.90	94.16 ± 3.14
	Normal	95.88 ± 3.71	89.87 ± 6.47	97.56 ± 2.45
	F1-score	95.50 ± 1.46	82.00 ± 2.55	96.46 ± 1.24
LLFLOW	ACC Global	95.06 ± 1.66	75.96 ± 3.40	96.34 ± 1.07
	Benign	96.23 ± 2.25	75.74 ± 3.73	97.25 ± 1.32
	Malignant	92.49 ± 3.47	68.09 ± 6.79	93.69 ± 2.94
	Normal	95.34 ± 6.82	89.10 ± 6.33	97.57 ± 3.77
	F1-score	95.04 ± 1.66	76.75 ± 3.25	96.33 ± 1.07
TV	ACC Global	95.64 ± 1.41	77.33 ± 3.21	<b>96.66 ± 1.66</b>
	Benign	96.97 ± 1.57	73.97 ± 5.25	97.42 ± 1.57
	Malignant	93.09 ± 3.18	76.30 ± 5.02	94.88 ± 2.84
	Normal	95.31 ± 4.38	90.05 ± 5.44	97.00 ± 3.86
	F1-score	95.63 ± 1.42	78.08 ± 3.06	96.66 ± 1.67
Ying	ACC Global	95.22 ± 1.56	78.14 ± 3.35	96.57 ± 1.39
	Benign	96.22 ± 1.76	76.90 ± 5.01	97.37 ± 1.44
	Malignant	93.80 ± 3.94	73.21 ± 7.25	94.64 ± 3.18
	Normal	94.18 ± 6.42	90.02 ± 5.97	96.99 ± 3.69
	F1-score	95.21 ± 1.58	78.93 ± 3.16	96.56 ± 1.39
Z-DCE	ACC Global	94.23 ± 2.18	76.89 ± 2.96	95.80 ± 1.35
	Benign	96.68 ± 1.56	78.56 ± 5.18	97.14 ± 1.46
	Malignant	92.14 ± 4.06	69.40 ± 5.54	93.09 ± 2.90
	Normal	89.52 ± 9.41	83.31 ± 7.36	95.70 ± 3.74
	F1-score	94.17 ± 2.25	77.25 ± 2.94	95.79 ± 1.35

Source: Elaborated by the author (2022).

Figure 26 – Confusion matrix for the combination of the Bilateral algorithm with the SVM classifier.



Source: Elaborated by the author (2022).

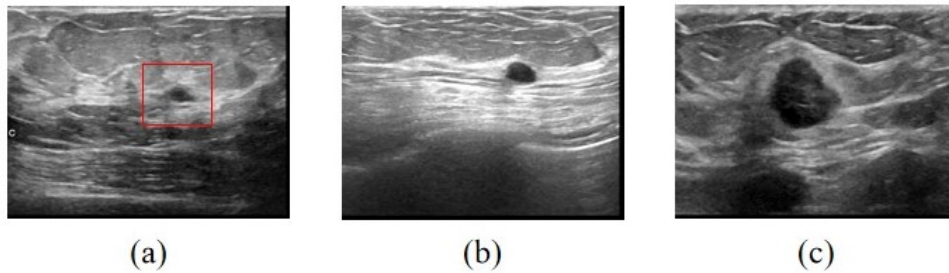
One of the possible explanations is that, although normal images do not have nodules, there are still regions in the ultrasound image that may have similarities with nodules. The characteristics of benign nodules are that they are well-defined and regular, whereas malignant nodules are larger and asymmetrical in shape. Thus, it may be observed that some of the regions in the normal images resemble the nodules in the benign images.

In Figure 27, it is possible to verify in (a) that the region marked in red has a similarity with the benign nodule, even though it has a lighter texture. In Figures 27 (b),(c), one can see the shapes of both benign and malignant nodules through their visual differences.

Analyzing the complete confusion matrix, it is noted that there were only 48 false negatives and 55 false positives. These false negatives and false positives are the ones that can cause the most inconvenience and delays in medical treatments and diagnoses, so minimizing these false positives is of great importance.

Thus, observing Table 4, which presents the image quality metrics, and Table 6, which presents the classification metrics, it is clear that the algorithms that obtained better results in the metrics of quality were the ones that achieved the best results in the ranking metrics. The

Figure 27 – Database images. (a) Normal image with region marked in red that resembles a benign nodule. (b) Image with a benign nodule. (c) Image with malignant nodule.



Source: Elaborated by the author (2022).

TV method and the Bilateral method stood out in terms of the quality metrics and achieved reasonable rates in the classification.

More stability and consistency in the results of the proposed image enhancement techniques were proved with better precision in the earlier stage detection of breast cancers. Particularly, the novel approaches in the pre-processing stages of the breast ultrasound image using different image enhancement algorithms guarantees stabilized outcomes on the chosen dataset. Therefore, it can be verified that good pre-processing, making improvements in the images, can considerably benefit the classification results.

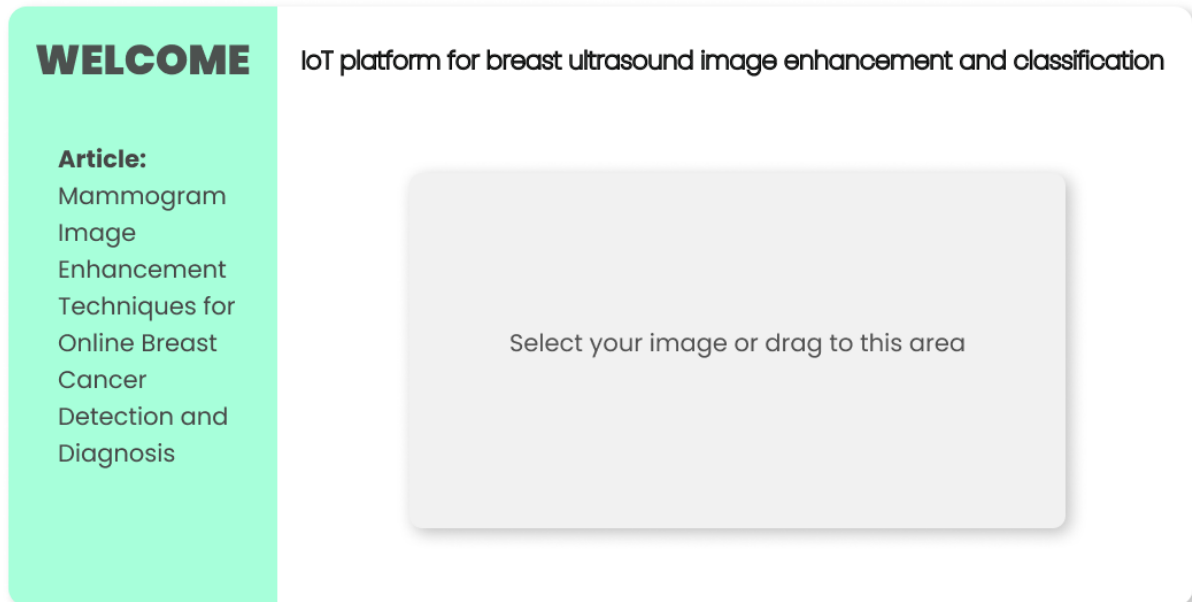
### 4.3 Online System/Web Interfaces

The online platform for automatic pre-screening of breast tumors basically consists of four modules: the main interface, the interface with enhanced images, the classification interface when there are nodules and the classification interface when there are no nodules, as specified in Figure 28. All image enhancement algorithms were tested and presented in the enhanced image interface. However, for classification purposes, the Bilateral and SVM set was selected.

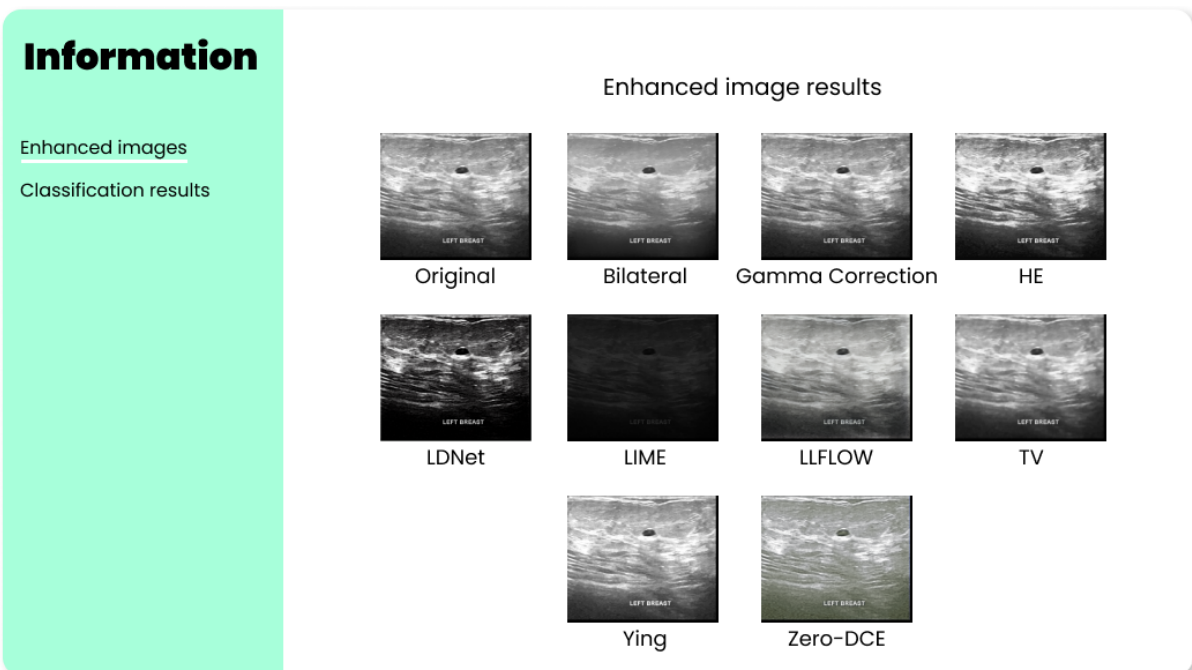
Figure 28a shows the main interface module, where it will be possible to upload the breast tumor images to be analyzed. After uploading, the web portal redirects users to the second interface. This module presents a menu-driven interface with the users, which will be capable of analyzing the pre-processed images by the image enhancement methods, as well as the classification result. When clicking on the “Enhanced images” button in the menu, the users will be redirected to the interface containing the specified image with the application of image enhancement methods, as shown in Figure 28b.

By clicking on “Classification results” in the menu, the users will be presented with a message. If there is a nodule, a message will be displayed to consult a mastologist (as shown in Figure 28c), if there is no nodule, the user will be informed that no nodule was found in the image (as shown in Figure 28d).

Figure 28 – Online web platform interfaces modules. (a) Main interface module (b) Module with images enhancement (c) Classification module with nodules (d) Nodule-free sorting module.



(a)



(b)

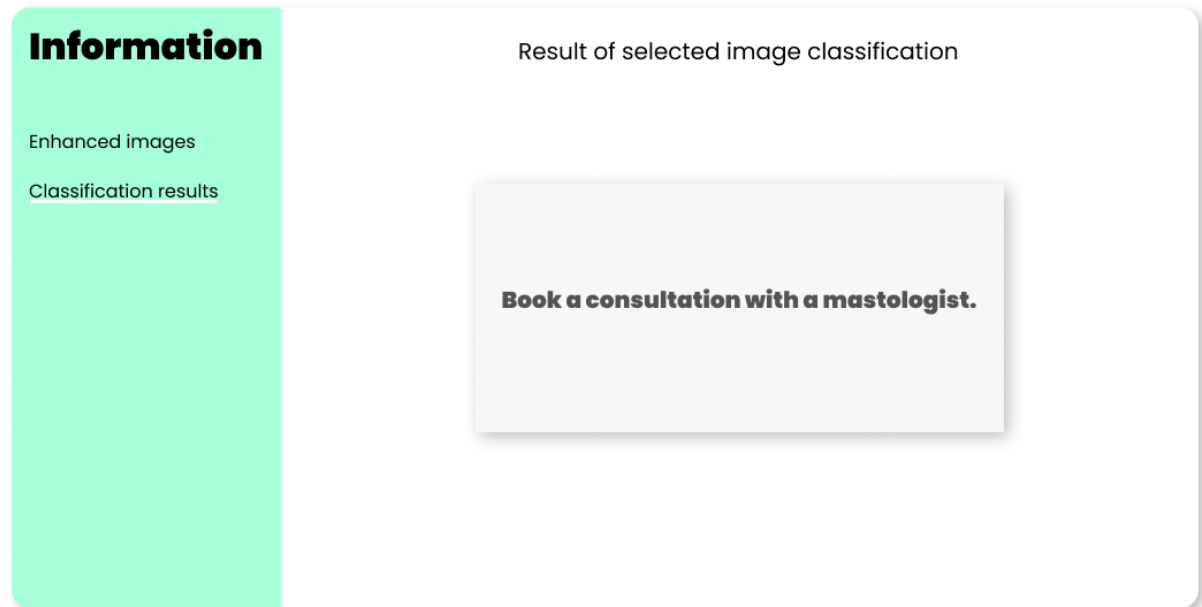
*Cont.*

**Information**

Enhanced images  
Classification results

Result of selected image classification

**Book a consultation with a mastologist.**

A screenshot of a user interface. On the left, there is a light green vertical bar containing the word 'Information' in bold, and two lines of text: 'Enhanced images' and 'Classification results'. To the right of this bar, the text 'Result of selected image classification' is centered. Below this text is a light gray rectangular box with a drop shadow, containing the bold text 'Book a consultation with a mastologist.'

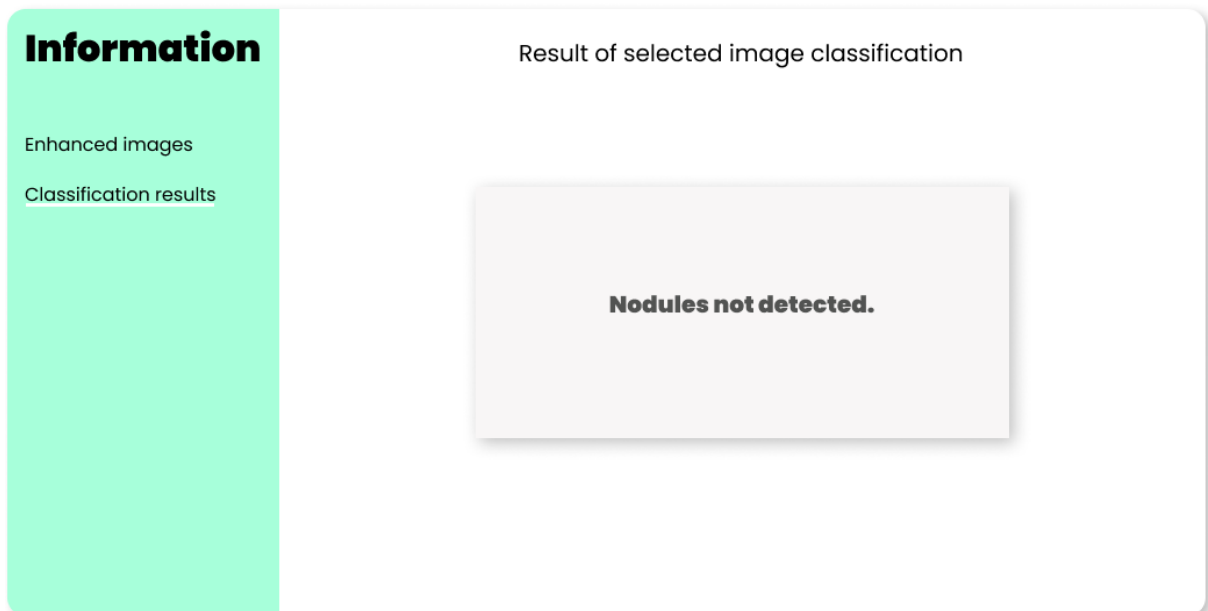
(c)

**Information**

Enhanced images  
Classification results

Result of selected image classification

**Nodules not detected.**

A screenshot of a user interface, similar to the one above. It features a light green vertical bar on the left with 'Information' in bold, and 'Enhanced images' and 'Classification results' below it. To the right, the text 'Result of selected image classification' is centered. Below this is a light gray rectangular box with a drop shadow, containing the bold text 'Nodules not detected.'

(d)

Source: Elaborated by the author (2022).



## 5 CONCLUSIONS AND FUTURE WORK

This research proposed to compare and evaluate methods for enhancing breast ultrasound images and classifying them as benign, malignant, and normal. For this purpose, a database containing 437 benign images, 210 malignant images and 133 normal images were used. Due to the small number of images, various data augmentation techniques were used. To extract the characteristics of these images, Resnet50 was used. For these extracted data, the SVM, kNN and MLP algorithms were used to perform the classification.

It was found through the experimental results that the application of appropriate image enhancement methods can improve classification performance. In addition, the algorithms that obtained better results in the metrics for achieving better image quality provided the best results in the classification.

It is observed that the Bilateral enhancement method together with the SVM classification algorithm obtained the highest hit rate, both for global accuracy (96.69%) and for accuracy in the detection of malignant tumors (95.11%). In addition, the TV method also achieved satisfactory results, with a processing time lower than that of the Bilateral method and similar performance results. Therefore, it is noted that the application of image enhancement methods has significant relevance to the diagnosis of breast cancer.

In this context, the following future works are intended to open up better opportunities for the researchers:

- Developing novel light image enhancement strategies specific for breast cancer, considering the applied generic enhancement algorithms;
- Embedding such new enhancement approaches in specific hardware modules with the possibility of interacting with the cloud;
- Building 3D reconstruction models to perform the volumetric quantification of the nodules;
- Building a web dashboard to analyze the experiments as well as the 3D reconstruction with better visualizations.

## REFERENCES

- ABDALRAHMAN, A.; ISMAIL, S. M.; SAID, L. A.; RADWAN, A. G. Double fractional-order masks image enhancement. *In: 3rd NOVEL INTELLIGENT AND LEADING EMERGING SCIENCES CONFERENCE (NILES)*. 2021, FL, USA: **International Institute of Informatics and Systemics**, 2021. p. 261–264.
- ABIN, D.; D.THEPADE, S.; DHORE, S. An empirical study of dehazing techniques for chest x-ray in early detection of pneumonia. *In: 2nd INTERNATIONAL CONFERENCE FOR EMERGING TECHNOLOGY (INCET)*. 2021, Belagavi, India: **Proceedings**, 2021. p. 1–5.
- ACS, A. C. S. **About breast cancer**. [s. n.], 2021. Available at: <<https://www.cancer.org/cancer/breast-cancer/about/what-is-breast-cancer.html>>. Accessed on: 10 jan. 2023.
- AFAQ, S.; JAIN, A. Mammo-net: An approach for classification of breast cancer using cnn with gabor filter in mammographic images. *In: INTERNATIONAL CONFERENCE ON COMPUTATIONAL INTELLIGENCE AND SUSTAINABLE ENGINEERING SOLUTIONS (CISES)*. 2022, Greater Noida, India: **Proceedings**, 2022. p. 177–182.
- AFONSO, L. C.; ROSA, G. H.; PEREIRA, C. R.; WEBER, S. A.; HOOK, C.; ALBUQUERQUE, V. H. C.; PAPA, J. P. A recurrence plot-based approach for parkinson’s disease identification. **Future Generation Computer Systems**, [S.l.], v. 94, p. 282–292, 2019. ISSN 0167-739X. Available at: <<https://www.sciencedirect.com/science/article/pii/S0167739X18322507>>. Accessed on: 02 jan. 2023.
- AGRAWAL, A.; XU, Y.; RASKAR, R. Invertible motion blur in video. *In: ACM SIGGRAPH 2009 papers*. [S.l.: s.n.], 2009. p. 1–8.
- AHIL, M. N.; VANITHA, V.; RAJATHI, N. Apple and grape leaf disease classification using mlp and cnn. *In: 2021 INTERNATIONAL CONFERENCE ON ADVANCEMENTS IN ELECTRICAL, ELECTRONICS, COMMUNICATION, COMPUTING AND AUTOMATION (ICAECA)*. 2021, Coimbatore, India: **Proceedings**, 2021. p. 1–4.
- AHMED, I.; AHMAD, A.; JEON, G. An iot-based deep learning framework for early assessment of covid-19. **IEEE Internet of Things Journal**, [S.l.], v. 8, n. 21, p. 15855–15862, 2021.
- AHMED, M.; ISLAM, M. R. Breast cancer classification from histopathological images using convolutional neural network. *In: 2021 INTERNATIONAL CONFERENCE ON COMPUTER, COMMUNICATION, CHEMICAL, MATERIALS AND ELECTRONIC ENGINEERING (IC4ME2)*. 2021, Rajshahi, Bangladesh: **Proceedings**, 2021. p. 1–4.
- AL-DHABYANI, W.; GOMAA, M.; KHALED, H.; FAHMY, A. Dataset of breast ultrasound images. **Data in Brief**, v. 28, p. 104863, 2020. ISSN 2352-3409. Available at: <<https://www.sciencedirect.com/science/article/pii/S2352340919312181>>. Accessed on: 20 oct. 2022.
- BABU, A.; JEROME, S. A. Mammogram image grade gauging of denoising filters enhancement methods. *In: 2022 FIRST INTERNATIONAL CONFERENCE ON ELECTRICAL, ELECTRONICS, INFORMATION AND COMMUNICATION TECHNOLOGIES (ICEEICT)*. 2022, Trichy, India: **Proceedings**, 2022. p. 1–6.

- BADAWY, S. M.; MOHAMED, A. E.-N. A.; HEFNAWY, A. A.; ZIDAN, H. E.; GADALLAH, M. T.; EL-BANBY, G. M. Classification of breast ultrasound images based on convolutional neural networks - a comparative study. *In: 2021 INTERNATIONAL TELECOMMUNICATIONS CONFERENCE (ITC-EGYPT)*. 2021, Alexandria, Egypt: **Proceedings**, 2021. p. 1–8.
- BAI, Y.; JIA, H.; JIANG, M.; LIU, X.; XIE, X.; GAO, W. Single-image blind deblurring using multi-scale latent structure prior. **IEEE Transactions on Circuits and Systems for Video Technology**, [S.l.], v. 30, n. 7, p. 2033–2045, 2020.
- BUDA, M.; SAHA, A.; WALSH, R.; GHATE, S.; LI, N.; ŚWIĘCICKI, A.; LO, J. Y.; MAZUROWSKI, M. A. Detection of masses and architectural distortions in digital breast tomosynthesis: a publicly available dataset of 5,060 patients and a deep learning model. **arXiv preprint arXiv:2011.07995**, 2020. Available at: <<https://arxiv.org/abs/2011.07995>>. Accessed on: 10 sep. 2022.
- CAO, G.; HUANG, L.; TIAN, H.; HUANG, X.; WANG, Y.; ZHI, R. Contrast enhancement of brightness-distorted images by improved adaptive gamma correction. **Computers Electrical Engineering**, [S.l.], v. 66, p. 569–582, 2018. ISSN 0045-7906. Available at: <<https://www.sciencedirect.com/science/article/pii/S0045790616306292>>. Accessed on: 02 Oct. 2022.
- CAO, L.; WANG, W.; HUANG, C.; XU, Z.; WANG, H.; JIA, J.; CHEN, S.; DONG, Y.; FAN, C.; ALBUQUERQUE, V. H. C. de. An effective fusing approach by combining connectivity network pattern and temporal-spatial analysis for eeg-based bci rehabilitation. **IEEE Transactions on Neural Systems and Rehabilitation Engineering**, [S.l.], v. 30, p. 2264–2274, 2022.
- CHAMBOLLE, A. An algorithm for total variation minimization and applications. **Journal of Mathematical imaging and vision**, [S.l.], v. 20, n. 1, p. 89–97, 2004.
- CHEN, C.; WANG, Y.; NIU, J.; LIU, X.; LI, Q.; GONG, X. Domain knowledge powered deep learning for breast cancer diagnosis based on contrast-enhanced ultrasound videos. **IEEE Transactions on Medical Imaging**, [S.l.], v. 40, n. 9, p. 2439–2451, 2021.
- CHEN, J.; ZHENG, Y.; LIANG, Y.; ZHAN, Z.; JIANG, M.; ZHANG, X.; DANIEL, S. d. S.; WU, W.; ALBUQUERQUE, V. H. C. d. Edge2analysis: A novel aiot platform for atrial fibrillation recognition and detection. **IEEE Journal of Biomedical and Health Informatics**, [S.l.], p. 1–1, 2022.
- CHENG, X.; FENG, X.; LI, W. Research on feature extraction method of fundus image based on deep learning. *In: IEEE 3rd INTERNATIONAL CONFERENCE ON AUTOMATION, ELECTRONICS AND ELECTRICAL ENGINEERING (AUTEEE)*. 2020, Shenyang, China: **Proceedings**, 2020. p. 443–447.
- CHENG, Y.; LI, B. Image segmentation technology and its application in digital image processing. *In: 2021 IEEE ASIA-PACIFIC CONFERENCE ON IMAGE PROCESSING, ELECTRONICS AND COMPUTERS (IPEC)*. 2021, Dalian, China: **Proceedings**, 2021. p. 1174–1177.
- CHOI, L. **Breast Cancer**. [s. n.], 2022. Available at: <<https://www.msmanuals.com/professional/gynecology-and-obstetrics/breast-disorders/breast-cancer>>. Accessed on: 10 jan. 2023.

- CHU, X.; CHEN, L.; CHEN, C.; LU, X. Improving image restoration by revisiting global information aggregation. *In: COMPUTER VISION–ECCV 2022: 17th EUROPEAN CONFERENCE*. 2022, Tel Aviv, Israel: **Proceedings, Part VII**, 2022. p. 53–71.
- CORONEL, L.; BADOY, W.; NAMOCO, C. Identification of an efficient filtering-segmentation technique for automated counting of fish fingerlings. **Int. Arab J. Inf. Technol.**, [S.l.], v. 15, n. 4, p. 708–714, 2018.
- DABASS, J.; ARORA, S.; VIG, R.; HANMANDLU, M. Segmentation techniques for breast cancer imaging modalities-a review. *In: 9th INTERNATIONAL CONFERENCE ON CLOUD COMPUTING, DATA SCIENCE ENGINEERING (CONFLUENCE)*. 2019, Noida, India: **Proceedings**, 2019. p. 658–663.
- DULF, E.-H.; MURESAN, C. I.; MOCAN, T.; MOCAN, L. Computer-aided diagnosis system for colorectal cancer. *In: 25th INTERNATIONAL CONFERENCE ON SYSTEM THEORY, CONTROL AND COMPUTING (ICSTCC)*. 2021, Iasi, Romania: **Proceedings**, 2021. p. 178–181.
- DUTTA, J.; CHANDA, D. Music emotion recognition in assamese songs using mfcc features and mlp classifier. *In: 2021 INTERNATIONAL CONFERENCE ON INTELLIGENT TECHNOLOGIES (CONIT)*. 2021, Hubli, India: **Proceedings**, 2021. p. 1–5.
- FACCIO, T. A. d. **Análise de características em imagens digitais na tarefa de segmentação interativa** 2020. 81 f. Master's Thesis (Mestrado Matemática Aplicada e Computacional) — Faculdade de Ciências e Tecnologia de Presidente Prudente, Programa de Pós-Graduação em Matemática Aplicada e Computacional, Universidade Estadual Paulista, Presidente Prudente, 2020.
- GAO, Z.; WANG, X.; SUN, S.; WU, D.; BAI, J.; YIN, Y.; LIU, X.; ZHANG, H.; de Albuquerque, V. H. C. Learning physical properties in complex visual scenes: An intelligent machine for perceiving blood flow dynamics from static ct angiography imaging. **Neural Networks**, [S.l.], v. 123, p. 82–93, 2020. ISSN 0893-6080. Available at: <<https://www.sciencedirect.com/science/article/pii/S0893608019303764>>. Accessed on: 02 sep. 2022.
- GONÇALVES, J. C. **Reconhecimento de dígitos em imagens de medidores de consumo de gás natural utilizando técnicas de visão computacional** 2016. 119 f. Master's Thesis (Mestrado Computação Aplicada) — Universidade Tecnológica Federal do Paraná, Curitiba, 2016.
- GONG, G.; ZHANG, K. Local blurred natural image restoration based on self-reference deblurring generative adversarial networks. *In: 2019 IEEE INTERNATIONAL CONFERENCE ON SIGNAL AND IMAGE PROCESSING APPLICATIONS (ICSIPA)*. 2019, Kuala Lumpur, Malaysia: **Proceedings**, 2019. p. 231–235.
- GONZALEZ, R.; WOODS, R. **Processamento de Imagens Digitais**. 1. ed. [S.l.]: Blucher, 2000.
- GONZALEZ, R.; WOODS, R. **Digital Image Processing**. 3. ed. [S.l.]: Pearson, 2010.
- GONZALEZ, R.; WOODS, R. **Digital Image Processing**. 4. ed. [S.l.]: Pearson, 2018.

GUO, C.; LI, C.; GUO, J.; LOY, C. C.; HOU, J.; KWONG, S.; CONG, R. Zero-reference deep curve estimation for low-light image enhancement. *In: 2020 IEEE/CVF CONFERENCE ON COMPUTER VISION AND PATTERN RECOGNITION (CVPR)*. 2020, Seattle, USA: **Proceedings**, 2020. p. 1777–1786.

GUO, X.; LI, Y.; LING, H. Lime: Low-light image enhancement via illumination map estimation. **IEEE Transactions on Image Processing**, [S.l.], v. 26, n. 2, p. 982–993, 2017.

HARRON, N. A.; OSMAN, N. F.; SULAIMAN, S. N.; KARIM, N. K. A.; ISMAIL, A. P.; SOH, Z. H. C. An image denoising model using deep learning for digital breast tomosynthesis images. *In: 2022 IEEE 13TH CONTROL AND SYSTEM GRADUATE RESEARCH COLLOQUIUM (ICSGRC)*. 2022, Shah Alam, Malaysia: **Proceedings**, 2022. p. 177–182.

HARUN, N. H.; BAKAR, J. A.; WAHAB, Z. A.; OSMAN, M. K.; HARUN, H. Color image enhancement of acute leukemia cells in blood microscopic image for leukemia detection sample. *In: 2020 IEEE 10th SYMPOSIUM ON COMPUTER APPLICATIONS INDUSTRIAL ELECTRONICS (ISCAIE)*. 2020, Malaysia: **Proceedings**, 2020. p. 24–29.

HE, K.; ZHANG, X.; REN, S.; SUN, J. Deep residual learning for image recognition. *In: 2016 IEEE CONFERENCE ON COMPUTER VISION AND PATTERN RECOGNITION (CVPR)*. 2016, Las Vegas, USA: **Proceedings**, 2016. p. 770–778.

HOSSAIN, M. M.; HASAN, M. M.; RAHIM, M. A.; RAHMAN, M. M.; YOUSUF, M. A.; AL-ASHHAB, S.; AKHDAR, H. F.; ALYAMI, S. A.; AZAD, A.; MONI, M. A. Particle swarm optimized fuzzy cnn with quantitative feature fusion for ultrasound image quality identification. **IEEE Journal of Translational Engineering in Health and Medicine**, [S.l.], v. 10, p. 1–12, 2022.

HUANG, C.; SONG, P.; GONG, P.; TRZASKO, J. D.; MANDUCA, A.; CHEN, S. Debiasing-based noise suppression for ultrafast ultrasound microvessel imaging. **IEEE Transactions on Ultrasonics, Ferroelectrics, and Frequency Control**, [S.l.], v. 66, n. 8, p. 1281–1291, 2019.

HUANG, C.; ZHANG, G.; CHEN, S.; ALBUQUERQUE, V. H. C. de. An intelligent multisampling tensor model for oral cancer classification. **IEEE Transactions on Industrial Informatics**, v. 18, n. 11, p. 7853–7861, 2022.

HUSSAIN, T.; MUHAMMAD, K.; ULLAH, A.; CAO, Z.; BAIK, S. W.; ALBUQUERQUE, V. H. C. de. Cloud-assisted multiview video summarization using cnn and bidirectional lstm. **IEEE Transactions on Industrial Informatics**, [S.l.], v. 16, n. 1, p. 77–86, 2020.

INCA, I. N. de Câncer José Alencar Gomes da S. **Atualização em mamografia para técnicos em radiologia**. [s. n.], 2019. Available at: <[https://bvsmis.saude.gov.br/bvsmis/publicacoes/atualizacao\\_mamografia\\_tecnicos\\_radiologia\\_2ed\\_rev\\_atal.pdf](https://bvsmis.saude.gov.br/bvsmis/publicacoes/atualizacao_mamografia_tecnicos_radiologia_2ed_rev_atal.pdf)>. Accessed on: 12 jan. 2023.

INCA, I. N. de Câncer José Alencar Gomes da S. **Estimativa 2020: incidência de câncer no Brasil**. [s. n.], 2019. Available at: <<https://www.inca.gov.br/sites/ufu.sti.inca.local/files//media/document//estimativa-2020-incidencia-de-cancer-no-brasil.pdf>>. Accessed on: 10 sep. 2022.

INCA, I. N. de Câncer José Alencar Gomes da S. **Detecção Precoce do Câncer**. [s. n.], 2021. Available at: <[https://www.inca.gov.br/sites/ufu.sti.inca.local/files//media/document/deteccao-precoce-do-cancer\\_0.pdf](https://www.inca.gov.br/sites/ufu.sti.inca.local/files//media/document/deteccao-precoce-do-cancer_0.pdf)>. Accessed on: 12 jan. 2023.

ISKANDAR, A. A.; JEREMY, M.; FATHONY, M. Breast cancer image pre-processing with convolutional neural network for detection and classification. *In: 2022 4th INTERNATIONAL CONFERENCE ON BIOMEDICAL ENGINEERING (IBIOMED)*. 2022, Yogyakarta, Indonesia: **Proceedings**, 2022. p. 81–86.

JAHWAR, A. F.; ABDULAZEEZ, A. M. Segmentation and classification for breast cancer ultrasound images using deep learning techniques: A review. *In: 2022 IEEE 18TH INTERNATIONAL COLLOQUIUM ON SIGNAL PROCESSING APPLICATIONS (CSPA)*. 2022, Selangor, Malaysia: **Proceedings**, 2022. p. 225–230.

KARTIKA, D. S. Y.; HERUMURTI, D.; RAHMAT, B.; YUNIARTI, A.; MAULANA, H.; ANGGRAENY, F. T. Combining of extraction butterfly image using color, texture and form features. *In: 2020 6TH INFORMATION TECHNOLOGY INTERNATIONAL SEMINAR (ITIS)*. 2020, Surabaya, Indonesia: **Proceedings**, 2020. p. 98–102.

KATTAKINDA, P.; RAJAGOPALAN, A. N. Unpaired image denoising. *In: 2020 IEEE INTERNATIONAL CONFERENCE ON IMAGE PROCESSING (ICIP)*. 2021, Abu Dhabi, United Arab Emirates: **Proceedings**, 2020. p. 1073–1077.

KHAN, H. U.; RAZA, B.; WAHEED, A.; SHAH, H. Msf-model: Multi-scale feature fusion-based domain adaptive model for breast cancer classification of histopathology images. **IEEE Access**, [S.l.], v. 10, p. 122530–122547, 2022.

KHAN, M. A.; MUHAMMAD, K.; SHARIF, M.; AKRAM, T.; ALBUQUERQUE, V. H. C. d. Multi-class skin lesion detection and classification via teledermatology. **IEEE Journal of Biomedical and Health Informatics**, [S.l.], v. 25, n. 12, p. 4267–4275, 2021.

KHAN, S.; MUHAMMAD, K.; MUMTAZ, S.; BAIK, S. W.; ALBUQUERQUE, V. H. C. de. Energy-efficient deep cnn for smoke detection in foggy iot environment. **IEEE Internet of Things Journal**, [S.l.], v. 6, n. 6, p. 9237–9245, 2019.

KHUMDEE, M.; ASSAWAROONGSAKUL, P.; PHASUKKIT, P.; HOUNGKAMHANG, N. Breast cancer detection using ir-uwv with deep learning. *In: 2021 16TH INTERNATIONAL JOINT SYMPOSIUM ON ARTIFICIAL INTELLIGENCE AND NATURAL LANGUAGE PROCESSING (ISAI-NLP)*. 2021, Ayutthaya, Thailand: **Proceedings**, 2021. p. 1–4.

KIM, E.; CHO, H.-H.; KWON, J.; OH, Y.-T.; KO, E. S.; PARK, H. Tumor-attentive segmentation-guided gan for synthesizing breast contrast-enhanced mri without contrast agents. **IEEE Journal of Translational Engineering in Health and Medicine**, [S.l.], v. 11, p. 32–43, 2023.

KR, K.; KV, A. R.; PILLAI, A. An improved feature selection and classification of gene expression profile using svm. *In: 2019 2ND INTERNATIONAL CONFERENCE ON INTELLIGENT COMPUTING, INSTRUMENTATION AND CONTROL TECHNOLOGIES (ICICICT)*. 2019, Kannur, India: **Proceedings**, 2019. p. 1033–1037.

KUMAR, A.; ANSARI, M.; ASHOK, A. Review of feature extraction and classification methods used in cad system. *In: 2020 2ND INTERNATIONAL CONFERENCE ON ADVANCES IN COMPUTING, COMMUNICATION CONTROL AND NETWORKING (ICACCCN)*. 2020, Greater Noida, India: **Proceedings**, 2020. p. 222–227.

KUMWILAISAK, W.; PIRIYATHARAWET, T.; LASANG, P.; THATPHITHAKKUL, N. On the numerical distortion-mutual information function of image denoising with deep convolutional networks. *In: 2020 17TH INTERNATIONAL CONFERENCE ON ELECTRICAL ENGINEERING/ELECTRONICS, COMPUTER, TELECOMMUNICATIONS AND INFORMATION TECHNOLOGY (ECTI-CON)*. 2020, Phuket, Thailand: **Proceedings**, 2020. p. 474–477.

LATIF, G.; BUTT, M. O.; ANEZI, F. Y. A.; ALGHAZO, J. Ultrasound image despeckling and detection of breast cancer using deep cnn. *In: 2020 RIVF INTERNATIONAL CONFERENCE ON COMPUTING AND COMMUNICATION TECHNOLOGIES (RIVF)*. 2020, Ho Chi Minh City, Vietnam: **Proceedings**, 2020. p. 1–5.

LI, L.; YANG, F.; LI, J.; XU, B.; WANG, D. Research progress on benign and malignant lung nodule classification based on deep learning. *In: 2020 CROSS STRAIT RADIO SCIENCE WIRELESS TECHNOLOGY CONFERENCE (CSRSWTC)*. 2020, Fuzhou, China: **Proceedings**, 2020. p. 1–3.

LI, M. Research on the detection method of breast cancer deep convolutional neural network based on computer aid. *In: 2021 IEEE ASIA-PACIFIC CONFERENCE ON IMAGE PROCESSING, ELECTRONICS AND COMPUTERS (IPEC)*. 2021, Dalian, China: **Proceedings**, 2021. p. 536–540.

LIANG, C.-H.; CHEN, Y.-A.; LIU, Y.-C.; HSU, W. H. Raw image deblurring. **IEEE Transactions on Multimedia**, [S.l.], v. 24, p. 61–72, 2022.

LIN, C.; WANG, Y.; WANG, T.; NI, D. Segmentation and recovery of pathological mr brain images using transformed low-rank and structured sparse decomposition. *In: 2019 IEEE 16TH INTERNATIONAL SYMPOSIUM ON BIOMEDICAL IMAGING (ISBI 2019)*. 2019, Venice, Italy: **Proceedings**, 2019. p. 1878–1881.

LIU, H.; XIAO, X.; LI, Y.; MI, Q.; YANG, Z. Effective data classification via combining neural networks and svm. *In: 2019 CHINESE CONTROL AND DECISION CONFERENCE (CCDC)*. 2021, Nanchang, China: **Proceedings**, 2019. p. 4006–4009.

LIU, M.; HU, L.; TANG, Y.; WANG, C.; HE, Y.; ZENG, C.; LIN, K.; HE, Z.; HUO, W. A deep learning method for breast cancer classification in the pathology images. **IEEE Journal of Biomedical and Health Informatics**, [S.l.], v. 26, n. 10, p. 5025–5032, 2022.

LIU, X.; WU, Z.; TANG, C. Modulation recognition algorithm based on resnet50 multi-feature fusion. *In: 2021 INTERNATIONAL CONFERENCE ON INTELLIGENT TRANSPORTATION, BIG DATA SMART CITY (ICITBS)*. 2021, Xi'an, China: **Proceedings**, 2021. p. 677–680.

LIU, Y.; MA, W. Fusing edge-information in image denoising based on cnn. *In: 2020 IEEE INTERNATIONAL CONFERENCE ON ARTIFICIAL INTELLIGENCE AND COMPUTER APPLICATIONS (ICAICA)*. 2020, Dalian, China: **Proceedings**, 2020. p. 544–548.

LOIZIDOU, K.; SKOUROUMOUNI, G.; NIKOLAOU, C.; PITRIS, C. Automatic breast mass segmentation and classification using subtraction of temporally sequential digital mammograms. **IEEE Journal of Translational Engineering in Health and Medicine**, [S.l.], v. 10, p. 1–11, 2022.

MA, J.; LI, J.; WANG, W. Application of wavelet entropy and knn in motor fault diagnosis. *In: 2022 4TH INTERNATIONAL CONFERENCE ON COMMUNICATIONS, INFORMATION SYSTEM AND COMPUTER ENGINEERING (CISCE)*. 2022, Shenzhen, China: **Proceedings**, 2022. p. 221–226.

MARQUES FILHO, O.; VIEIRA NETO, H. **Processamento digital de imagens**. [S.l.]: Brasport, 1999.

MATIC, Z.; KADRY, S. Tumor segmentation in breast mri using deep learning. *In: 2022 FIFTH INTERNATIONAL CONFERENCE OF WOMEN IN DATA SCIENCE AT PRINCE SULTAN UNIVERSITY (WIDS PSU)*. 2022, Riyadh, Saudi Arabia: **Proceedings**, 2022. p. 49–51.

MEMARI, N.; MOGHBEL, M. Computer-aided diagnosis (cad) of knee osteoarthritis based on magnetic resonance imaging for quantitative pathogenesis analysis and visualization. *In: 2020 IEEE 10TH SYMPOSIUM ON COMPUTER APPLICATIONS INDUSTRIAL ELECTRONICS (ISCAIE)*. 2020, Malaysia: **Proceedings**, 2020. p. 192–197.

MENKE, C. H.; BIA ~S, J. V.; XAVIER, N. L.; A, C. J.; RABIN, E. G.; BITTELBRUNN, A.; CERICATTO, R. **Rotinas em mastologia**. [S.l.]: Artmed, 2007.

MESQUITA, V. A.; CORTEZ, P. C.; RIBEIRO, A. B.; de Albuquerque, V. H. C. A novel method for lung nodule detection in computed tomography scans based on boolean equations and vector of filters techniques. **Computers and Electrical Engineering**, v. 100, 2022. ISSN 0045-7906. Available at: <<https://www.sciencedirect.com/science/article/pii/S004579062200194X>>. Accessed on: 10 sep. 2022.

MIN, X.; ZHAI, G.; GU, K.; ZHU, Y.; ZHOU, J.; GUO, G.; YANG, X.; GUAN, X.; ZHANG, W. Quality evaluation of image dehazing methods using synthetic hazy images. **IEEE Transactions on Multimedia**, [S.l.], v. 21, n. 9, p. 2319–2333, 2019.

MISRA, S.; JEON, S.; MANAGULI, R.; LEE, S.; KIM, G.; YOON, C.; LEE, S.; BARR, R. G.; KIM, C. Bi-modal transfer learning for classifying breast cancers via combined b-mode and ultrasound strain imaging. **IEEE Transactions on Ultrasonics, Ferroelectrics, and Frequency Control**, [S.l.], v. 69, n. 1, p. 222–232, 2022.

MOHAMED, A.; WAHBA, A. A.; SAYED, A. M.; HAGGAG, M. A.; EL-ADAWY, M. I. Enhancement of ultrasound images quality using a new matching material. *In: 2019 INTERNATIONAL CONFERENCE ON INNOVATIVE TRENDS IN COMPUTER ENGINEERING (ITCE)*. 2019, Aswan, Egypt: **Proceedings**, 2019. p. 47–51.

MOORE, K. L.; DALLEY, A. F.; AGUR, A. M. **Moore anatomia orientada para a clínica**. [S.l.]: Guanabara Koogan, 2014.

MOSHREFI, A.; NABKI, F. An efficient method to enhance the quality of ultrasound medical images. *In: 2021 IEEE INTERNATIONAL MIDWEST SYMPOSIUM ON CIRCUITS AND SYSTEMS (MWSCAS)*. 2021, Lansing, MI, USA: **Proceedings**, 2021. p. 267–270.

MUFID, M. R.; BASOFI, A.; RASYID, M. U. H. A.; ROCHIMANSYAH, I. F.; ROKHIM, A. Design an mvc model using python for flask framework development. *In: 2019 INTERNATIONAL ELECTRONICS SYMPOSIUM (IES)*. 2019, Surabaya, Indonesia: **Proceedings**, 2019. p. 214–219.



MUHAMMAD, K.; HUSSAIN, T.; TANVEER, M.; SANNINO, G.; ALBUQUERQUE, V. H. C. de. Cost-effective video summarization using deep cnn with hierarchical weighted fusion for iot surveillance networks. **IEEE Internet of Things Journal**, [S.l.], v. 7, n. 5, p. 4455–4463, 2020.

MUHAMMAD, K.; MUSTAQEEM; ULLAH, A.; IMRAN, A. S.; SAJJAD, M.; KIRAN, M. S.; SANNINO, G.; de Albuquerque, V. H. C. Human action recognition using attention based lstm network with dilated cnn features. **Future Generation Computer Systems**, [S.l.], v. 125, p. 820–830, 2021. ISSN 0167-739X. Available at: <<https://www.sciencedirect.com/science/article/pii/S0167739X21002405>>.

MUNADI, K.; MUCHTAR, K.; MAULINA, N.; PRADHAN, B. Image enhancement for tuberculosis detection using deep learning. **IEEE Access**, [S.l.], v. 8, p. 217897–217907, 2020.

NAPIER, J.; DEBONO, C. J.; BEZZINA, P.; ZARB, F. A cad system for brain haemorrhage detection in head ct scans. *In: IEEE EUROCON 2019 - 18TH INTERNATIONAL CONFERENCE ON SMART TECHNOLOGIES*. 2021, Novi Sad, Serbia: **Proceedings**, 2019. p. 1–6.

OLIVEIRA, A. D. D. **MalariaSystem**: uma ferramenta para diagnóstico automático de malária em dispositivos móveis. 2014. 88 f. Master's Thesis (Mestrado em Informática Aplicada) — Universidade Federal Rural de Pernambuco, Recife, 2014.

PANDE, N. A.; BHOYAR, D. A comprehensive review of lung nodule identification using an effective computer-aided diagnosis (cad) system. *In: 2022 4TH INTERNATIONAL CONFERENCE ON SMART SYSTEMS AND INVENTIVE TECHNOLOGY (ICSSIT)*. 2022, Tirunelveli, India: **Proceedings**, 2022. p. 1254–1257.

PANG, S.; PANG, C.; ZHAO, L.; CHEN, Y.; SU, Z.; ZHOU, Y.; HUANG, M.; YANG, W.; LU, H.; FENG, Q. Spineparsenet: Spine parsing for volumetric mr image by a two-stage segmentation framework with semantic image representation. **IEEE Transactions on Medical Imaging**, [S.l.], v. 40, n. 1, p. 262–273, 2021.

PATEL, V.; CHAURASIA, V.; MAHADEVA, R.; PATOLE, S. P. Garl-net: Graph based adaptive regularized learning deep network for breast cancer classification. **IEEE Access**, [S.l.], v. 11, p. 9095–9112, 2023.

QADRI, S. F.; SHEN, L.; AHMAD, M.; QADRI, S.; ZAREEN, S. S.; AKBAR, M. A. Svseg: stacked sparse autoencoder-based patch classification modeling for vertebrae segmentation. **Mathematics**, [S.l.], v. 10, n. 5, p. 796, 2022.

QUAN, Y.; DONG, S.; FENG, W.; DAUPHIN, G.; ZHAO, G.; WANG, Y.; XING, M. Spectral-spatial feature extraction based cnn for hyperspectral image classification. *In: IGARSS 2020 - 2020 IEEE INTERNATIONAL GEOSCIENCE AND REMOTE SENSING SYMPOSIUM*. 2020, Waikoloa, HI, USA: **Proceedings**, 2020. p. 485–488.

RAIKWAR, S. C.; TAPASWI, S. Lower bound on transmission using non-linear bounding function in single image dehazing. **IEEE Transactions on Image Processing**, [S.l.], v. 29, p. 4832–4847, 2020.

RODRIGUEZ-MOLARES, A.; RINDAL, O. M. H.; D'HOOGHE, J.; MåSøY, S.-E.; AUSTENG, A.; TORP, H. The generalized contrast-to-noise ratio. *In: 2018 IEEE INTERNATIONAL ULTRASONICS SYMPOSIUM (IUS)*. 2018, Kobe, Japan: **Proceedings**, 2018. p. 1–4.

SABILLA, I. A.; MEIRISDIANA, M.; SUNARYONO, D.; HUSNI, M. Best ratio size of image in steganography using portable document format with evaluation rmse, psnr, and ssim. *In: 2021 4TH INTERNATIONAL CONFERENCE OF COMPUTER AND INFORMATICS ENGINEERING (IC2IE)*. 2021, Depok, Indonesia: **Proceedings**, 2021. p. 289–294.

SADEGHI, H.; RAIE, A.-A. Human vision inspired feature extraction for facial expression recognition. **Multimedia Tools and Applications**, [S.l.], v. 78, p. 30335–30353, 2019.

SAIFUDIN, S. A.; SULAIMAN, S. N.; KARIM, N. K. A.; OSMAN, M. K.; ISA, I. S.; HARRON, N. A. A comparative study of unsharp masking filters for enhancement of digital breast tomosynthesis images. *In: 2022 IEEE 12TH INTERNATIONAL CONFERENCE ON CONTROL SYSTEM, COMPUTING AND ENGINEERING (ICCSCE)*. 2022, Penang, Malaysia: **Proceedings**, 2022. p. 147–152.

SALIM, A. P.; LAKSITOWENING, K. A.; ASROR, I. Time series prediction on college graduation using knn algorithm. *In: 2020 8TH INTERNATIONAL CONFERENCE ON INFORMATION AND COMMUNICATION TECHNOLOGY (ICOICT)*. 2020, Yogyakarta, Indonesia: **Proceedings**, 2020. p. 1–4.

SINGH, P.; MUKUNDAN, R.; RYKE, R. d. Feature enhancement in medical ultrasound videos using multifractal and contrast adaptive histogram equalization techniques. *In: 2019 IEEE CONFERENCE ON MULTIMEDIA INFORMATION PROCESSING AND RETRIEVAL (MIPR)*. 2019, San Jose, USA: **Proceedings**, 2019. p. 240–245.

SOUZA, R. W.; SILVA, D. S.; PASSOS, L. A.; RODER, M.; SANTANA, M. C.; PINHEIRO, P. R.; de Albuquerque, V. H. C. Computer-assisted parkinson's disease diagnosis using fuzzy optimum- path forest and restricted boltzmann machines. **Computers in Biology and Medicine**, v. 131, 2021. ISSN 0010-4825. Available at: <<https://www.sciencedirect.com/science/article/pii/S0010482521000548>>. Accessed on: 20 sep. 2022.

SULAIMAN, S. N.; NORMAZLI, M. H.; HARRON, N. A.; KARIM, N. K. A.; AHMAD, K. A.; SOH, Z. H. C. A convolutional neural network model for image enhancement of extremely dense breast tissue in digital breast tomosynthesis images. *In: 2022 IEEE 12TH INTERNATIONAL CONFERENCE ON CONTROL SYSTEM, COMPUTING AND ENGINEERING (ICCSCE)*. 2022, Penang, Malaysia: **Proceedings**, 2022. p. 153–157.

SUNG, H.; FERLAY, J.; SIEGEL, R. L.; LAVERSANNE, M.; SOERJOMATARAM, I.; JEMAL, A.; BRAY, F. Global cancer statistics 2020: Globocan estimates of incidence and mortality worldwide for 36 cancers in 185 countries. **CA: a cancer journal for clinicians**, [S.l.], v. 71, n. 3, p. 209–249, 2021.

TOMASI, C.; MANDUCHI, R. Bilateral filtering for gray and color images. *In: SIXTH INTERNATIONAL CONFERENCE ON COMPUTER VISION*. 1998, Bombay, India: **Proceedings**, 1998. p. 839–846.

TRINKS, S.; FELDEN, C. A differentiation between image mining and computer vision in the application area of big data. *In: 2020 IEEE INTERNATIONAL CONFERENCE ON BIG DATA (BIG DATA)*. 2020, Atlanta, USA: **Proceedings**, 2020. p. 5839–5842.

TURESSON, H. K.; RIBEIRO, S.; PEREIRA, D. R.; PAPA, J. P.; ALBUQUERQUE, V. H. C. de. Machine learning algorithms for automatic classification of marmoset vocalizations. **PLoS**

one, [S.l.], v. 11, n. 9, 2016. Available at: <<https://journals.plos.org/plosone/article?id=10.1371/journal.pone.0163041>>. Accessed on: 10 sep. 2022.

ULLAH, H.; MUHAMMAD, K.; IRFAN, M.; ANWAR, S.; SAJJAD, M.; IMRAN, A. S.; ALBUQUERQUE, V. H. C. de. Light-dehazenet: A novel lightweight cnn architecture for single image dehazing. **IEEE Transactions on Image Processing**, [S.l.], v. 30, p. 8968–8982, 2021.

VOCATURO, E.; ZUMPANO, E. Artificial intelligence approaches on ultrasound for breast cancer diagnosis. *In*: 2021 IEEE INTERNATIONAL CONFERENCE ON BIOINFORMATICS AND BIOMEDICINE (BIBM). 2021, Houston, USA: **Proceedings**, 2021. p. 3116–3121.

WAN, Z.; GU, T. A bootstrapped transfer learning model based on resnet50 and xception to classify buildings post hurricane. *In*: 2021 2ND INTERNATIONAL CONFERENCE ON BIG DATA ARTIFICIAL INTELLIGENCE SOFTWARE ENGINEERING (ICBASE). 2021, Zhuhai, China: **Proceedings**, 2021. p. 265–270.

WANG, B.; HU, X.; ZHANG, J.; XU, C.; GAO, Z. Intelligent internet of things in mammography screening using multicenter transformation between unified capsules. **IEEE Internet of Things Journal**, [S.l.], v. 10, n. 2, p. 1536–1545, 2023.

WANG, H.; WANG, J. Short term wind speed forecasting based on feature extraction by cnn and mlp. *In*: 2021 2ND INTERNATIONAL SYMPOSIUM ON COMPUTER ENGINEERING AND INTELLIGENT COMMUNICATIONS (ISCEIC). 2021, Nanjing, China: **Proceedings**, 2021. p. 191–197.

WANG, Y.; LEI, B.; ELAZAB, A.; TAN, E.-L.; WANG, W.; HUANG, F.; GONG, X.; WANG, T. Breast cancer image classification via multi-network features and dual-network orthogonal low-rank learning. **IEEE Access**, v. 8, p. 27779–27792, 2020.

WANG, Y.; WAN, R.; YANG, W.; LI, H.; CHAU, L.-P.; KOT, A. C. Low-light image enhancement with normalizing flow. **arXiv**, [S.l.], 2021. Available at: <<https://arxiv.org/abs/2109.05923>>. Accessed on: 02 mar. 2022.

WANG, Y.; WANG, N.; XU, M.; YU, J.; QIN, C.; LUO, X.; YANG, X.; WANG, T.; LI, A.; NI, D. Deeply-supervised networks with threshold loss for cancer detection in automated breast ultrasound. **IEEE Transactions on Medical Imaging**, [S.l.], v. 39, n. 4, p. 866–876, 2020.

WANG, Y.; ZHAO, Z.; HE, J.; ZHU, Y.; WEI, X. A method of vehicle flow training and detection based on resnet50 with centernet method. *In*: 2021 INTERNATIONAL CONFERENCE ON COMMUNICATIONS, INFORMATION SYSTEM AND COMPUTER ENGINEERING (CISCE). 2021, Beijing, China: **Proceedings**, 2021. p. 335–339.

WANG, Z.; LUO, Y.; XIN, J.; ZHANG, H.; QU, L.; WANG, Z.; YAO, Y.; ZHU, W.; WANG, X. Computer-aided diagnosis based on extreme learning machine: A review. **IEEE Access**, [S.l.], v. 8, p. 141657–141673, 2020.

WEIDERPASS, E.; STEWART, B. W. **World Cancer Report: Cancer Research Cancer Prevention**. [s. n.], 2020. Available at: <<https://publications.iarc.fr/586>>. Accessed on: 12 mar. 2022.

WHO, W. H. O. **Guide to cancer early diagnosis**. [s. n.], 2017. Available at: <<https://apps.who.int/iris/bitstream/handle/10665/254500/9789241511940-eng.pdf?sequence=1&isAllowed=y>>. Accessed on: 12 jan. 2023.

- WU, H.; HUO, Y.; PAN, Y.; XU, Z.; HUANG, R.; XIE, Y.; HAN, C.; LIU, Z.; WANG, Y. Learning pre- and post-contrast representation for breast cancer segmentation in dce-mri. *In: 2022 IEEE 35TH INTERNATIONAL SYMPOSIUM ON COMPUTER-BASED MEDICAL SYSTEMS (CBMS)*. 2022, Shenzhen, China: **Proceedings**, 2022. p. 355–359.
- XIE, B.; SHEN, J.; YANG, J.; LV, Z. Single image dehazing based upon modified image enhancement algorithm. *In: 2020 5TH INTERNATIONAL CONFERENCE ON INFORMATION SCIENCE, COMPUTER TECHNOLOGY AND TRANSPORTATION (ISCTT)*. 2020, Shenyang, China: **Proceedings**, 2020. p. 448–451.
- XU, M.; HUANG, K.; QI, X. A regional-attentive multi-task learning framework for breast ultrasound image segmentation and classification. **IEEE Access**, [S.l.], v. 11, p. 5377–5392, 2023.
- YAGANTEESWARUDU, A. Multi disease prediction model by using machine learning and flask api. *In: 2020 5TH INTERNATIONAL CONFERENCE ON COMMUNICATION AND ELECTRONICS SYSTEMS (ICCES)*. 2020, Coimbatore, India: **Proceedings**, 2020. p. 1242–1246.
- YANG, Q.; YAN, P.; ZHANG, Y.; YU, H.; SHI, Y.; MOU, X.; KALRA, M. K.; ZHANG, Y.; SUN, L.; WANG, G. Low-dose ct image denoising using a generative adversarial network with wasserstein distance and perceptual loss. **IEEE Transactions on Medical Imaging**, [S.l.], v. 37, n. 6, p. 1348–1357, 2018.
- YANG, X.; YANG, D.; HUANG, C. An interactive prediction system of breast cancer based on resnet50, chatbot and pyqt. *In: 2021 2ND INTERNATIONAL SEMINAR ON ARTIFICIAL INTELLIGENCE, NETWORKING AND INFORMATION TECHNOLOGY (AINIT)*. 2021, Shanghai, China: **Proceedings**, 2021. p. 309–316.
- YIN, P.; YUAN, R.; CHENG, Y.; WU, Q. Deep guidance network for biomedical image segmentation. **IEEE Access**, [S.l.], v. 8, p. 116106–116116, 2020.
- YING, Z.; LI, G.; REN, Y.; WANG, R.; WANG, W. A new image contrast enhancement algorithm using exposure fusion framework. *In: FELSBERG, M.; HEYDEN, A.; KRÜGER, N. (Ed.). Computer analysis of images and patterns*. Cham: Springer International Publishing, 2017. p. 36–46.
- YU, J.; CHEN, L.; LI, H.; ZHOU, S.; WANG, L.; ZHANG, Z. Ultrasound image denoising based on fuzzy logic. *In: 2019 INTERNATIONAL CONFERENCE ON COMMUNICATIONS, INFORMATION SYSTEM AND COMPUTER ENGINEERING (CISCE)*. 2019, Haikou, China: **Proceedings**, 2019. p. 230–233.
- ZHANG, D.; LI, X. Research on computer aided diagnosis system for neurocritical and critical diseases. *In: 2021 6TH INTERNATIONAL CONFERENCE ON COMMUNICATION AND ELECTRONICS SYSTEMS (ICCES)*. 2021, Coimbatre, India: **Proceedings**, 2021. p. 1234–1237.
- ZHANG, X.; HU, H.-M.; CHEN, J. Fast image deblurring based on dual-exposure prior. *In: 2019 IEEE VISUAL COMMUNICATIONS AND IMAGE PROCESSING (VCIP)*. 2019, Sydney, Australia: **Proceedings**, 2019. p. 1–4.

ZHANG, Y.; WANG, S.; LI, W.; YIN, X.; DENG, J. Large-scale simulated dataset for aerial image deblurring based on dota dataset. *In: 2020 IEEE INTERNATIONAL CONFERENCE ON INFORMATION TECHNOLOGY,BIG DATA AND ARTIFICIAL INTELLIGENCE (ICIBA).* 2020, Chongqing, China: **Proceedings**, 2020. v. 1, p. 1453–1456.

ZHAO, H.; NIU, J.; MENG, H.; WANG, Y.; LI, Q.; YU, Z. Focal u-net: A focal self-attention based u-net for breast lesion segmentation in ultrasound images. *In: 2022 44TH ANNUAL INTERNATIONAL CONFERENCE OF THE IEEE ENGINEERING IN MEDICINE BIOLOGY SOCIETY (EMBC).* 2022, Glasgow, United Kingdom: **Proceedings**, 2022. p. 1506–1511.

ZHENG, M.; QI, G.; ZHU, Z.; LI, Y.; WEI, H.; LIU, Y. Image dehazing by an artificial image fusion method based on adaptive structure decomposition. **IEEE Sensors Journal**, [S.l.], v. 20, n. 14, p. 8062–8072, 2020.

ZHIHONG, W.; XIAOHONG, X. Study on histogram equalization. *In: 2011 2ND INTERNATIONAL SYMPOSIUM ON INTELLIGENCE INFORMATION PROCESSING AND TRUSTED COMPUTING.* 2011, Wuhan, China: **Proceedings**, 2011. p. 177–179.

ZHU, H.; CHENG, Y.; PENG, X.; ZHOU, J. T.; KANG, Z.; LU, S.; FANG, Z.; LI, L.; LIM, J.-H. Single-image dehazing via compositional adversarial network. **IEEE Transactions on Cybernetics**, [S.l.], v. 51, n. 2, p. 829–838, 2021.